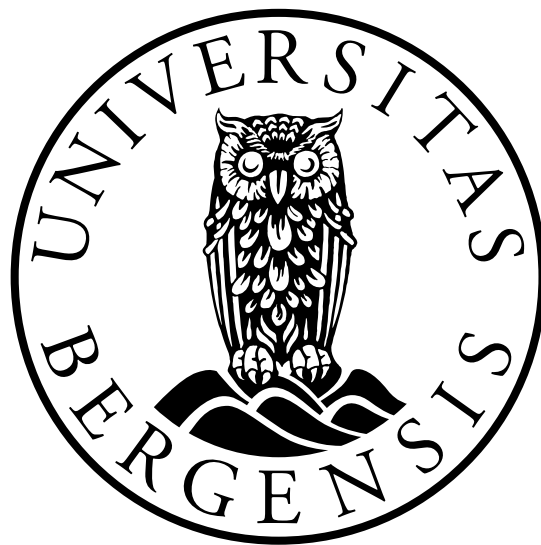# A Study of Wind-Wave Interactions using Offshore High-Frequency Wind and Wave Measurements

Master's Thesis in Energy

Tore Totland Skjerdal
Geophysical Institute
University of Bergen

May 31, 2022

Acknowledgement

I want to thank my supervisor Mostafa Bakhoday Paskyabi (*Associate Professor at Geophysical Institute, UiB*), for providing this thesis subject, giving me insight into wind-wave interactions and broadening my knowledge of critical wind-wave interactions. I would also like to thank my co-supervisors, Martin Flügge (*PhD Candidate at Geophysical Institute, UiB*) and Joachim Reuder (*Professor at Geophysical Institute, UiB*), for explaining processes within the Marine Atmospheric Boundary Layers (MABL) and for providing meaningful feedback on my work. The contributions the three of you have provided have been significant and crucial for the construction of this thesis.

Getting an MSc degree focusing on wind energy has been a long journey. I have transitioned from being an electrician to taking a BSc in Energy Technology at Western Norway University of Applied Sciences before finally doing an MSc in wind energy at the University of Bergen. I want to thank all my professors and co-students along the way for sharing knowledge and supporting me.

Writing this thesis has been a steep learning curve, where my knowledge of coding and processes within the MABL has been challenged. I am grateful for all the support I received from friends and family, and not the least, all the emotional and professional help I have received from my co-students during the writing of this thesis. I would especially express my gratitude to Adrian, Martine, Tiril and Christina for all the days spent together at the study hall, for helpful comments and feedback and for our daily coffee break to boost our morality.

<div align="right">

Tore Totland Skjerdal
Tore.T.Skjerdal@gmail.com
Bergen, May 31, 2022

</div>

"The story behind why data is missing might, in many cases, be more important than the story told by the data we have"

Abstract

Technology advancements in the wind energy sector are growing rapidly due to increasing electricity demands, coupled with global targets to increase the share of renewable energy supply. The size of the turbines has dramatically increased, and the stable and higher offshore winds are being utilized, moving from onshore- to offshore wind parks. Herein, research on how wind-wave interactions affect power generation and the wind field surrounding the wind parks have become increasingly important.

This growing interest in wind-wave interactions has led this thesis to investigate how different wind-wave interactions interfere with the surrounding wind field, affecting turbine performance and how big of a contribution these interactions yield. The physical processes within the marine boundary layer (MABL), such as vertical transport of horizontal momentum and wind-wave misalignment, are investigated to determine how they affect wind power generation. In addition, the shear exponent and Weibull parameters have been identified, together with environmental contour plots stating the extreme parameters at the FINO1 measurement site.

Data retrieved from FINO1 (during the OBLEX-F1 measurement campaign and routinely performed measurements at FINO1), NORA3 and SCADA data from the Alpha Ventus 4 wind turbine have been combined to describe the conditions present at the measurement site. Wind, wave and wind turbine data are combined to see whether specific wind-wave interactions affect the wind field to such a degree that it is visible in wind power generation. Multiple power curves are presented to indicate any significant differences in power generated during wind-wave interaction events of interest, where results show that wind-wave alignments affect power generation. The best wind power generation results are found during aligned wind waves, whereas the power curve for opposed wind waves deviates by 5.7%. No clear indication is shown for the upward transfer of horizontal momentum on the power. In addition, the shear exponent, the Weibull parameters for wind speed and significant wave height are presented. All show an effect of wind-wave alignment. Finally, wind roses show wind veer during the different case studies, while environmental contour plots show the extreme environmental parameters at the measurement site.

Contents

Chapter 1

Thesis Introduction

1.1 Introduction

Wind energy generation are gaining momentum in Europe, where wind resources are being utilised at an increasingly rate [1]. According to WindEurope [2, 3], Europe added 14,7 GW of new wind power capacity in 2020 and 17.4 GW in 2021, while 116 GW are scheduled for installation within the next five years [3]. Today 15% of Europe's electricity demand is covered by wind energy, where onshore wind is a significant contributor at 88% [3]. Wind turbine technology has faced considerable advancements in light of the increased need for more electricity and the change from fossil fuels to renewable energy. Since the first official European wind park was commissioned in 1982 [4], the size of the turbines has dramatically increased, and the stable and higher offshore winds are being utilized, moving from onshore- to offshore wind parks. As of 2019, Europe had 110 offshore wind farms divided into 12 different European countries, representing 22,072 MW [5]. As seen in the Offshore Wind in Europe report [1], the number of offshore wind installations has increased each year since 2009. The report also shows an increase in turbine capacity, which has more than doubled from 2009 to 2019. As more turbines are installed offshore, and the turbine capacity increases, a complete understanding of the conditions at offshore wind sites is necessary. This has led to an increased focus on offshore wind conditions and the understanding of how the ocean and atmosphere interact. Several studies throughout the years have investigated these interactions and most peer-reviewed publications on wind-wave interactions have been published over the last five years [6]. As Table 1.1 shows, there is a significant incentive from both the research environment and the industry to enhance further the knowledge we have and to utilize the wind energy source found offshore.

Time Perspective	# of Publications
All time	14260
Last 20 Years	12328
Last 10 Years	9076
Last 5 Years	5865

Table 1.1: Number of peer-reviewed publications on wind-wave interactions as of 16.05.2022.

1.2 Motivation

The challenge in the offshore wind industry is highly related to the harsh environment found offshore, where waves and wind interacts and creates conditions that differ compared to onshore. The interactions between the ocean and the atmosphere lead to constant exchanges of heat, momentum and humidity [7] where the ocean surface influences the wind field and wind resources [8–11]. Offshore we have a lower surface roughness length compared to onshore, and studies have proved that swell waves may transfer momentum from the ocean to the atmosphere, thereby directly influencing the wind field above [12]. Awareness of how wind-wave interactions affect the wind field is essential for the planning-, construction- and operational phase of a wind park. Wind park design criteria for structural loads and profitability estimates are based on wind resource assessment. Wind turbine profitability and capacity factors depend on wind conditions, where weather forecasts and understanding of wind sources are vital for assessing the best operation and maintenance, O&M, and routine. Therefore a good insight into flow conditions and how they affect a wind turbine is crucial for estimating the performance of a turbine. Wind models and -analysis need to take wind-wave interactions into account to prevent shutdowns of turbines during ideal wind conditions. As mentioned in the introduction, 1.1, several studies have investigated wind-wave interactions and misalignment in the latest year, focusing on wind-wave misalignment effects and vertical transfer of horizontal momentum from the ocean to the atmosphere. This master thesis seeks to explore how wind-wave misalignment and upward momentum affects power generation by doing three analysis of different time scales. The motivation for this thesis is to enhance and cohere the research on wind-wave interactions with the wind industry by looking at how different wind-wave interactions interfere with the surrounding wind field, affecting the turbine performance, and how big of a contribution these interactions yield.

1.3 Objectives and Contribution

The three main objectives of this thesis are to:

1. Look at the effects of misalignment on wind energy generation.

2. Conduct a process study of wind-wave interaction cases by looking at wind speed power spectra, atmospheric stability, some (higher order) statistics, two point statistics, wind shear and veer, in accord with SCADA data outputs from a wind turbine.

3. Provide an environmental contour based on NORA3 reanalysis data

This thesis will examine how different wind-wave interactions interfere with the surrounding wind field, thereby affecting wind turbine performances. Moreover, how big of a contribution these interactions yield. The main contribution of this thesis will be to combine research about wind-wave interactions and use it towards the wind industry, thereby enhancing the offshore wind industries' knowledge about the interactions between the ocean and the atmosphere and their importance for wind power generation.

1.4   Related Theory

We have comprehensive knowledge about wind conditions and wind turbines onshore, but we still lack a good understanding of how wind-wave processes affect offshore wind energy generation.

Lately, understanding of the physical processes in the Marine Atmospheric Boundary Layer (MABL) has increased. Research shows that the stability of the MABL affects power generation in offshore wind parks. Sonia Wharton and Julie K. Lundquist, [13] highlighted the benefits of observing more complete wind profiles, including both wind speed and turbulence, across the whole turbine rotor disk. Their results suggested that the accuracy of wind energy resource assessments would improve if atmospheric stability impacts were measured and incorporated appropriately. For new and higher wind turbines, meteorological features such as the vertical gradient in the mean wind, the wind direction and the turbulence intensity above the ocean surface have become crucial in order to complete a wind analysis [14].

The atmospheric boundary layer (ABL) turbulence is generated either by shear forces or thermal instabilities. Thermally generated turbulence is dominant during periods of low wind speeds, while wind shear generated turbulence prevails for high wind speeds [15]. In the MABL, the surface roughness length increases with increasing wind speed due to the interaction between the ocean and the atmosphere [14]. Further research has shown that swell waves can influence wind speed. The wave shear stress is considerable in the MABL, and the vertical transfer horizontal momentum between the ocean and atmosphere can be directed either upward or downward. Swells affect the atmosphere, strengthening the wind shear, while wind influences the ocean, creating waves. The aerodynamic roughness length is an important parameter to consider when assessing the wind profile, and several studies have tried improving it. Porchetta et al. presented a new roughness length parameterization accounting for wind-wave misalignment. This study indicated that the roughness length of swell waves is dependent on the relation between wind and wave directions [16].

Wind-wave misalignment is one of the examined wind-wave interactions done to improve estimations for the offshore wind industry. Studies by van Vledder et al. [17], and Hildebrandt et al. [18] have proved that events with higher wind speeds tend to have fewer misalignment compared to events with lower wind speeds. Hildebrandt et al. observed wind-wave alignments at FINO1 and saw that wind-wave misalignment was quite frequent, where wind and waves were only aligned 20% of the time. These findings substantiate the importance of considering wind-wave alignments. Further on, Porchetta et al. [8] investigated how wind power generation is affected by wind-wave misalignment, mainly focusing on wake effects, and pointed out the importance of including waves in assessing the energy of offshore winds. Since wind speed and power are related cubical, even minor variations in the wind speed will result in significant changes in power generation. Giving the incentive to analyze and understand the relationship between ocean and atmosphere and how it may affect the wind field surrounding a wind turbine [19].

1.5   Thesis outline

The structural outline of the thesis is shown in figure 1.1. It follows a streamlined outline with a literature review for understanding the underlying theory, followed by a wind-wave interaction analysis based on three datasets.
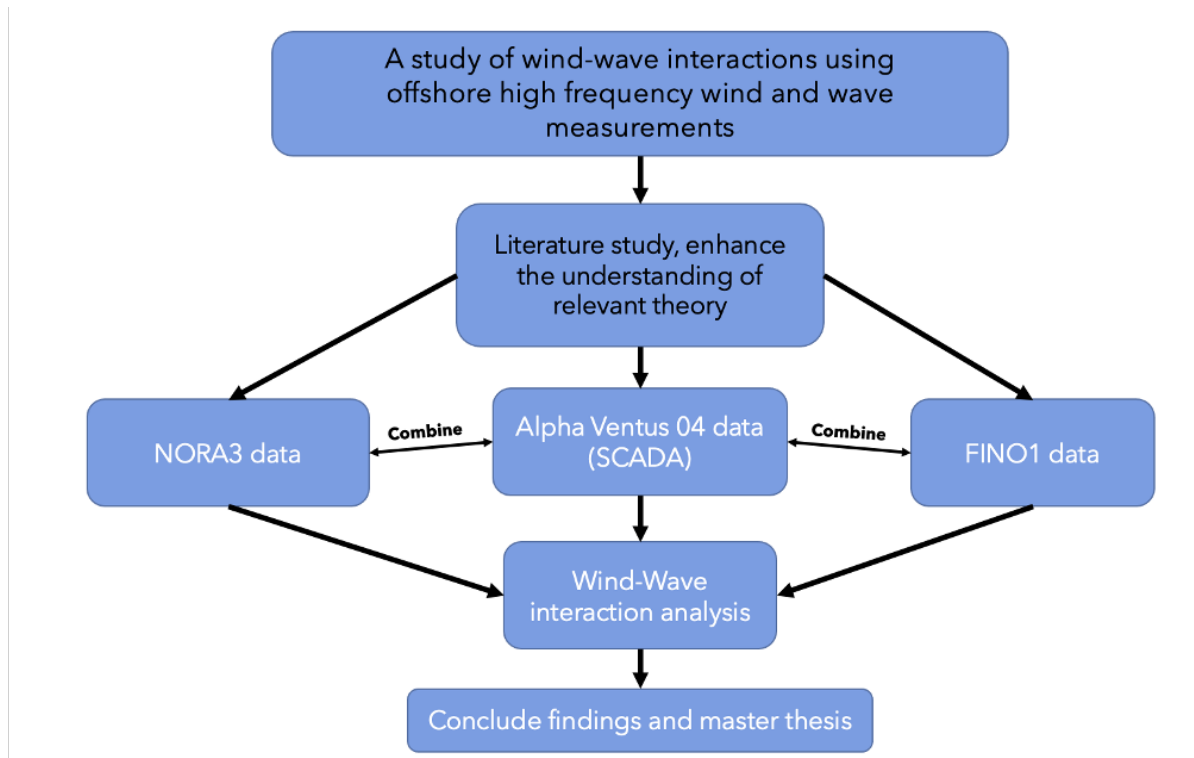

Figure 1.1: Structure and outline of the master thesis.

The wind-wave analysis includes three separate case studies.

     (I)   Overview analysis during a period of one year

    (II)   In depth analysis during a period of one month

   (III)   Long term comparison analysis using NORA3

Chapter 2

Theoretical Background

This chapter aims to provide a theoretical background relevant to the subject of this master thesis. Introducing theory about wind, waves, wind-wave interactions, boundary layers and power generation.

2.1 Wind

Wind is the movement of air caused due to pressure differences in the atmosphere, which occur mainly due to latitudinal differences in solar radiation. Variations in solar radiation cause the wind to behave differently during different seasons and diurnal cycles. The human race has utilized the wind's ability to move objects for centuries, like sailing or milling wheat. In a grand scheme, we sort the wind into two categories, local- and global wind [20].

2.1.1 Global Wind

The global wind pattern results from cold air at the poles and hot air at the equator. These temperature differences create high- and low-pressure systems, resulting in global pressure belts and convection cells. According to the second law of thermodynamics, low-pressure moves toward high-pressure. As the hot air rises at the equator, the cold air from the poles moves towards the equator to fill the space left behind. Simultaneously the hot air moves towards the pole, losing energy/heat over time, causing the air to descend towards the ground before the cycle is repeated. This cycle or wind pattern is affected by the earth's rotation, the Coriolis effect, causing the wind pattern to deflect/curve.

There are three global wind pattern circulations, the Polar-, Ferrel- and the Hadley Cell [20], shown in figure 2.1. The Hadley Cell is located by the equator, where the circulating air is subject to direct thermal solar energy. The hot air rises and moves towards the poles before it cools and descends into the subtropics. The Ferrel Cell is located in the mid-latitudes and is subject to thermally indirect solar radiation. The Ferrell Cell gets warm air from the Hadley Cell and cold air from the Polar Cell. Here colder air rises at higher latitudes, and warmer air descends into the subtropics, creating an inverse circulation where hot air moves towards the poles near the ground and
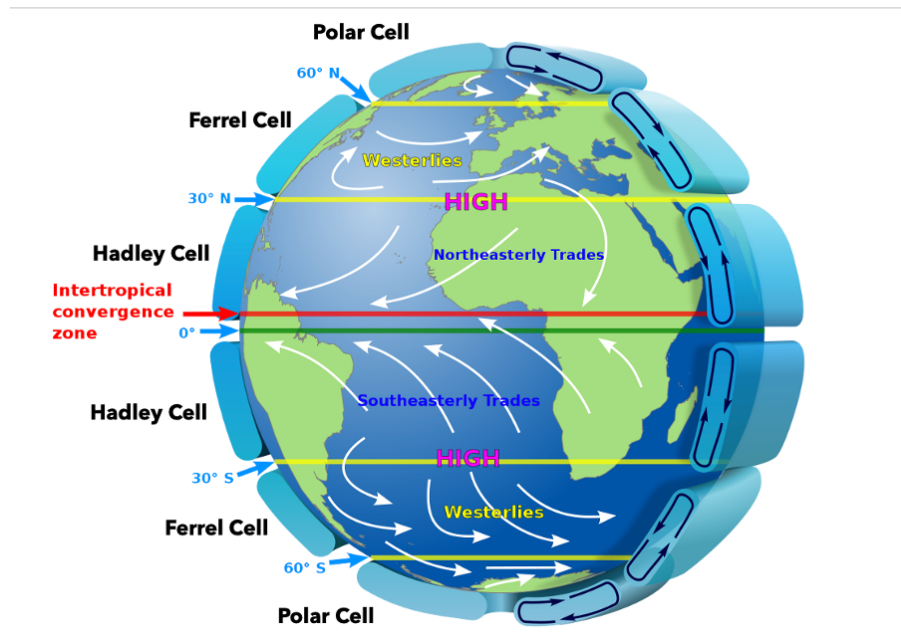
Figure 2.1: Global wind patterns. Adapted from NASA's depiction of the global wind patterns [21].

cold air towards the subtropics above—lastly, the Polar Cell is subject to direct thermal circulations. The cold air descends over the poles in the Polar Cell and rises at lower latitudes, resulting in a high pressure above the poles.

At the surface, the winds are affected by the direction of the Hadley-, Ferrel- and Polar Cell. The surface winds within the Hadley- and Polar Cell (moving towards the poles) mainly flow in an easterly direction, the surface wind within the Ferrel Cell (moving towards the equator) mainly flows in a westerly direction.

Two jet streams are located between these cells. The two main jet streams are the Polar jet, located between the Polar cell and the Ferrel cell, and the Subtropical jet, situated between the Ferrel cell and the Hadley cell. These jet streams blow from the west towards the east, at the upper part of the atmosphere.

2.1.2   Local Wind

The local wind is an airflow that moves over short distances, typically caused by temperature differences between the Atmospheric Boundary Layer (ABL) and the surface. Water has a high heat capacity, giving it the ability to store the heat gained from the sun. A pressure difference between the ocean and land occurs due to the heat capacity difference between the land and ocean surfaces. As depicted in figure 2.2, during a diurnal/nocturnal cycle or a seasonal cycle, differences in temperature between ocean and land result in air moving from low pressure to high-pressure areas, causing a land-sea breeze. Similar phenomena occur with mountains and valleys, where hot air rises along a steep mountain during the day, and the cold air descend along the mountain slope during the night.

Figure 2.2: As the sun heats the land surface, the local air starts to heat and rise. Creating a pressure difference between ocean and land, causing air to move from the high-pressure zone to the low-pressure zone, where H denotes high-pressure, and L denotes low-pressure. In the evening, this cycle changes direction, where the land surface has cooled down while the ocean has stored large quantities of heat, which can heat the surrounding air.

2.1.3 Governing Equations

The airflow caused by local or global wind patterns can be decomposed into two governing variables; the mean wind flow ($\overline{u}$) and the turbulent airflow (u'):

$$\mathbf{u} = \overline{\mathbf{u}} + \mathbf{u}'. \tag{2.1}$$

The airflow (U) is three dimensional and consists of two horizontal components (v, u) and one vertical component (w), which leads to the following equation:

$$U^2 = |\mathbf{u}|^2 + |\mathbf{v}|^2 + |\mathbf{w}|^2, \tag{2.2}$$

$$U^2 = (\overline{\mathbf{u}} + \mathbf{u}')^2 + (\overline{\mathbf{v}} + \mathbf{v}')^2 + (\overline{\mathbf{w}} + \mathbf{w}')^2. \tag{2.3}$$

The governing equations in the ABL, the continuity, (2.4), and momentum equation 2.5, which are based upon the Navier-Stokes equation, can be derived using the equations (2.2 - 2.3).

$$\frac{\partial \overline{\mathbf{U_i}}}{\partial \mathbf{x_i}} = 0, \tag{2.4}$$

$$\frac{\partial \overline{U_i}}{\partial t} + \overline{U_j}\left(\frac{\partial \overline{U_i}}{\partial x_i}\right) = -\delta_{i3}g + f_c\varepsilon_{ijk}\overline{U_j} - \frac{1}{\rho_a}\frac{\partial \overline{p}}{\partial x_i} + v\frac{\partial^2 \overline{U_i}}{\partial x_j^2} - \frac{\partial \overline{(u_i'u_j')}}{\partial x_j}, \qquad (2.5)$$

where $x_i = (x, y, z)$, $U_i = (u, v, z)$, δ_{i3} is the Kronecker delta function, g is the gravitational acceleration, f_c is the Coriolis parameter, ε_{ijk} is the alternating unit tensor, ρ_a is the air density, p is the air pressure and v is the kinematic viscosity coefficient [10, 22, 23]. Note that in this thesis, we follow the right-hand side Cartesian coordinate system, where i, j, k respectively denote vectors along the $x-, y-, z$ axis. The description of all terms may be found in Table 2.1. The continuity and momentum equation is used to look at the transport of mass (continuity) and momentum within the atmosphere [15]. The last governing equation, the energy equation, can be found in Section 2.1.5.

Term	Description
$\frac{\partial \mathbf{U_i}}{\partial t}$	Storage of momentum
$U_j\left(\frac{\partial \mathbf{U_i}}{\partial x_i}\right)$	Advection of momentum
$\delta_{i3}g$	Gravity term
$f_c\varepsilon_{ijk}\mathbf{U_j}$	Coriolis term
$\frac{1}{\rho_a}\frac{\partial p}{\partial x_i}$	Pressure gradient force
$v\frac{\partial^2 \mathbf{U_i}}{\partial x_j^2}$	Viscous stress

Table 2.1: Description of each term of the momentum equation, assuming incompressibility.

The transfer of quantity per unit area per unit time, transfer fluxes, especially vertical transfer, is of interest when assessing the forces in the movement of air. The transport fluxes are split into x, y and z directions, corresponding to the wind components $\mathbf{u}, \mathbf{v}, \mathbf{w}$. In practical matters, these fluxes are directly measured using sonic anemometers. For this thesis, the eddy fluxes are in focus. Eddy fluxes contain a vertical gradient (w) of the quantity transported [15], where some common kinematic eddy fluxes are shown in Table 2.2.

Eddy flux	Description
$\overline{w'u'}$	Vertical kinematic eddy flux of horizontal momentum
$\overline{w'\theta'}$	Vertical kinematic eddy heat flux
$\overline{w'q'}$	Vertical kinematic eddy moisture flux

Table 2.2: Overview of some kinematic eddy fluxes.

2.1.4   Wind Profile

A wind profile describes the wind speed at different altitudes. Two of the most used wind profiles are the logarithmic wind profile and the power-law wind profile, where the IEC standard 61400-1 Ed.3 states the use of either of these wind profiles for load calculations on wind turbines [24]. The wind speed close to the surface is equal to zero due to surface friction between wind and the surface, in accordance with the law of the wall. The surface friction effect decreases with height and will no longer influence the wind when it becomes geostrophic (balanced between pressure gradients and Coriolis forces).

Power Law Wind Profile

The wind industry often uses the power-law wind profile due to its mathematical simplicity [25]. The wind profile is given as

$$U(z) = U(z_{ref})\left(\frac{z}{z_{ref}}\right)^{\alpha}, \tag{2.6}$$

where $U(z)$ is the wind speed at height z, $U(z_{ref})$ is the wind speed at the reference height z_{ref} and α is the wind shear coefficient relating wind speed at different heights. For marine environments, a shear coefficient of 0.14 is deemed appropriate [26].

Logarithmic Wind Profile

The logarithmic wind profile is widely used in the offshore wind industry [9]. The neutral logarithmic wind profile is given as [24]:

$$U(z) = \frac{u_*}{\kappa} ln\left(\frac{z}{z_0}\right), \tag{2.7}$$

where z_0 is the roughness length, u_* is the friction velocity, and κ is the von Karman constant. By including stability effects, the wind profile is given as

$$U(z) = \frac{u_*}{\kappa} \left[ln\left(\frac{z}{z_0}\right) - \Psi\left(\frac{z}{L}\right) + \Psi\left(\frac{z_0}{L}\right) \right], \qquad (2.8)$$

where Ψ is the stability corrections based on the Monin-Obukhov length L, described in Section 2.5.1.

Non-Dimensional Wind Profile

The non-dimensional wind profile is used to further look at the wind shear. By including the roughness parametrization to the non-dimensional wind profile, we can estimate the wind shear available at a given site. One of the most common roughness lengths was given by Charnock, which relates roughness length to wind stress [27, 28]. The standard dimensionless wind profile is given by [28]:

$$\frac{U}{u_*} = \frac{1}{\kappa} ln\left(\frac{z}{\overline{z_0}}\right), \qquad (2.9)$$

where z is the height in meters, $\overline{z_0}$ is the mean roughness length, U is the mean wind speed, κ is the von Karman constant and u_* is the friction velocity.

2.1.5 Turbulent Kinetic Energy

When looking at kinetic energy within the atmosphere, it is often interesting to look at turbulence. Using the turbulent kinetic energy budget equation, developed from the Navier-Stokes equation, provides an insight into the generation of wind turbulence. The equation consists of different terms given in Table 2.3. Each term corresponds to a different contribution to turbulent kinetic energy, where the importance of each term is situational.

The turbulent kinetic energy, TKE, is an important variable, and it is a direct measure of the turbulence in a flow. It is directly related to turbulent fluxes such as momentum, heat, moisture and pollutants and is closely related to the variances of the velocity components.

The definition of a turbulent flux is a parcel of fluid with different properties that are moved by turbulent eddies—the net flux results from averaging the transport by all the eddies over a given area. The turbulent fluxes are the same as the eddy fluxes and require a vertical gradient, W, of the transported quantity (heat, moisture, momentum, pollutant) [15]. Assuming that the coordinate system is aligned with the mean wind, that we have horizontal homogeneity and no subsidence, the turbulent kinetic energy equation can be written as:

$$\frac{\partial \bar{e}}{\partial t} = \frac{\overline{w'\theta_V'}}{\overline{\theta_V'}} g - \overline{u'w'} \frac{\partial \overline{U}}{\partial z} - \frac{\partial(\overline{w'e})}{\partial z} - \left(\frac{1}{\overline{\rho_a}}\right) \frac{\partial(\overline{w'p'})}{\partial z} - \varepsilon, \qquad (2.10)$$

$$\qquad\quad I \qquad III \qquad\quad IV \qquad\quad V \qquad\qquad VI \qquad\quad VII,$$

where $\bar{e} = \frac{1}{2}(\overline{(\mathbf{u'^2})} + \overline{(\mathbf{v'^2})} + \overline{(\mathbf{w'^2})})$, and $e = \bar{e} + e'$. In Table 2.3 the explanation of each term is shown.

Term	Explanation
I	Local storage or tendency of TKE
III	Buoyant production or consumption of TKE.
IV	Mechanical or shear productions off TKE.
V	Turbulent transport of TKE.
VI	Pressure correlation term
VII	Viscous dissipation of TKE. E.g. the conversion of TKE into heat is always a loss term.

Table 2.3: Explanations of the different terms in the Turbulent Kinetic Energy Budget Equation [15].

2.1.6   Buoyancy and Shear forces

Buoyancy and wind shear are the two dominant turbulence factors in the atmosphere, where the balance and strength of these two influence the entire ABL. Therefore, understanding these factors and their contribution is crucial when analyzing and working with wind energy. Rising hot air creates buoyancy forces. Buoyancy is either an upward-directed or downward-directed force exerted upon a parcel of fluid, e.g. air parcel, due to density differences between the parcel and surrounding fluid. Buoyancy is one of the critical features to creating mixing within the atmosphere and breaking up stratification [29]. In comparison, horizontal or vertical variations in the wind speed cause wind shear.

$$Buoyancy = \frac{\overline{\mathbf{w'}\theta'_{\mathbf{V}}}}{\overline{\theta'_V}}g, \tag{2.11}$$

$$Shear = \overline{\mathbf{u'w'}}\frac{\partial \overline{U}}{\partial z}, \tag{2.12}$$

where in equation (2.11); $\overline{\mathbf{w'}\theta'_{\mathbf{V}}}$ is the turbulent kinetic heat flux, g is the gravitational acceleration and θ'_V is the virtual potential temperature. In equation (2.12); $\overline{\mathbf{u'w'}}$ is the turbulent flux (reynolds stress) and $\overline{U}$ is the mean wind speed.

2.2   Marine Atmospheric Boundary Layer

Wind-wave interactions occur within the Marine Atmospheric Boundary Layer (MABL). The conditions and behaviour of this boundary layer are highly affected by water's high heat capacity and the presence of wind-generated waves and swells. Therefore, the processes in the MABL influence the wind profile and the intensity of the turbulent

forces. On a general basis, boundary layers are fluid layers in contact with boundaries of distinctly different physical characteristics. Therefore, based on the description, the MABL is where the ocean, or a large water surface, influences the atmospheric conditions, giving it different characteristics than boundary layers over land.

2.2.1   Structure

The structure of the MABL can be sorted into different sublayers, from micro to macro sizes, where each sublayer has its characteristics. The different sublayers are depicted in figure 2.3. In the lowest part of the MABL, we find the viscous sublayer, further mentioned in Section 2.3. Above this sublayer, we have the wave sublayer. The wave sublayer's order depends on the height of the waves and ranges from the ocean surface and up to five times the wave height. Above this sublayer, we find the constant-flux sublayer, which is in the order of 10 to 100 m. This layer is roughly 10% of the MABL. The last upper 90% consists of the Ekman layer, where the top of the layer reaches geostrophic winds. The MABL is usually shallower than the ABL and is generally in the order of 100 - 1000 m in depth [20].

There are many aspects of the MABL that are beyond the scope of this thesis, e.g. the creation of convective cells, the behaviour of surface roughness, and in-depth explanations of stability parameters. However, an overall understanding of its functions and characteristics is still highly relevant for offshore wind generation and can be found in "Wind Energy Meteorology" by Stefan Emeis [20].
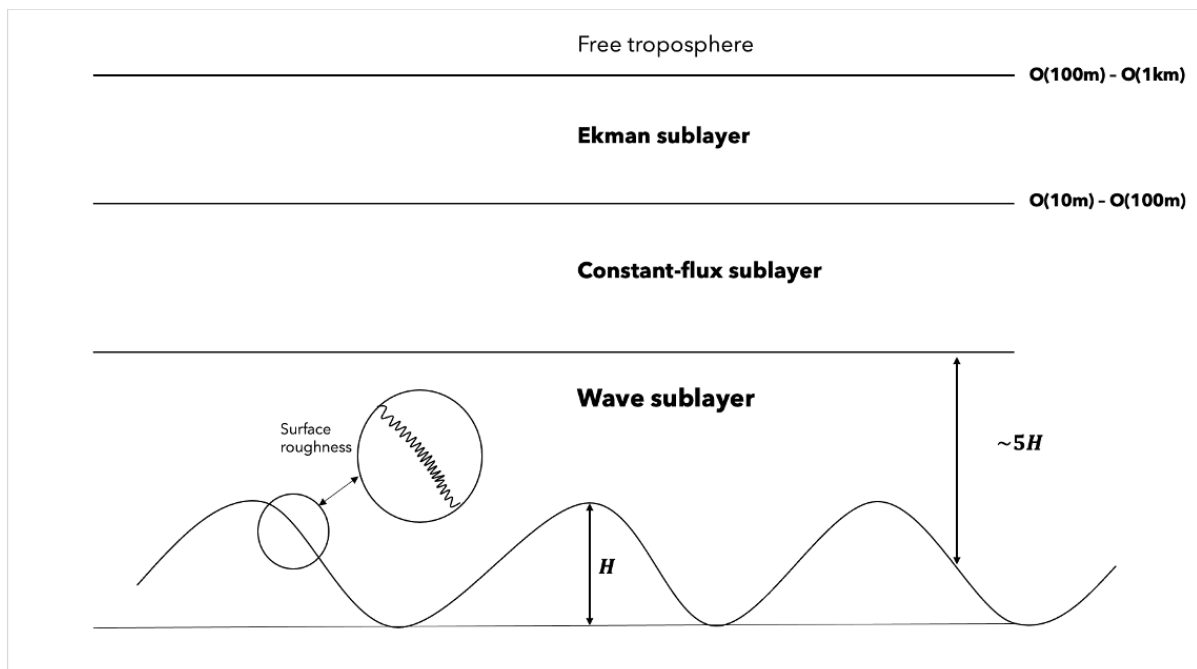
Figure 2.3: Vertical structure of the MABL, adapted from "Wind Energy Meteorology" [20].

2.3   Wave Boundary Layer

A good understanding of the Wave Boundary Layer (WBL) is necessary to fully under-
stand how waves influence the power generation for offshore wind parks. The WBL, the
lowest part of the MABL, is where surface waves affect the atmosphere. This bound-
ary layer occurs based on the conservation of momentum and energy, and its depth is
closely related to the wave height and might be in the order of 10 m [30]. Momen-
tum flux is essential for assessing the wind-wave interactions in the lower parts of the
MABL. The momentum flux is described by using the surface roughness length, which
again is parameterized by wind and wave parameters such as wind speed at 10 m (U_{10}),
inverse wave age u_*/C_p and wave steepness H_{m0}/L_p [23]. The parametrization of the
roughness length has been further improved in the later years, taking into account the
dependence of alignment between wind and waves [16]. The focus on improving this
parameter shows how important it is for the offshore industry to include the wind-wave
interactions in their calculations of offshore conditions. Insight into the primary param-
eters within the WBL is crucial for calculating the wind profile within this boundary
layer, where figure 2.4 show the flow geometry over a wavy surface.
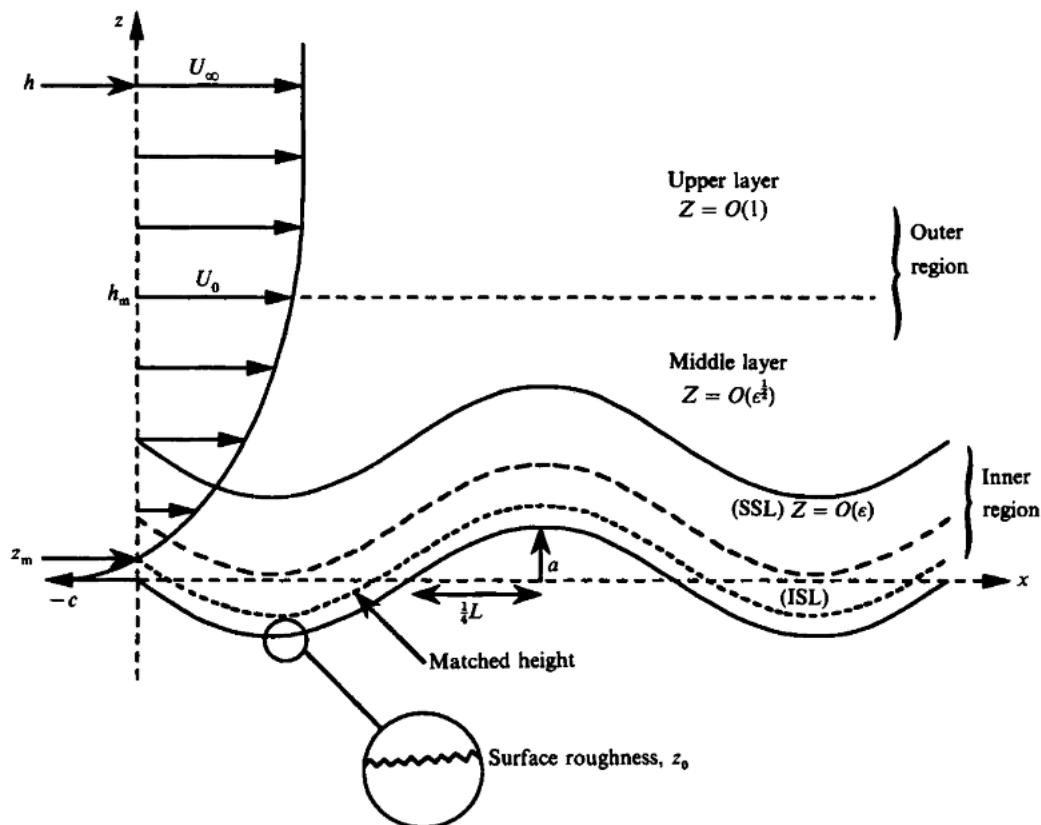
Figure 2.4: Flow geometry showing the wind flow over a wave [31].

2.3.1   Governing Equations

The governing equations used within the WBL describe waves and their behaviour.
Significant wave height, H_s, is defined as the average height of the highest one-third of

the waves and is given by:

$$H_s = \frac{1}{N/3} \sum_{i=1}^{N/3} H_i,$$ (2.13)

where N represents individual wave heights and H_i is a series of recorded wave heights, ranked in descending order. Further on, the wave period is given as:

$$T_p = \frac{1}{f_{wave}} = \frac{\lambda}{v},$$ (2.14)

where f_{wave} is the wave frequency, λ is the wavelength and v is the wave velocity. Together, H_s and T_p provides valuable information through wave spectrums, such as the JONSWAP spectrum [32].

Another governing equation for waves is the phase velocity, C_p, which describes the speed of the crest as the wave is moving. The following equation is based on the linear dispersion relation, such as C_p can be calculated using T_p [33]:

$$C_p = \frac{gT_p}{2\pi}.$$ (2.15)

The phase velocity is further used to determine the wave age, which is the ratio of surface wave phase speed to the wind speed and given as:

$$\chi = \frac{C_p}{U_{10}},$$ (2.16)

where U_{10} is the wind speed at 10 m. Over the sea surface the total kinematic stress is given as a combination of turbulent stress, τ_{turb}, wave-induced stress, τ_{wave} and viscous stress, τ_{visc} [34].

$$\tau_{tot} = \tau_{turb} + \tau_{wave} + \tau_{visc},$$ (2.17)

$$\tau_{turb} = -\rho_a \overline{u'w'},$$ (2.18)

where the viscous stress is assumed negligible as it is only essential millimetres above the ocean surface [34, 35]. During the development of waves, the wave-induced stress is positive and given as [34]:

$$\tau_{wave} = -\rho_a \overline{\tilde{u}\tilde{w}}, \tag{2.19}$$

where the tilde, $\tilde{\ }$, denotes the wave induced parameter, further explained in Section 2.4.1. According to the linear wave theory, the energy flux of waves is given as:

$$E_f = E\, C_g, \tag{2.20}$$

where for deep waters, the group speed, C_g, is

$$C_g = \frac{1}{2}C_p, \tag{2.21}$$

and the mechanical energy E, where A is the wave amplitude, is given as:

$$E = E_{kinetic} + E_{potential} = \frac{1}{2}\rho_a g A^2, \tag{2.22}$$

where $E_{kinetic}$ and $E_{potential}$ is given as:

$$E_{kinetic} = \frac{1}{2}mv^2, \tag{2.23}$$

$$E_{potential} = mgh, \tag{2.24}$$

where m denotes mass, g is gravity, v is the velocity and h is the height.

2.3.2 Wind-Generated Waves

The ocean's importance for the wind industry has grown as the focus has shifted from onshore to offshore energy generation. With insight into the critical factors within the wave sublayer and the governing equations listed, we can focus on wind-generated wave creation and -growth.

John W. Miles developed the Miles theory in 1957 [36], describing the mechanism behind the generation of wind waves from a flat surface. The physical interpretation of wind-wave generation is a flow domain consisting of two fluids with different densities. In respect to this thesis, these fluids refer to water and air. When air, which has a lower density than water, flows over the ocean, it starts to interact with the ocean due to the surface roughness of the ocean. Small ripples are generated, and if the wind force acts on the ocean surface over an extended period, these ripples will increase in amplitude and turn into wind-generated waves. Wave energy is highly dependent on the energy transferral between the atmosphere and the ocean [37].

Waves are categorized based on the water depth (h) and wavelength (λ). The three main categories are deep-, intermediate-, and shallow water waves, shown in Table 2.4.

Wave Category	Condition
Deep Water Waves	$0.5 < \frac{h}{\lambda}$
Intermediate Water Waves	$\frac{1}{20} < \frac{h}{\lambda} < 0.5$
Shallow Water Waves	$\frac{h}{\lambda} < \frac{1}{20}$

Table 2.4: Wave categories and their conditions.

Despite the different categories, waves have the same parameters as shown in figure 2.5.
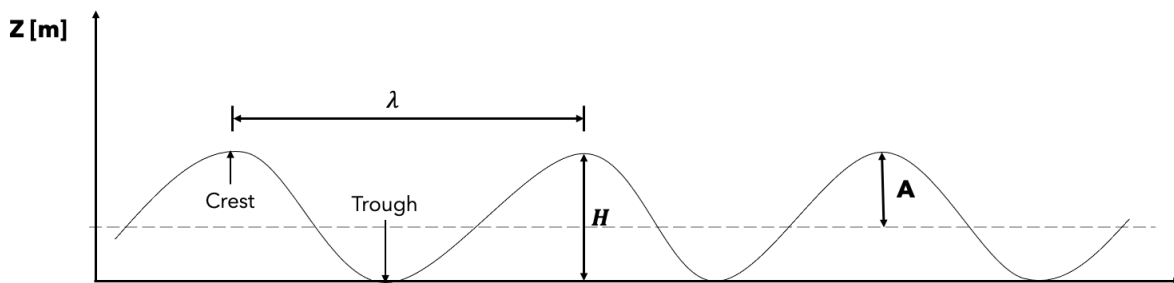
Figure 2.5: Wave parameters where H is the wave height, A is the amplitude, and λ is the wavelength. Adapted from Thauvin [32].

Energetic waves are, when created, categorized as wind-generated waves. As these waves propagate and move away from the energy source, they are called swell waves. These swell waves can, in some events, classify as a wave-driven wind regime. The characteristics of waves are determined by the strength of the wind, the duration of the wind blowing, and in which area of the ocean it occurs. In cases with strong winds over a long-time period, over large distances, the distance between each wave becomes more prolonged, and the energy "stored" in the waves increases. The waves lose energy as they propagate away from the wind source, causing them to dissipate eventually [38].

As the wind blows over the ocean, it changes the boundary layer above the ocean surface, thus affecting the surface roughness length. The surface roughness over the ocean is dependent on several factors, including the wind speed and alignments of the wind and wave. One of the most common ways to calculate the roughness length over the ocean is the Charnock method [27], which relates the roughness length to the wind stress [28]. Charnock defines the surface roughness as:

$$z_0 = a_c \frac{u_*^2}{g},\tag{2.25}$$

where a_c is the Charnock parameter, g is the gravitational acceleration and u_* is the friction velocity. The equation indicates that strong wind stress leads to higher waves,

resulting in a greater roughness length. The value of the Charnock parameter ranges from 8×10^{-3} to 6×10^{-2}, according to different literature's [28, 39, 40].

2.3.3   Swell

Swells are waves that have propagated away from the wind source that created them, indicating that they no longer depend on the wind's momentum and that they will not break within the generation zone [38]. Swell waves are low-frequency waves with a long wavelength that, on occasion, travel faster than the surface wind. Indicating that swell waves cause vertical transfer of horizontal momentum from the ocean to the atmosphere during low wind speeds[12, 38, 41]. The equation for wave age is used to classify wherever swell waves or wind-generated waves are present. Wave age is the ratio of surface wave phase speed to the wind speed, C_p/U_{10}. Measuring the strength of the wind forcing and wave growth. In event where $C_p/U_{10} > 1.2$, swell waves dominate [33].

2.3.4   Irregular Waves and JONSWAP

The linear wave theory is often used to simplify the mathematical understanding of the wave field. Surface gravity waves are three dimensional and nearly chaotic, in the sense that random appearances of the ocean surface cause records of measured waves never to repeat themselves exactly, as shown in figure 2.6. Due to superimposed wave fields, waves moving in succession differ in height, period, speed, and propagation direction [7]. Therefore, statistical tools are used to investigate how waves behave. One such tool created is the JONSWAP spectrum.

The JONSWAP spectrum was developed during the Joint North Sea Wave Project, where the project goal was to determine the structure of the source functions governing the energy balance of the wave spectrum [42]. The JONSWAP spectrum is a commonly used tool for research in the North Sea, used in several studies [10, 18, 23, 43–46]. It is common to look at the energy spectra when analysing waves, where wave energy is distributed in the frequency domain.

$$E(f) = \frac{\alpha g^2}{(2\pi)^4 f^5} \exp\left[-\frac{5}{4}\frac{f}{f_p}\right]^4 \gamma_e^{exp[-1/2[(f-f_p)/(\sigma f_p)]^2]}, \tag{2.26}$$

where f_p is the peak frequency of the wave spectrum, $\sigma = 0.07$ for $f \leq f_p$ and $\sigma = 0.09$ for $f \geq f_p$, $\gamma_e = 3.3$ and $\alpha = 0.0081$ [10].
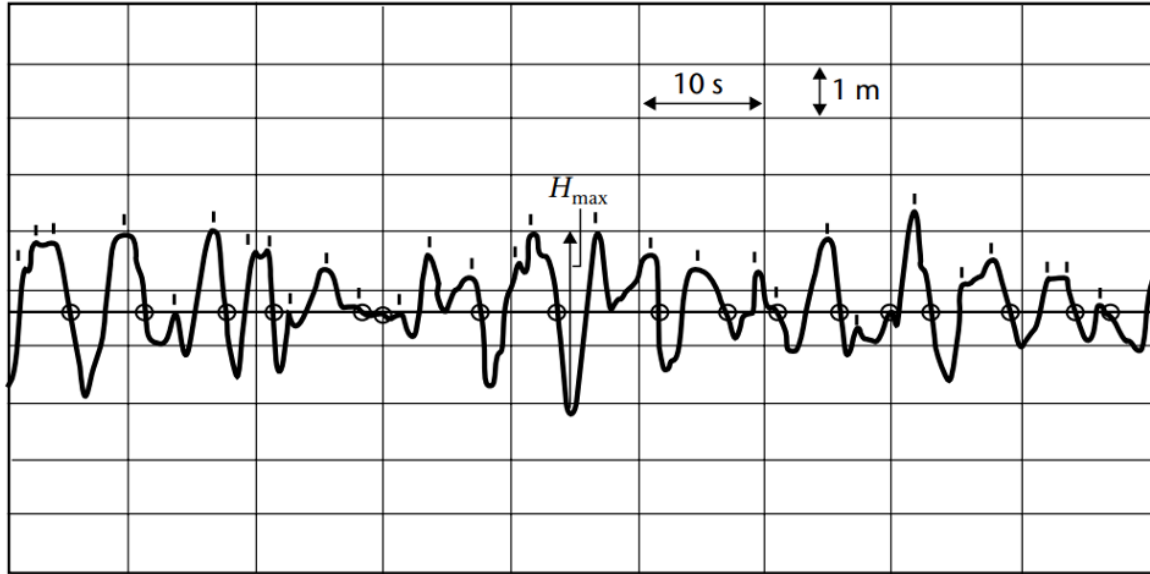
Figure 2.6: Visualization of the irregularity of ocean waves, where dashes (|) show the wave crest and the circles show the zero down crossing. Retrieved from the 2018 version of "Guide to Wave Analysis and Forecasting" [47].

2.4   Wind-Wave Interactions

The combination of wind and non-stationary waves introduces new aspects of understanding momentum and energy exchanges in the air-sea interface. This thesis will focus on two types of wind-wave interactions; (1) misalignment between wind and wave and (2) vertical transfer of momentum events. As mentioned in Section 2.3.2, the wind exerts a downward directed force towards the ocean, and waves exert an upward directed force towards the atmosphere. Thereby exchanging momentum between the air-sea interface. Wind-wave interactions mainly occur within the lowest part of the MABL, and numerical studies have suggested that waves can impact the wind field up to the hub height of a wind turbine [16].

2.4.1   Governing Equations

As mentioned in Section 2.1.3 the governing equations in the atmosphere are the continuity (2.4), momentum (2.5) and energy equations (2.10). These must be modified when moving from the ABL into the MABL [10, 22, 23, 46, 48]. The presence of surface gravity waves adds another term when decomposing the wind. One must account for effects caused by waves using the momentum and energy equations [10, 11]. In the ABL, as shown in Section 2.1.3, conditions can be described by the decomposed wind consisting of a mean variable and a turbulent variable, while over surface waves, it is written as:

$$\mathbf{u} = \overline{\mathbf{u}} + \mathbf{u}' + \tilde{\mathbf{u}}, \tag{2.27}$$

$$U^2 = (\overline{\mathbf{u}} + \mathbf{u}' + \tilde{\mathbf{u}})^2 + (\overline{\mathbf{v}} + \mathbf{v}' + \tilde{\mathbf{v}})^2 + (\overline{\mathbf{w}} + \mathbf{w}' + \tilde{\mathbf{w}})^2, \tag{2.28}$$

and the newly introduced $\tilde{\mathbf{u}}_{\mathbf{i}}$ is the wave fluctuation.
Given this decomposition the total kinetic energy within the wind is given as:

$$e = \frac{1}{2}\mathbf{u_i u_i} = \overline{e} + e' + \tilde{e}, \tag{2.29}$$

and the mean kinetic energy is given as:

$$\overline{e} = \frac{1}{2}\overline{\mathbf{u_i u_i}} + \frac{1}{2}\overline{\tilde{\mathbf{u}}_{\mathbf{i}}\tilde{\mathbf{u}}_{\mathbf{i}}} + \frac{1}{2}\overline{\mathbf{u}'_{\mathbf{i}}\mathbf{u}'_{\mathbf{i}}}. \tag{2.30}$$

Based on Hara and Belcher [22], the continuity and the energy budget equation are given as:

$$\frac{\partial \tilde{\mathbf{u}}_{\mathbf{i}}}{\partial \overline{x_i}} = 0, \tag{2.31}$$

$$\frac{d}{dz}(\overline{\mathbf{u}}\tau_{tot}) + \frac{d\prod}{dz} + \frac{d\prod'}{dz} - \rho_a \varepsilon = 0, \tag{2.32}$$

where $\prod$ is the vertical transport of kinetic energy based on wave-induced motions:

$$\prod = -\overline{\tilde{\mathbf{w}}\tilde{p}} - \rho_a \overline{\tilde{\mathbf{u}}_{\mathbf{i}}(\widetilde{\mathbf{u}'_{\mathbf{i}}\mathbf{w}'_{\mathbf{i}}})}, \tag{2.33}$$

and $\prod'$ is the vertical transport of TKE:

$$\prod{}' = -\overline{\mathbf{w}'p'} - \frac{\rho_a}{2}\overline{\tilde{\mathbf{w}}(\widetilde{\mathbf{u}'_{\mathbf{i}}\mathbf{u}'_{\mathbf{i}}})} - \frac{\rho_a}{2}\overline{\mathbf{w}'\mathbf{u}'_{\mathbf{i}}\mathbf{u}'_{\mathbf{i}}}, \tag{2.34}$$

ρ_a and ε is, respectively, the air density and the viscous dissipation rate.

$$\varepsilon(z) = \frac{|\overrightarrow{\tau_{tot}}(z)/\rho_a|^{\frac{3}{2}}}{\kappa z}. \tag{2.35}$$

Momentum exchange between the ocean surface and the atmosphere is one key parameter to investigate during wind-wave interactions. The equations presented in this subsection is based upon studies by Semedo et al., Paskyabi et al., Semedo, Hanley et al., Flügge et al. and Grachev et al. [10, 11, 34, 35, 41, 49]. In the lower layer of the MABL, the wave-induced stress, τ_{wave}, is dependent on the wave age, given in Section 2.3.1. In situations where wind-generated waves dominates, $C_p/U_{10} < 1.2$, the stress related to waves is positive and directed downwards ($\tau_{wave} > 0$). This wave-induced stress, τ_{wave} is a part of the total stress contribution acting on the air-sea interface,

where the total stress, τ_{tot}, is given as:

$$\tau_{tot} = \tau_{turb} + \tau_{wave} + \tau_{visc}. \tag{2.36}$$

The viscous stress, τ_{visc}, is assumed negligible as it is only important directly above the ocean surface (order of millimeters). This gives the following relation of the total stress:

$$\tau_{tot} = \tau_{turb} + \tau_{wave}. \tag{2.37}$$

In situations where the wave phase speed exceeds the wind speed, $C_p/U_{10} > 1.2$, the wave-induced stress becomes negative, and the wave-induced stress flux is then directed upwards. If the wave age value surpasses $C_p/U_{10} > 1.2$ the vertical transport of horizontal momentum will be negative, i.e. a vertical transfer of horizontal momentum from the ocean surface to the atmosphere (upward). As we are interested in the vertical momentum transfer between the air-sea interface, the wave-induced stress and turbulent stress are given as:

$$\tau_{wave} = -\rho_a\Big(\big\langle \tilde{u}\tilde{w}\big\rangle i + \big\langle \tilde{v}\tilde{w}\big\rangle j\Big), \tag{2.38}$$

$$\tau_{turb} = -\rho_a\Big(\big\langle \mathbf{u}'\mathbf{w}'\big\rangle i + \big\langle \mathbf{v}'\mathbf{w}'\big\rangle j\Big). \tag{2.39}$$

The total stress is thus given as:

$$\tau = -\rho_a\big\langle \mathbf{u}'\mathbf{w}' + \tilde{u}\tilde{w}\big\rangle i - \rho_a\big\langle \mathbf{v}'\mathbf{w}' + \tilde{v}\tilde{w}\big\rangle j = \tau_x + \tau_y. \tag{2.40}$$

This equation can be simplified when $C_p/U_{10} < 1.2$ as for wind-generated waves, the y-directional stress is negligible (as the wind is what contributes to wind-wave interaction). Moreover, since the wave-induced stress decreases exponentially with height, the wave-induced stress is only valid within the WBL.

2.4.2 Wind Profile - Over the Ocean

Different wind profiles and equations for calculations of wind profiles have been proposed in several studies, and each profile has its benefits and drawbacks. Even though vertical wind profiles over land is typically calculated using a logarithmic approach (2.1.4), it has been found unfavourable over the ocean [16, 22], due to the interactions between the ocean and the atmosphere. Based on the WBL model formulation given by Hara and Belcher[22] and Moon et al. [46], the wind profile near an ocean surface can be expressed as:

$$\frac{d\vec{u}}{dz} = \begin{cases} \frac{u_*}{\kappa z}\frac{\vec{\tau_{tot}}}{|\vec{\tau_{tot}}|} & \text{if} \quad z \geq \frac{g\delta}{\sigma_{min}^2}, \\[3mm] \left[\frac{\delta}{z^2}\widetilde{F_w}(\sigma = \sqrt{g\delta/z}) + \frac{\rho_a}{\kappa z}\left|\frac{\vec{\tau_{turb}}(z)}{\rho_a}\right|^{\frac{3}{2}}\right] \times \frac{\vec{\tau_{turb}}(z)}{\vec{\tau_{turb}}(z)\vec{\tau_{tot}}} & \text{if} \quad \frac{g\delta}{\sigma_{max}^2} \leq z < \frac{g\delta}{\sigma_{min}^2}. \\[3mm] \frac{\rho_a}{\kappa z}\left|\frac{\vec{\tau_{visc}}}{\rho_a}\right|^{\frac{3}{2}} \times \frac{\vec{\tau_{visc}}}{\vec{\tau_{visc}}\vec{\tau_{tot}}} & \text{if} \quad z_v \leq z < \frac{g\delta}{\sigma_{max}^2}. \end{cases}$$

(2.41)

Component	Explanation
τ_{tot}	Total stress
τ_{turb}	Turbulent stress
τ_{visc}	Viscous stress
ρ_a	Air density
u_*	Friction velocity
κ	von Karman constant
$\sigma_{max/min}^2$	Max/Min wave spectrum radian frequency
z_v	Viscous sublayer roughness length
$\tilde{F}_w$	Vertical decay function
δ	Empirical coefficient, O(0.01) [46]

Table 2.5: An explanation of the components of the wind profile equation 2.41 [22, 23].

[23]

Each parameter in equation 2.41 are described in Table 2.5. Looking at equation (2.41) we see that the wind profile, and thereby the height dependent wind speed, is dependent on which sublayer it is located in. Starting from the ocean surface and moving upwards, we divide the atmosphere into three sublayers; (1) Viscous sublayer, (2) Wave sublayer and (3) Atmospheric sublayer. From the wind profile equation, we see that in the viscous sublayer, at a height between the viscous height, Z_v, and $g\delta/\sigma_{max}^2$, the wind speed is dependent on the viscous stress. Moving upwards to the wave sublayer, we see the wind speed is dependent on the turbulent stress, which contributes to the wave growth [23]. Above the waves and the wave sublayer, the wind speed is dependent on the total stress. As the equation above indicates, a wind profile used over land may not be sufficient over the ocean. The air-sea interaction between the ocean and the atmosphere influences the wind profile.

2.4.3   Wave Induced Low-level jet

The wave-induced low-level jets, WI-LLJ, can be described as an air current found on top of the WBL, at height $0.1/k_p$ where k_p is the wavenumber of the waves at the peak in the spectrum [38]. WI-LLJ is thought to be a characteristic of wave-driven

wind regimes [35], together with fast travelling swell waves and upward transfer of horizontal momentum. In events with fast travelling swells aligned with light wind conditions and where the vertical transfer of horizontal momentum is directed upwards (from the ocean to the atmosphere), the wind near the surface accelerates, creating a WI-LLJ [12, 41]. Sullivan et al. [50] showed, based on a large eddy simulation (LES) that during certain circumstances, the generation of WI-LLJ results in a near-collapse of the turbulence above the waves, indicating that swell waves can affect the whole MABL. Further on, studies by Semedo et al. [34], and Hanley et al. [35] have also shown that this WI-LLJ, caused by swell waves, can change the wind field throughout the MABL. The occurrence of a WI-LLJ increases the Coriolis force within the boundary layer, causing the wind to turn in the opposite direction to the classical Ekman layer.
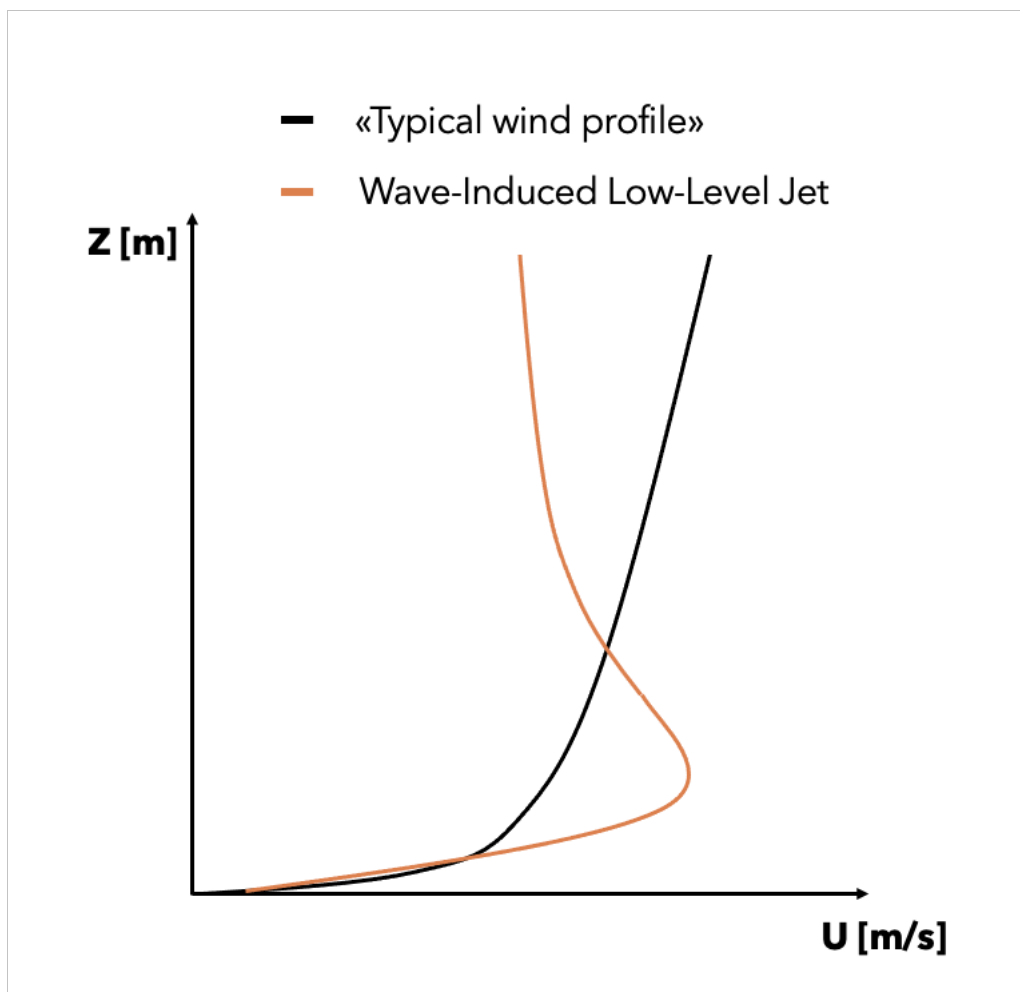
Figure 2.7: A visual representation of a WI-LLJ compared to a typical wind profile, where the height of WI-LLJ occurs at $0.1/k_p$. The k_p is the wavenumber of the waves at the peak in the spectrum. Adapted from "Low-level jets over the north sea based on ERA5 and observations: Together they do better" by Kalverla et al.[51].

During events with WI-LLJ, the vertical wind profile will no longer exhibit a logarithmic shape, as the acceleration of the airflow will generate a wave-driven wind maximum. This indicates that the logarithmic wind profile fails to describe the observed wind speed adequately. Therefore, a WI-LLJ is identified by investigating if there are

any local maximums [34] in the wind profile, as shown in figure 2.7. Additionally, the wave age is a good indicator of the direction of the vertical transfer of horizontal momentum and thereby a first indication of a WI-LLJ [35].

2.4.4   Wind-Wave Regime

In offshore wind energy, there are two main wind-wave regimes of interest; wind-generated waves and wave-driven winds. How these regimes influence the vertical wind profile and thereby the wind resource potential is not fully understood. Recent studies show that the different wave regimes may increase and decrease the observed wind profile, depending on the alignment between wind and waves [16].

Several studies have shown the importance of swell waves and their effect on the wind speed, depending on the alignment between the wind and wave directions. Situations with aligned wind waves may increase the wind speed, and opposed wind-wave may decrease the wind speed [11, 33, 52]. To categorize wind-generated waves and wave-driven winds, wave age has regularly been used and is suggested as an appropriate parameterization as it highly depends on the peak phase speed of the wave field and the wind speed [33].

As described by Porchetta et al. [16] and Yousefi et al. [53], the wind-wave interactions are dependent on the shear stress forcing, where the total shear stress in the MABL is mainly affected by the wave shear stress and the turbulence shear stress. Furthermore, the wave shear stress is highly dependent on the wave age, equation (2.16). The connection between the wave age and the wind-wave regimes is given in Table 2.6.

Condition	Regime
$\frac{C_p}{U_{10}} < 1.2$	Wind-generated waves regime
$\frac{C_p}{U_{10}} = 1.2$	Fully developed sea
$\frac{C_p}{U_{10}} > 1.2$	Wave-driven wind regime

Table 2.6: The wind-wave regime based upon the wave age.

As mentioned in Section 2.4.3, a study by Hanley et al. [35] indicated the presence of a WI-LLJ directly above the propagating waves. This WI-LLJ is identified using the classical Ekman model, with a term representing the wave-induced stress, where upward transfer of horizontal momentum accelerates the WI-LLJ. This affects the entire MABL due to an increase in the Coriolis force. Therefore, in events with an upward momentum from the ocean to the atmosphere, different wind conditions are expected compared to events with downward momentum [38]. Two factors determine the structure of wave-induced airflow and the resultant momentum exchange. (1) The effect of

the critical layer, defined as the height where the wind speed equals the wave celerity, and (2) the wave-induced turbulent stress [54]. These wind conditions might affect the energy generation from wind turbines, the dynamic loads and the fatigue due to the changes in the vertical wind profile, as shown in figure 2.8.
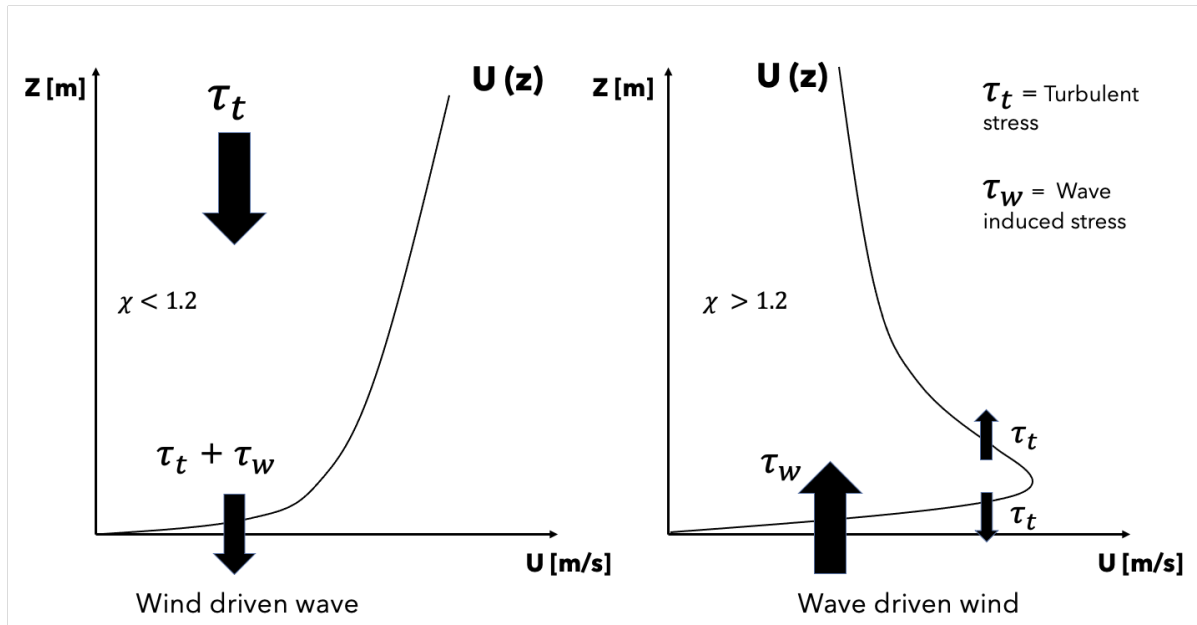
Figure 2.8: Visualization of wave regimes, where we have strong winds over slow waves for wind-generated waves and for wave-driven wind, we have weak winds over fast waves. χ indicates the wave age. Adapted from Hanley and Belcher [31, 35].

2.4.5   Wind-Wave Alignment

As defined by van Vledder [17], wind-wave misalignment is a temporal difference between the wind direction and the mean wave direction of wind-generated waves. As wind creates waves, it would be natural to assume that the wave direction follows the wind direction. However, in many cases, this is not true, as shown by multiple studies [8, 11, 16–18, 43, 55–58]. Some common factors leading to wind-wave misalignment are waves propagating from another area not affected by the local wind, i.e. swell waves, and the inertia of the ocean. In situations where swell waves are present, one can expect some level of wind-wave misalignment, where the period of these misalignments depends on the wind speed and its mean direction.

Studies on wind-wave misalignment [8] provide indications that aligned wind and waves result in higher wind speeds stretching up to wind turbine hub height, resulting in higher power generations, compared to situations where there are no waves. Conversely, in events of opposed wind and waves, a study by Patton et al. [59] showed a 15% decrease in wind speed at 100 m. These results show the importance of wind-wave (mis)alignments in power generation.

Furthermore, wind-wave alignments are also crucial for load analysis of wind turbines, where misaligned- and opposed wind waves induce increased fatigue damage on

the sub-structures of a wind turbine [44]. The distribution of wind-wave alignments varies from area to area, and a study by Haghayeghi et al. [57] showed that for the Hy-Wind Scotland site, the most extreme winds and waves might act in opposite directions. Hence, consideration of directional dependencies of metocean conditions for the analysis and design of marine structures, such as offshore wind turbines, is crucial. A study by Kalvig et al. [60] investigated wind turbine fatigue caused by wave-influenced wind and found that during relatively low wind regimes (with a reference wind of 8 m/s at 400 m height), and especially during opposed wind waves, the wave-influenced wind increased the fatigue damage on the turbine, compared to situations with no waves.

Wind-wave alignment is calculated by comparing the wind direction to the wave direction. To easier distinct between the level of alignments, the following characteristic is proposed in Table 2.7:

Condition	Regime
$|\theta| < 30$	Aligned
$30 < |\theta| < 135$	Misaligned
$|\theta| > 135$	Opposed

Table 2.7: The wind-wave regime based upon the wave age, where θ is the angle between the wind- and wave direction.

2.5   Stability Regimes

Specific interactions within the MABL cause heat, mass, and momentum to be transferred between the ocean surface and the atmosphere. Due to the diurnal cycle of day and night and the seasonal cycle from winter to summer, we can expect to find different conditions inside the MABL depending on the time of day and time of year. The exchange process, or boundary layer transport, is responsible for the stability conditions in the MABL.

There are three stability regimes which are used to categorize the processes within the atmosphere [28]. These can be distinguished depending on the dominant source of turbulence. In figure 2.9, the affect stability has on the wind profile is shown.

The stable regime refers to air, which is statically stable. This process suppresses buoyancy generation and typically leads to a regime characterized by small eddies and strong wind shear.

The turbulence is mainly driven by thermal differences in the unstable regime, creating buoyancy forces. The turbulence is induced due to heat transfer from the ground, where warm air pockets rise and shove the cold air surrounding it away. The warm air continues to rise until it reaches an inversion zone, where the temperature of the air pocket equals the temperature surrounding it. As the warm air pocket rises, it will break through stratification in the atmosphere and cause the air to mix. This regime is characterized by large turbulent eddies created by buoyancy forces.

The neutral regime is the most beneficial and ideal for wind energy extraction, and studies [9] have yielded results suggesting that neutral stratification gives the lowest fatigue damage on the rotors. This regime is characterized by strong wind shear and a heat flux close to zero.
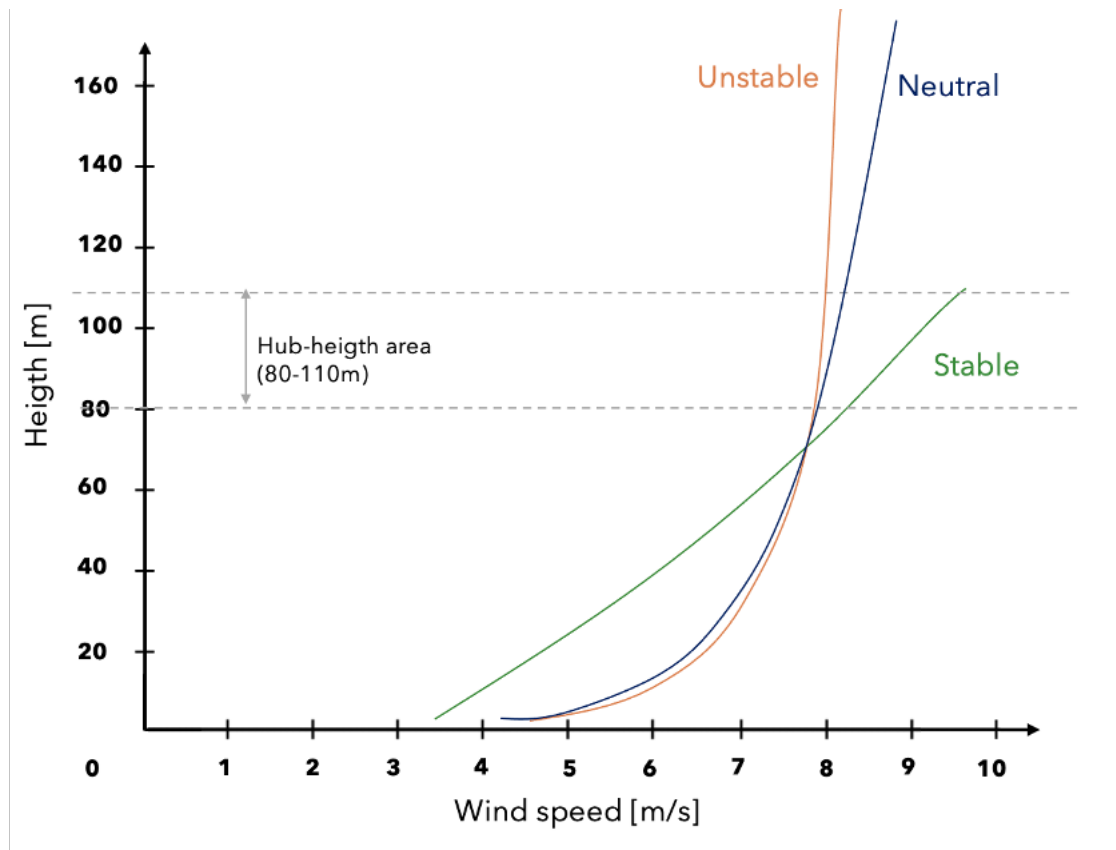
Figure 2.9: Influence of stability conditions on a wind profile, adapted from "Influence of Atmospheric Stability Variation on Uncertainties of Wind Farm Production Estimation" [61].

2.5.1 Monin-Obukhov Length Scale

Wind shear has been proven to rely strongly on atmospheric stability, where wind shear profiles which do not consider the atmospheric stability strongly deviate from those where it is considered. Generally, the atmosphere tends to become neutrally stratified for strong wind speeds. However, Holstag et al. found that there are a significant amount of non-neutral stability observations even at strong wind speeds [24]. Therefore, categorizing these stabilities and a good understanding may prove crucial when analyzing wind-wave interactions coupled with power generations.

The Monin-Obukhov length, also called Obukhov length, is used to categorize these stabilities. Monin-Obukhov length was first described by Obukhov in 1946 and has since then been commonly used to describe the different contributions to TKE from buoyancy and wind shear. As mentioned in Section 2.1.5, the turbulent kinetic energy is a direct measure of the turbulence in a flow.

Monin-Obukhov length scale, L_{Mo}, is one of the most common scaling parameters for the atmospheric layer, and it can be described as a parameter that is proportional to the height above the surface where buoyancy first dominates over the mechanical shear forces. Therefore, it is also a critical length scale and is often used in similarity scaling of turbulence in the mixing surface layer. In the atmosphere, we assume that above L_{Mo} we have buoyancy forces dominating the turbulence production, whereas below, we have wind shear or mechanical shear forces dominating [62].

The L_{Mo} is derived from the TKE budget equation and is defined as:

$$L_{Mo} = -\frac{\overline{\theta_v} u_*^2}{\kappa g \theta_*},$$
(2.42)

where κ is the von Karman constant, g is the gravitational acceleration, u_* is the friction velocity and $\overline{\theta_v}$ si the mean virtual potential temperature. During events with strong wind, we expect the L_{Mo} to be high and the wind shear to dominate the turbulent kinetic energy production. The opposite holds true for none to light wind, where we expect the L_{Mo} to be lower and buoyancy forces to be higher.

The Monin-Obukhov length is used to estimate the atmospheric stability in our data. The stability influences the wind shear, and it is an essential factor that needs to be included when analyzing the wind. Studies [13] have shown that the atmospheric stability impacts the power output from turbines when the wind speed during stable conditions is higher than the wind speed at strongly convective conditions. Wharton et al. [13] showed an average power output difference of 15%, depending on the stability.

There are different ways to classify the atmosphere's stability, and many studies rely on the Monin-Obukhov length. Some studies also rely on the Richardson number [63] or other methods. In this thesis, we will use Monin-Obukhov length and classify the different stabilities as shown in Table 2.8.

Class Name	Class Boundaries
Unstable (U)	-500 < L < 0
Neutral (N)	|L| > 500
Stable (S)	0 < L < 500

Table 2.8: Stability classes and its boundaries, based on Monin-Obukhov length [24].

2.6   Wind Energy Power Generation

To fully utilize a wind-wave analysis with respect to wind energy application, understanding the basics behind a wind turbine is crucial. In Table 2.9, the most important terms for wind turbines are presented. Wind turbines can mainly be categorized into horizontal-axis and vertical-axis, where the horizontal-axis turbine is most commonly used. Both the horizontal- and the vertical wind turbine utilizes the same concept of

transforming moving air into electricity by transforming the kinetic energy within the wind into mechanical energy. This occurs when the moving air flows over the wind turbine blades, forcing them to move. How this energy is transformed into electricity can best be explained by looking at the typical design of a wind turbine.

Term	Explanation
Rated Wind Speed	The wind speed where rated power is reached
Rated Power	The turbines generating capacity
Cut-in Speed	The minimum wind speed needed to generate power
Cut-off speed	The maximum wind speed the generator can handle
Efficiency	Ratio of energy generated from available energy source

Table 2.9: A short table explaining the most important terms for wind turbines.

2.6.1   Horizontal-Axis Wind Turbine Design

A typical horizontal-axis wind turbine consists of a nacelle, a tower and a rotor. In cases where the wind direction differs from the wind turbine direction, a yaw control can move the nacelle and the rotor to face the incoming wind. When the rotor is aligned with the wind direction, with the wind blowing over the rotor blades, the rotor starts to turn. This rotation is then transferred to a shaft within the nacelle. In older turbines, this shaft is further connected to a gearbox, which primary function is to turn the low turning speed (round per minute, rpm) of the wings into a high turning speed (rpm). With a high rpm, the generator can generate electricity. Newer wind turbines skip the gearbox, as they tend to require more maintenance than the rest of the turbine, and instead use a gearless generator. This generator is fed a rotation that equals the rotation of the wing and generates electricity by magnetic direct drive generators.

The wind turbine blades themselves can turn due to their design. Each blade consists of a combination of different airfoils, with the primary objective being to ease the rotation of the rotor. The rotor blades use the same principles as wings on airplanes to create lift forces. The difference is that airplanes utilize the airfoils to ascend from the ground, while the wind turbine blades utilize the lift forces to rotate the rotor. When a rotor blade is parallel to the wind speed, the wind flow will divide and move around the blade. If the angle of attack, the angle between the mean wind flow and the blade, increases, the wind flow will be disturbed, resulting in increased lift forces. The physical explanation for this lift force is based on basic fluid mechanics. Bernoulli's principle states that when the velocity of a fluid decreases, the pressure increases. Therefore, when the wind flow is divided by the blade, it creates a high pressure underneath the blade and a low pressure above the blade. This creates a suction, i.e. lift force, which

helps the wind rotor blades turn. The amount of lift force is determined by a blade-pitch controller, which at all times tries to maximize the potential power generation from the kinetic energy within the wind.

2.6.2   Energy Extraction

The amount of energy a wind turbine can generate depends on the wind speed, the blade swept area, the limitations of the generator and the Betz law. Betz law is the theoretical maximum efficiency a wind turbine can have and is based upon momentum conservation and Bernoulli's equation. The principle behind this efficiency is that to gain 100% efficiency; one would have to extract all the kinetic energy from the wind, which would not be possible since we need the wind flow to move over and past the blades to generate rotation. Betz limit can be calculated as,

$$Cp_{max} = 4a(1-a)^2 = 16/27 = 0.59, \tag{2.43}$$

where a is the fractional decrease in wind velocity between the wind flow and the turbine rotor, or the axial induction.

By including betz limit the maximum power possible to extract from the wind is:

$$P_{max} = 1/2C_P\rho_a AU^3, \tag{2.44}$$

where U is the mean wind speed, ρ_a is the air density, and A is the blade swept area. Besides increasing the efficiency of wind turbines, the blade swept area is the only way to increase the maximum power, leading to incentives for larger wind turbines. The blade swept area can be calculated as

$$A = \pi r^2, \tag{2.45}$$

where r is the length of the blade. In figure 2.10, the swept area of an horizontal-axis wind turbine is shown, where D is given as the diameter.
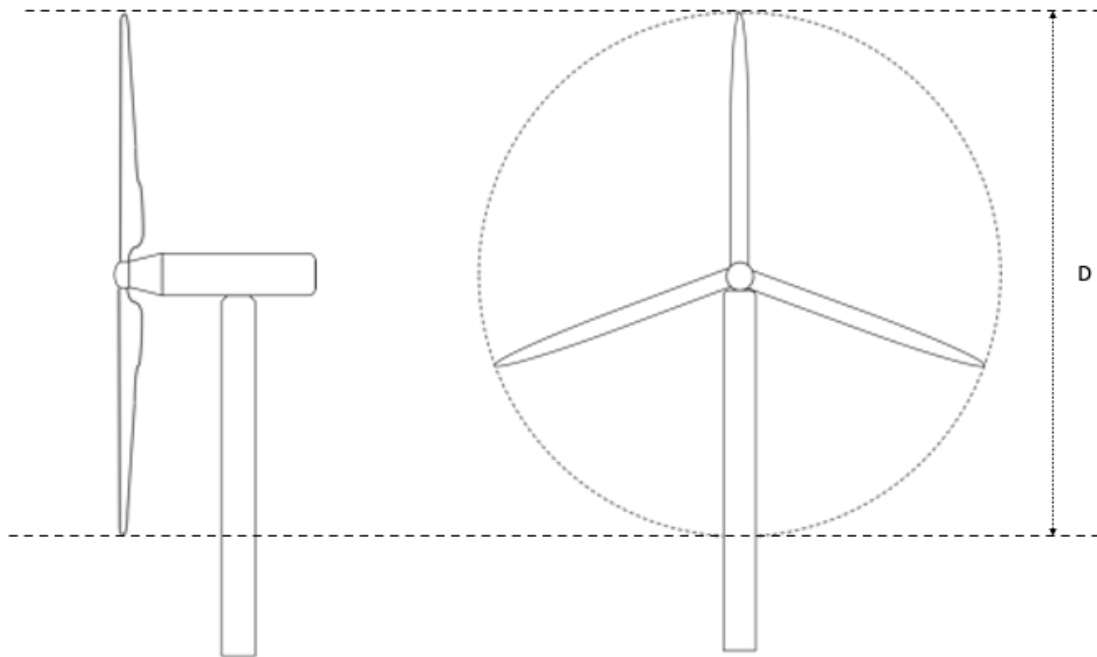
Figure 2.10: Sketch of a Horizontal-axis wind turbine visualizing the swept area, where D is the diameter of the swept area, or double the blade length.

Another important aspect for the wind energy industry is the wind power density, categorized by W/m^2. Wind power density is a method to evaluate the wind resources available at a given site, and is a measurement of available wind energy (P) per square feet of blade swept area (A), given as:

$$P_D = P/A, \tag{2.46}$$

where the available wind energy is given as:

$$P = \frac{1}{2}\rho_a U^3.$$

2.6.3   Power Curve

Based on equation (2.44) a theoretical power curve, also called the ideal power curve, can be created for each wind turbine. This theoretical power curve shows the potential power generation based on the available wind speed.
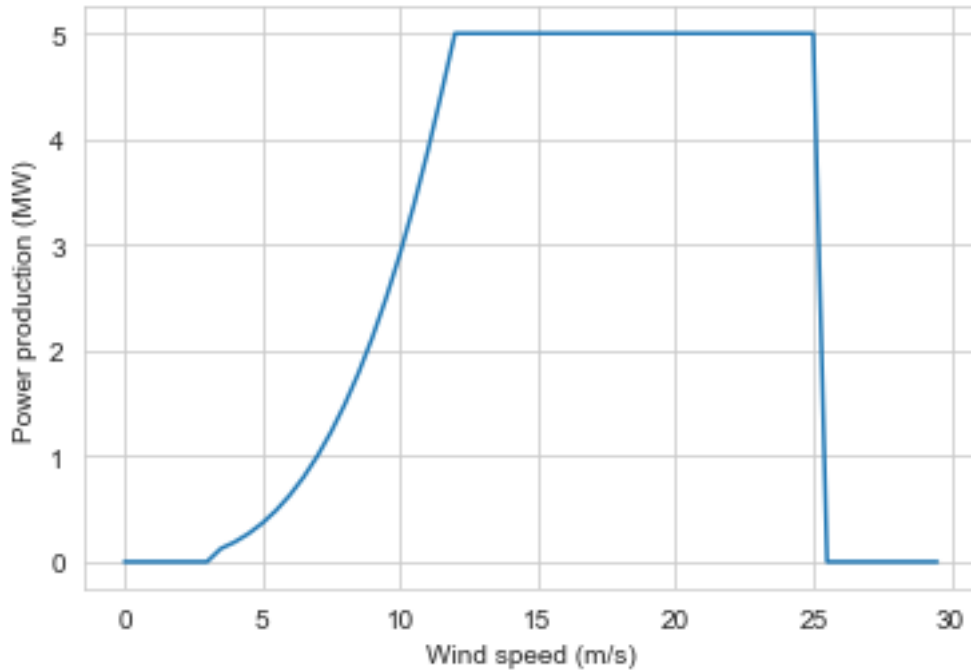
Figure 2.11: A theoretical power curve, or ideal power curve, with an efficiency at 40%, cut-in speed at 3.5 m/s, cut-off speed at 25 m/s.

The theoretical power curve, as shown in figure 2.11, is calculated using the power equation (2.44), where the Betz limit is exchanged with the efficiency of the wind turbine. However, an actual power curve is calculated differently, as it relies on actual data output from a functioning wind turbine. An actual power curve would underperform compared to the theoretical due to environmental conditions affecting the wind flow and operational demands.

2.6.4 Turbine and Site Performance

Indications of how well a wind farm site is utilized or how effective a turbine is operated can be validated using a capacity factor. The capacity factor measures the actual power generated (P_{actual}) compared to the theoretical maximum possible (P_{max}), and is given as:

$$CF = \frac{P_{actual}}{P_{max}}, \tag{2.47}$$

where a CF of 1.0, or 100%, indicates that the turbine is constantly generating following the ideal power curve. From the capacity factor, one gains information about the run-time of a turbine, which again includes information about a turbine's down-time and wind speeds outside the generation range of a turbine.

A more straightforward way to validate the turbine performance is to examine the deviation from a theoretical power curve. All turbines have a theoretical power curve provided by the manufacturers. This power curve indicates how much power is generated based on wind speed, indicated in figure 2.11. By comparing actual data to the theoretical power curve, one can identify events where the turbine is underperforming or overperforming. This information can even indicate how different interactions impact power generation.

2.6.5 Control System

Wind turbines have their own control system. The primary purpose of this system is to maintain the turbine's health and maximize the energy extracted from the wind. There are two central systems designated for this: the pitch and yaw systems.

Pitch System

The primary purpose of the pitch system is to change the angle of the turbine rotor blades to maximize the power output and to protect the wind turbine at higher wind speeds by creating a stall [64]. Looking at the power curve in figure 2.11 one can see the effect of the pitch system when the wind speed is between 13 m/s and 25 m/s. At this point, the power generation is stable while the wind speed increases. Therefore, the rotor speed is controlled by changing the angle of the blades.

Yaw System

Horizontal-axis wind turbines are designed to be faced perpendicular to the wind direction, causing them to rely on yaw systems to adjust to changes in wind direction. As the wind direction changes, a motor turns the nacelle and the blades in the direction of the wind.

Curtailment

As wind energy can only be generated when the wind is blowing and the complexity of the electricity grid demands an instantaneous balance in demand and supply, wind turbines might often experience curtailment. Curtailment is when the electricity generation from a wind turbine is restricted due to system operation demands.

2.6.6   Prediction of Power Generation

Wind analysis is crucial for the wind industry due to the concept of preventive maintenance. Preventive maintenance is based on predicting the site conditions, where data collection from both the wind turbine and the environment is crucial. Moving wind parks from onshore, where access to the turbine is easy, to offshore leads to difficulties regarding maintenance. The offshore conditions are harsher and follow a seasonal cycle, whereas onshore conditions follow a diurnal cycle. Maintenance of wind turbines needs to be done during the low-wind season. An unforeseen event causing a wind turbine to halt generation may be catastrophic economically. Hence, this leads the offshore wind industry to rely heavily on weather forecasts, on-site analysis and sensor equipment.

Chapter 3

Site Description and Available Data

The data used in this thesis is gathered from the OBLEX-F1 measurement campaign and routinely measurements at FINO1, SCADA data at the Alpha Ventus 4 wind turbine from RAVE and reanalyses data from NORA3. In this Section a short introduction is given about the available data and sites, before the data is further described in chapter 4.

3.1 FINO1

Part of the data in this thesis is retrieved from the German research station FINO1 (Forschungsplattformen in Nord- und Ostsee) located 45 km north of the german island Borkum, shown in figure 3.1. The research station is equipped with comprehensive measurement equipment and is built upon a jacket construction, placed at a water depth of approximately 30 m [65]. The platform can be seen in n figure 3.2.
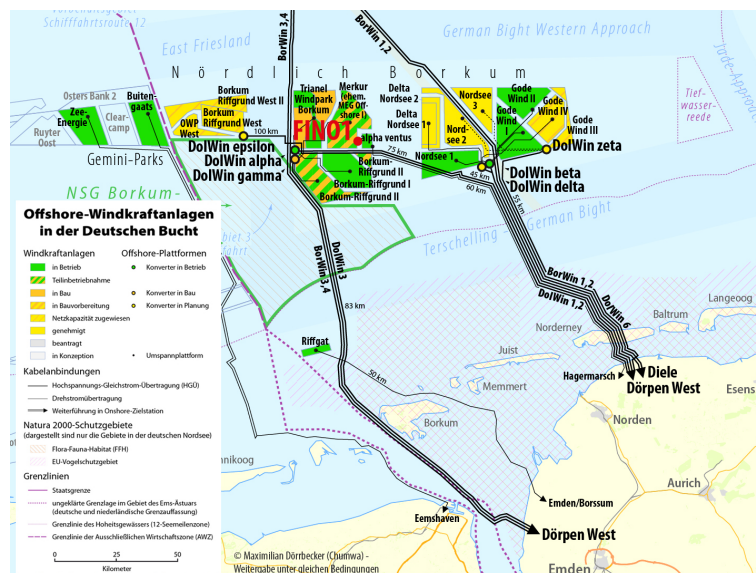
Figure 3.1: The FINO1 research station is located in close proximity to wind parks in the German North Sea.©Forschungs- und Entwicklungszentrum Fachhochschule Kiel GmbH.

FINO1 was constructed to investigate environmental conditions which might be crucial for utilizing the wind energy present in the German sector of the North Sea [65].

Figure 3.2: The FINO1 platform's main function is to secure operations with maximum degree of availability. ©Forschungs- und Entwicklungszentrum Fachhochschule Kiel GmbH.

High-frequency sonic anemometer data is gathered from routinely measurements from 01.08.15 to 31.08.15. The routinely measurements observe meteorology data at heights 40, 60 and 80 m. High-frequency sonic anemometer data is also gathered from the OBLEX-F1 campaign, coinciding with the same period, for heights 15 and 20 m. The high-frequency measurements are gathered at 25 Hz on heights 15 and 20 m, 20 Hz at 40 and 80 m, and 10 Hz at 60 m. The oceanographic data is captured from a sea buoy near FINO1 (200 m away), capturing wave height, period, and direction. The buoy is of the type Datawell Directional Waverider MKIII with a sampling rate of 3.84 Hz.

The meteorology data is recorded at a met-mast mounted on the platform, stretching roughly 103 meters above sea level (ASL), as shown in figure 3.3. Different sensors are mounted to the met-mast, recording wind speed, wind direction, air pressure, humidity and air- and sea temperature at different heights. Table 3.1 summarizes the measure heights of the sonic anemometers and cup anemometers installed at FINO1, while Table 3.2 summarizes the sampling frequency and orientation.

Height [m]	Cup Anemometer	Sonic Anemometer	Measurement Campaign
15		X	OBLEX-F1
20		X	OBLEX-F1
33	X		Routinely measurement
40	X	X	Routinely measurement
50	X		Routinely measurement
60	X	X	Routinely measurement
70	X		Routinely measurement
80	X	X	Routinely measurement
90	X		Routinely measurement
100	X		Routinely measurement

Table 3.1: Table showing available anemometers at FINO1 at different heights, where X marks sensor. The height is given as the height ASL. The measurement campaign column indicates if the measurements are taken routinely (as part of the FINO1 project) or during other measurement campaigns.

Height [m]	Frequency	Orientation
15	25Hz	135°
20	25Hz	135°
40	20Hz	308°
60	10Hz	308°
80	20Hz	308°

Table 3.2: Sampling frequency of the Sonic anemometer, where heights is given as the height ASL.
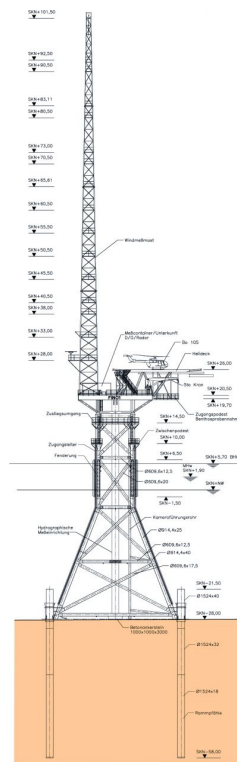
Figure 3.3: The platform is a jacket construction, placed at a depth of 30 m. ©Forschungs- und Entwicklungszentrum Fachhochschule Kiel GmbH [66].

This thesis used sonic anemometer data from heights of 15, 20, 40, 60 and 80 meters and cup anemometer data from 33 and 90 meters. The different heights were chosen in the analysis to quantify if the vertical transport of horizontal momentum is visible from sea level to the hub level. If this interaction is visible at the height of 80 meters, we can look at how it affect the estimated power extraction. In addition, the heights are used to look at wind veer and the wind shear exponent.

3.2   Alpha Ventus - RAVE

Rave is a research initiative by the Federal Government of Germany [67], further advancing the German offshore wind energy industry and knowledge. To date, it is funded by the Federal Ministry for Economic Affairs and Energy and coordinated by the Fraunhofer Institute for Wind Energy Systems. Rave was initiated as an offshore test field with four primary goals:

1. Proving the offshore suitability of 5 MW turbines

2. Further develop system technology

3. Investigate open question about offshore wind energy use

4. Expand the wind energy potential in Germany

Further, these goals have been updated to reduce offshore wind energy cost and reduce the technical risk associated with offshore wind. In 2010 the offshore wind farm Alpha Ventus was commissioned and the Rave measuring systems were put into operation. The wind farm Alpha Ventus consists of 12 turbines at 5 MW, half of them produced by Senvion and the other half by Adwen. The layout of the Alpha Ventus wind park is shown in figure 3.4.
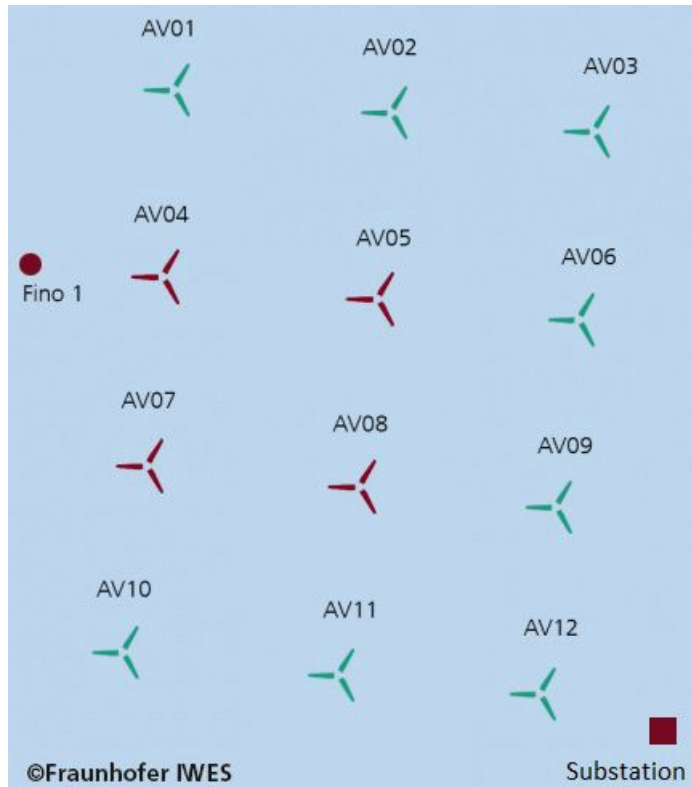
Figure 3.4: The Rave research initiative, Alpha Ventus wind park, is located in close proximity to FINO1 [68].
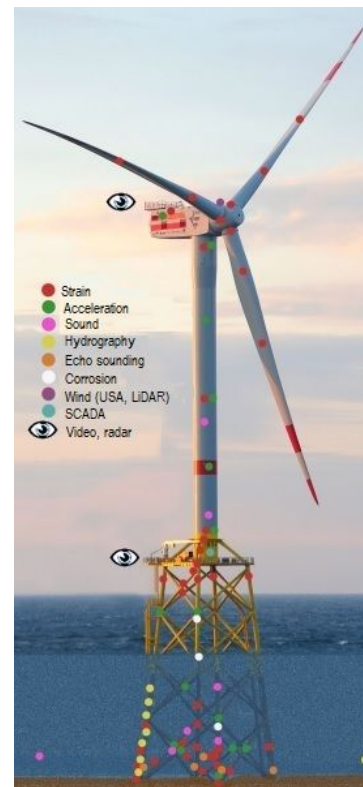
Figure 3.5: Different types of sensors are mounted on AV4, a Senvion wind turbine [68].

Wind turbine data is collected from the Alpha Ventus wind park, located east of FINO1. Of the turbines in the Alpha Ventus wind park, the one closest to FINO1 is Alpha Ventus 4, AV4 (405 m east of FINO1).The location of the AV4 is shown in Table 3.3. The turbine is of the type Senvion 5M, horizontally-axed with three blades, with a rated power of 5 MW [68]. The measurements from the turbine are collected and supervised by GL Garrad Hassan Deutschland GmbH. The turbine is divided into four measurement segments: the rotor, the tower, the nacelle and the support structure, depicted in figure 3.5. The sensors in the nacelle and the rotor blades comprise three acceleration sensors, 16 strain gauges, 12 temperature humidity pressure sensors, 12 fiberoptic sensors, and 6 SCADA signals. SCADA data from the Senvion wind turbine is retrieved as 10-min average values [68]. The wind speed restrictions on AV4 is shown in Table 3.4 This thesis focuses only on the SCADA signals retrieved from the nacelle, and permission to publish the thesis using RAVE data were given 20.May 2020.

Turbine	Coordinates (East)	Coordinates (North)
Alpha Ventus 04	6° 35'37.834"E	54° 00'51.569"N

Table 3.3: Location of the Alpha Ventus 04 turbine.

Restriction	Value [m/s]
Cut-in wind speed	3.5
Rated wind speed	12.5
Cut-off wind speed	25

Table 3.4: AV4 restrictions.

3.3   NORA3

NORA3 is a Norwegian Reanalysis dataset with a 15-year mesoscale-permitting atmospheric hindcast of the North Sea, the Barents Sea, and the Norwegian Sea [69]. NORA3 have been validated to suit wind power estimates with a slightly conservative estimate of offshore wind metrics [70]. The high-resolution data set was made by the Norwegian Meteorological Institute and is an atmospheric dynamic downscaling of the ERA-5 reanalysis data set from the European Centre of Medium-Range Weather Forecasts [70]. NORA3 provides wind data at heights between 10 m and 500 m and wave data, covering a period from 1979 until 2021.

Key information about the NORA3 dataset is shown in Table 3.5, while further in-depth information is found in "NORA3: A Nonhydrostatic High-Resolution Hindcast of the North Sea, the Norwegian Sea, and the Barents Sea" [69] and "Norwegian hindcast archive (NORA3) - A validation of offshore wind resources in the North Sea and Norwegian Sea" [70].

	NORA3
Horizontal Resolution	3km
Weather prediction model	HARMONIE–AROME, Cy 40h1.2
Based on	ERA5 reanalysis
Period	1979-2021
Available heights	10, 20, 50, 100, 250, 500, 750 [m]

Table 3.5: Key information about NORA3.

Chapter 4

Data and Methods

4.1 Methodology

In this section, the key parameters from FINO1, OBLEX-F1, NORA3 and SCADA from AV4 and how the data was processed will be presented. Since this thesis consists of multiple case studies using different datasets, the key parameters for each case will be presented separately. Following a description of methods and how the data is processed. All data was processed using Python [71] and Jupiter Notebook [72], with formulas extracted from various articles mentioned in the theory part of this thesis. Figure 4.1 shows the overall methodology of how the data is processed before conducted into the analysis.
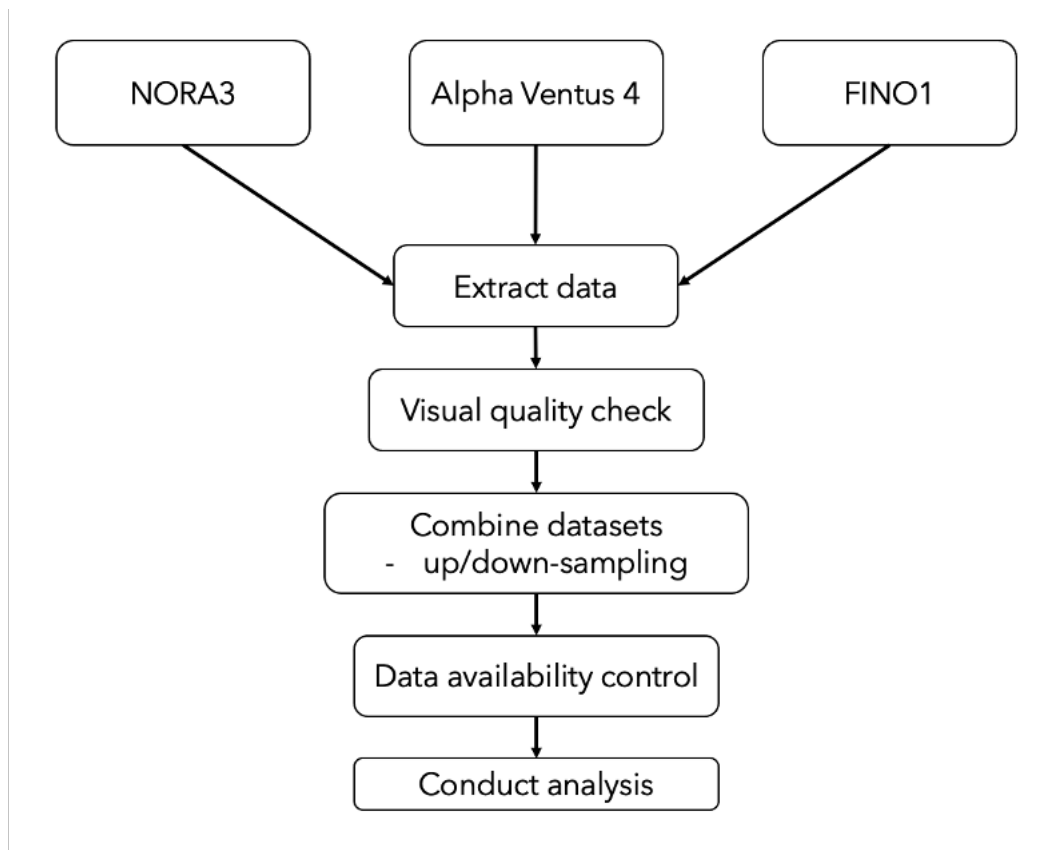
Figure 4.1: Methodology, showing how the different datasets are used and controlled.

This thesis aims to conclude a wind-wave interaction study using high-frequency wind and wave measurements to investigate how wind-wave interactions affect offshore wind power generation. This study used observational qualitative data, retrieved from FINO1, NORA3 and a Alpha Ventus wind turbine during the period stated in Table 4.1.

Case Study	Period	Datasets	Type of Data
I	01.05.2015 − 01.01.2016	FINO1 & Alpha Ventus	Cup-anemometer & SCADA
II	01.08.2015 − 31.08.2015	FINO1 & Alpha Ventus	Sonic-anemometer & SCADA
III	01.01.2015 − 31.01.2017	NORA3 & Alpha Ventus	Reanalysis data & SCADA

Table 4.1: Case study overview. Note that in Case study II the FINO1 dataset consists of OBLEX-F1 and routinely measurements.

4.2   Data Description

4.2.1   Case Study I

Wind

Wind data used in the analysis was retrieved from FINO1 cup anemometers at heights 33 m and 90 m. The data was sampled as 10-min average values. For data retrieved from these cup anemometers, wind shadow zones were not considered as a study by Kettle [73] showed no significant changes in the data when the shadow zone caused by the met-mast was included.
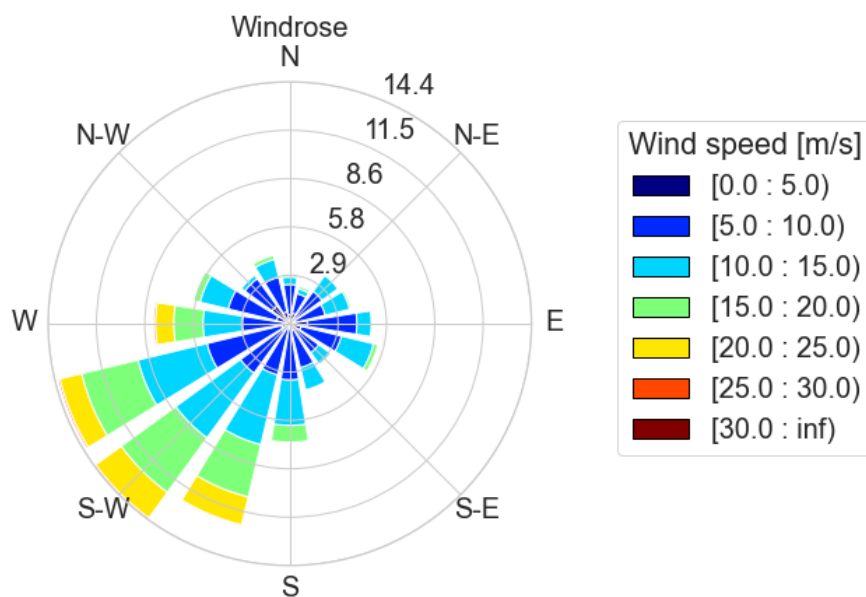
Figure 4.2: A wind rose shown at FINO1, over the time period 05.01.2015 − 31.12.2015. The wind rose shows wind speed (90 m ASL) as m/s.

Figure 4.2 show how wind directions are distributed throughout the period 05.01.2015

− 31.12.2015, where the majority of the wind comes from a south-westerly direction. The wind data used in this case study has a data availability at 100% for wind measurement at 33 m and 90 m.

Wave

The wave data was sampled as 30-minutes average data during the period 01.05.2015 − 31.12.2015. The wave data has a data availability of 85.65%, with data missing at two separate time steps. Figure 4.3 show how wave directions are distributed throughout the period 05.01.2015 − 31.12.2015, where the majority of the waves comes from an westerly direction. Table 4.2 show the highest and lowest significant wave height in the dataset.

Measurement	Value
Highest significant wave height	8.54 m
Lowest significant wave height	0.25 m

Table 4.2: Wave data at FINO1, Case study I.
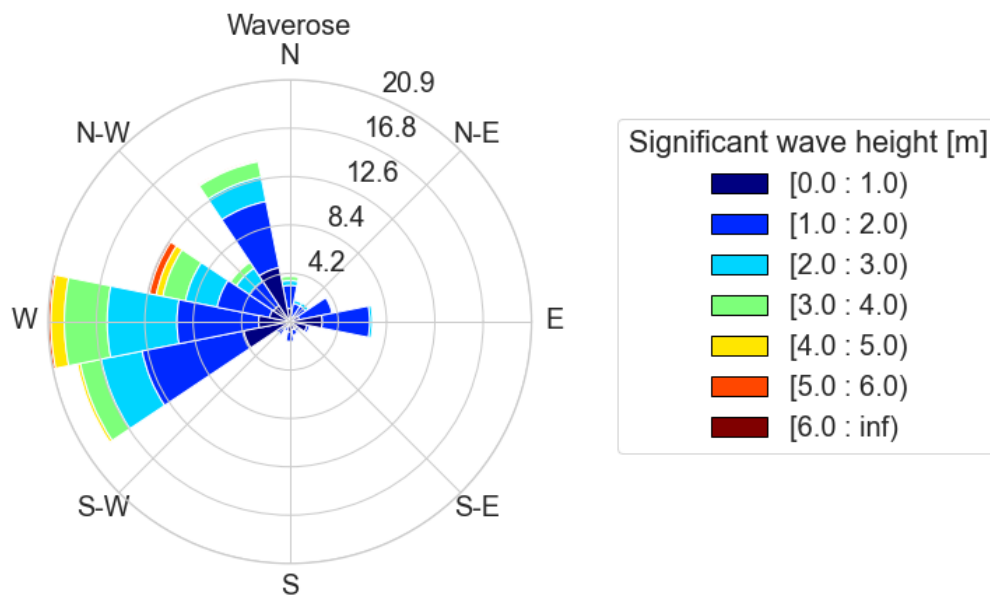
Figure 4.3: Wave rose shown at FINO1, over the time period 05.01.2015 − 31.12.2015. The wave rose show significant wave height as m.

Power

The power generation data is retrieved from SCADA-system on AV4, where active power data is normalized to values between zero and one. The mean normalized power generation value is 0.66 MW, leading to a capacity factor of 66%. The rated power of AV4 is 5 MW, equivalent to 1 when normalized. The wind turbine AV4 is located in close vicinity to FINO1, further explained in section 3.2. The SCADA data has a availability at 100%.

4.2.2   Case Study II

Wind

Wind data used is retrieved from sonic anemometers at heights 15 m, 20 m, 40 m, 60 m and 80 m. Figure 4.4 shows the distribution of wind direction and wind speed.
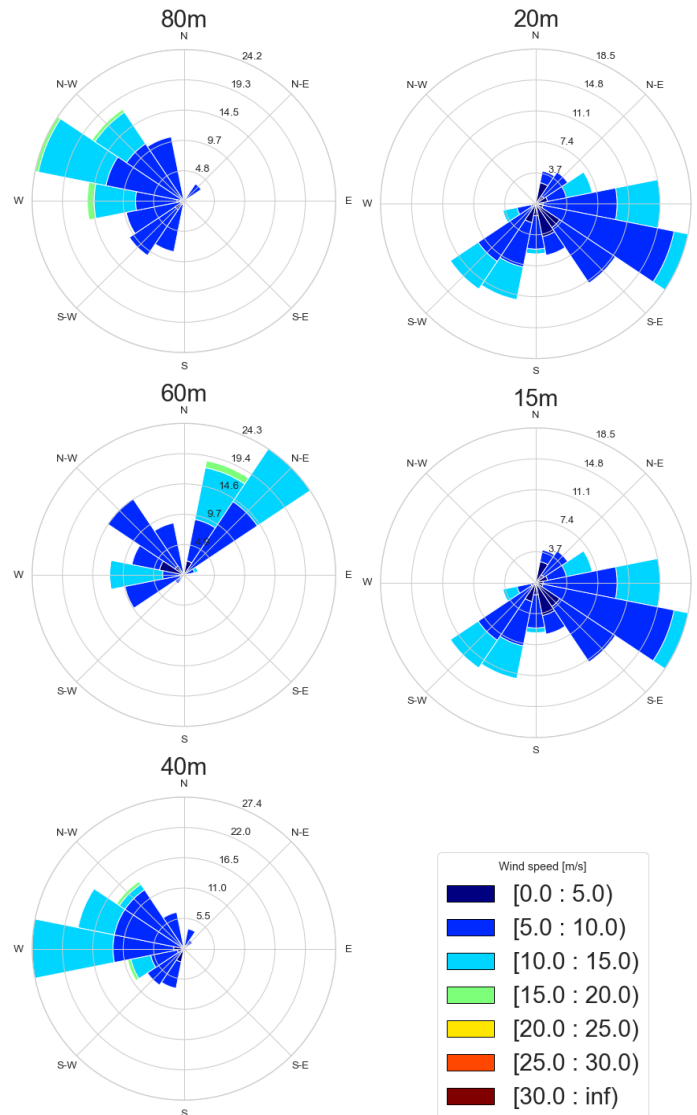
Figure 4.4: A wind rose shown at FINO1, over the time period 01.05.2015 − 31.08.2015. The wind rose shows wind speed as [m/s], for heights 15 m, 20 m, 40 m, 60 m and 80 m. Wind data from heights 15 m and 20 m is from the OBLEX-F1 campaign, while 40 m, 60 m and 80 m are routinely measurements.

The predominant wind direction for heights 15 m and 20 m is east/southeast with small contributions from southwest. For heights 40 m and 80 m the predominant direction is westerly, and for 60 m it is northeast. For sonic anemometers measurements the wind shadow zone was taken into account and wind data affected is removed from the analysis. For anemometers with an orientation at 308°, data from wind directions between 60° - 200° is removed. While for anemometers with an orientation of 135°, data from wind direction between 245° - 360° is removed [16]. The sensor orientation

and wind shadow zones can be seen in section 3.1. The data availability, before any filtering, is shown in Table 4.3.

Height [m]	Availability [%]
15	100
20	100
40	54.53
60	54.24
80	54.53

Table 4.3: Data availability of wind data set used for case study 2.

Wave

The wave data was sampled as 30-minutes averages during August 2015, and figure 4.5 shows how the wave direction and significant wave height was distributed. Table 4.4 show maximum and minimum significant wave height and total occurrence of wave age in the dataset.

Measurement	Value
Highest significant wave height	2.91 m
Lowest significant wave height	0.28 m
Wave age > 1.2	32.95%

Table 4.4: Wave data at FINO1, Case study II.
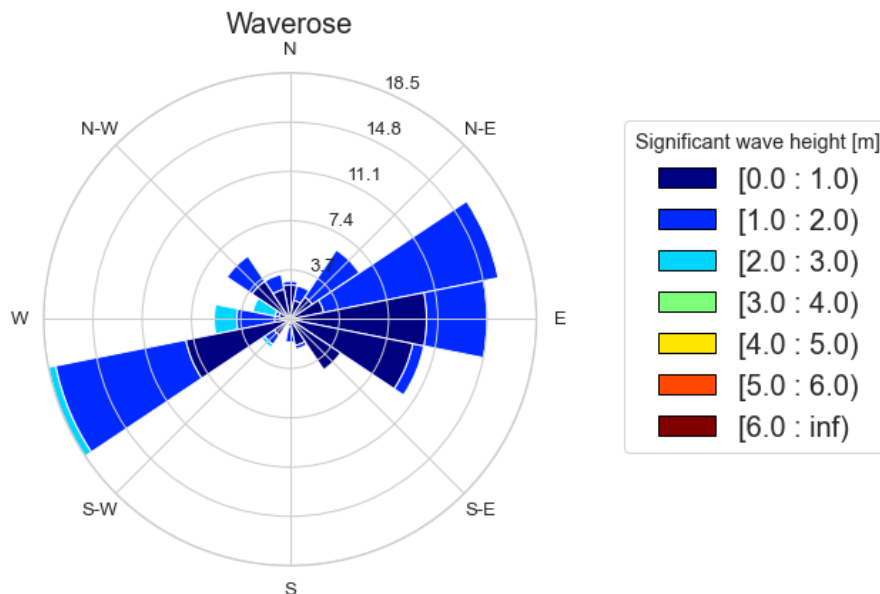
Figure 4.5: Wave rose shown at FINO1, over the time period 01.05.2015 − 31.08.2015. The wave rose show significant wave height as m.

The data availability of the wave data is 85.65%, while the predominant wave direction varies between westerly/southwesterly and east.

Power

The power generation data is retrieved from SCADA-system on AV4, where active power data is normalized to values between zero and one. The mean normalized power generation value is 0.496, leading to a capacity factor of 49.6%. The rated power of AV4 is 5 MW, equivalent to 1 when normalized. The SCADA data has a availability at 100%.

4.2.3   Case Study III

The data in Case study III is retrieved from NORA3 reanalysis dataset. As this is a reanalysis dataset, the data availability is at 100%.

Wind

The wind data is given as hourly values and stretches over the period $01.01.2015 - 01.01.2017$. Figure 4.6 shows the distribution of wind direction and wind speed, where the predominant wind direction is westerly/southwesterly for all heights.
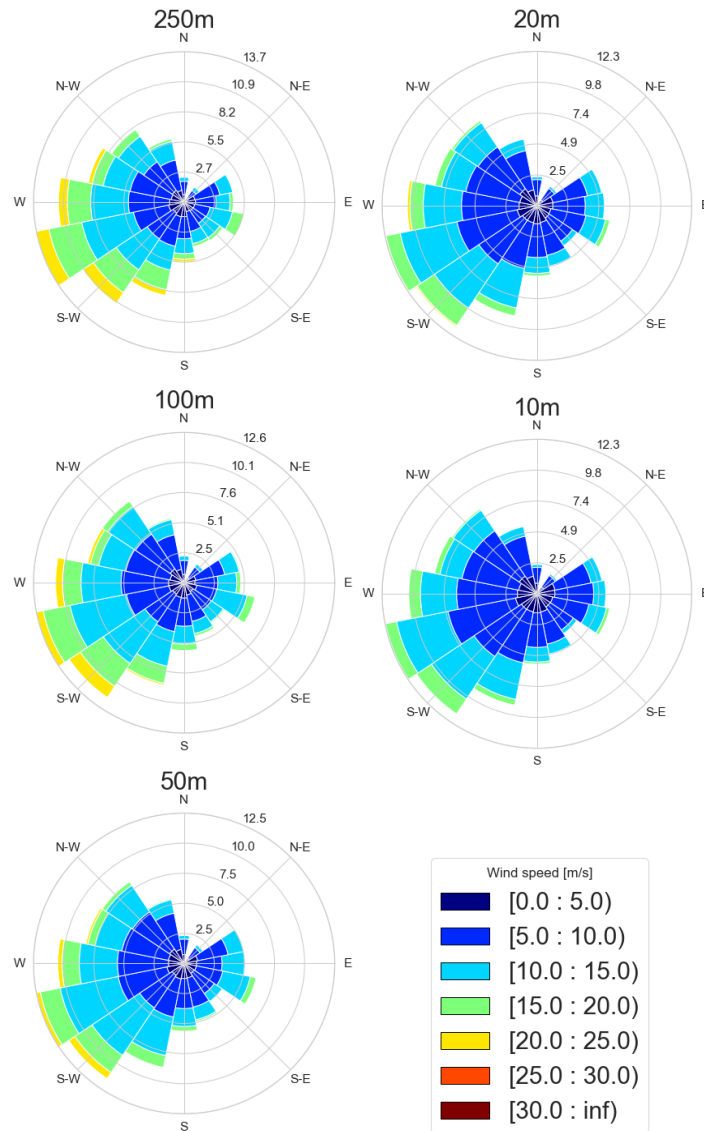
Figure 4.6: Wind rose shown at FINO1, over the time period 01.01.2015 − 01.01.2017. The wind rose show wind speed as [m/s], for heights 10 m, 20 m, 50 m, 100 m and 250 m.

Wave

The data is sampled hourly and stretches over the period 01.01.2015 − 01.01.2017. Figure 4.7 shows how wave direction and significant wave height is distributed. Table 4.5 show maximum and minimum significant wave height and total occurrence of wave age in the dataset.

Measurement	Value
Highest significant wave height	6.36 m
Lowest significant wave height	0.11 m
Wave age > 1.2	52.07%

Table 4.5: Wave data for NORA3.
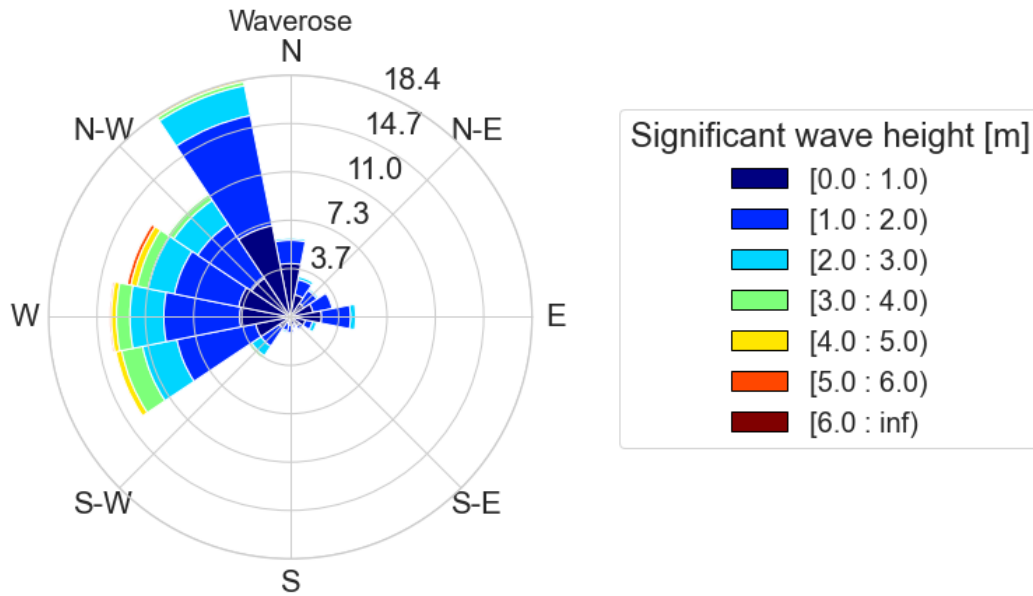
Figure 4.7: Wave rose shown at FINO1, over the time period 01.01.2015 − 01.01.2017. The wave rose show significant wave height as m.

Power

The power generation data is retrieved from SCADA-system on AV4, where active power data is normalized to values between zero and one. The mean normalized power generation value is 0.46, leading to a capacity factor of 46%. The rated power of AV4 is 5 MW, equivalent to 1 when normalized. The SCADA data has a availability at 93.7%. In Table 4.6 the mean normalized power for 2015 and 2016 is shown.

Year	Normalized power
2015	0.48
2016	0.42

Table 4.6: Overview of the mean normalized power generation at AV4.

4.3   Data Processing

4.3.1   Visual Control

To investigate and compare FINO1-data, Alpha Ventus 4, AV4, data and NORA3-data, a processing is necessary. As visualized in figure 4.8, the first step of data processing is a visual control.
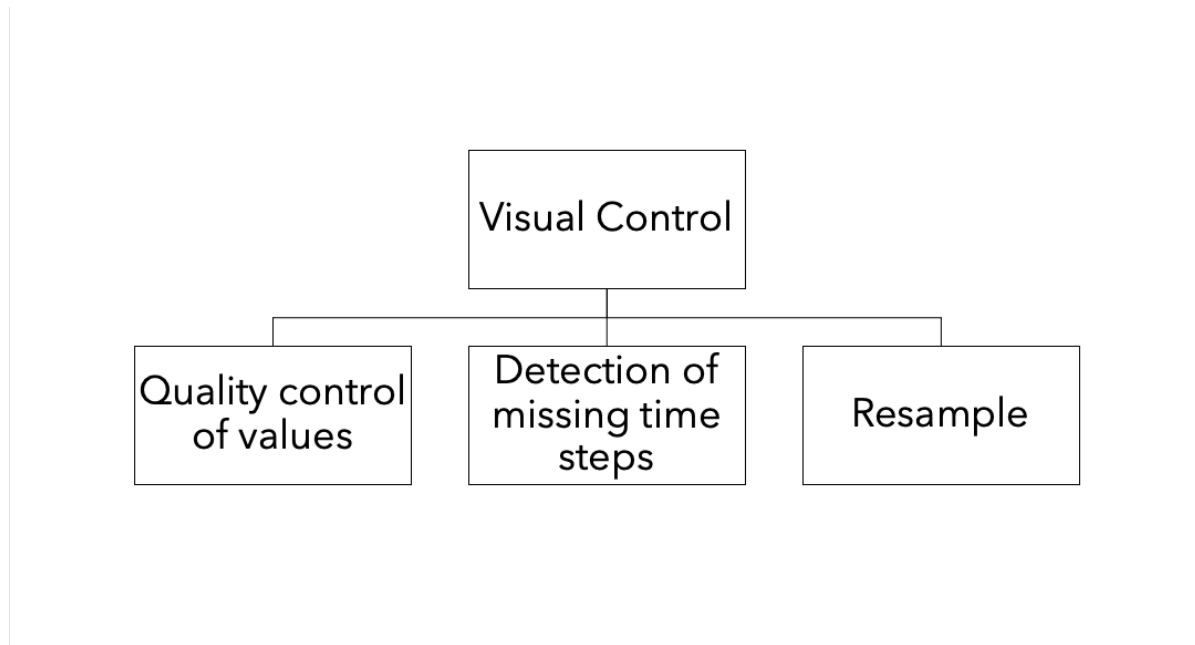
Figure 4.8: Visual control flowchart.

Quality Control

Quality control of data points was done in multiple ways. One aspect is to look for outliers, which is a datapoint which clearly deviates from the rest of the samples.

Another aspect is to remove data which exceeds given maximum and/or minimum values, e.g. power data, from AV4, where all data exceeding rated power were removed. The same goes for wind speed data where the wind direction exceeded $360°$ or when the wind speed were below cut-in speed.

Missing Time Steps

Missing time steps can be detected two ways. (1) is to plot a timeseries based on dates, (2) is to plot time in Matlab-time format which, if complete, should show a linear line.
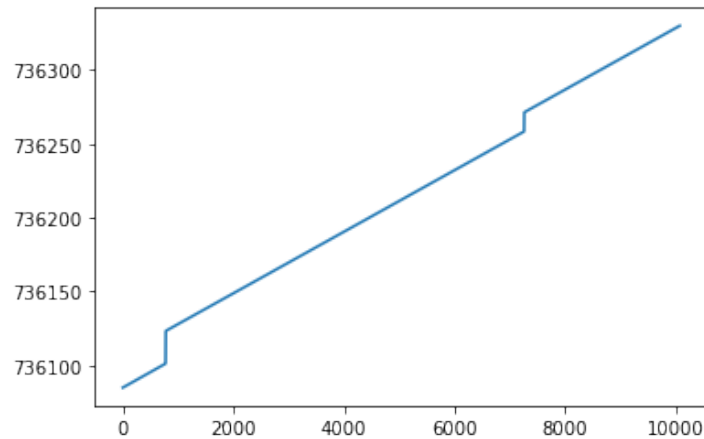
Figure 4.9: A plot with timesteps in Matlab-format showing missing time steps at two occurrences. These vertical leaps indicate areas in the data set where we have no available data. By identifying the start and stop of these leaps, we can easily remove/add these missing time steps.

Figure 4.9 shows indication of two time periods where time steps are missing. After these missing time steps were identified the missing dates were linearly interpolated, giving us a complete time series including date information. All values corresponding to the linearly interpolated dates are then set as NaN-values (Not-a-Number values).

Resampling

We are interested in comparing multiple data sets sampled with different rates and time steps, and we need to resample them all to match. In most cases, this means a resample into 10-min averages, as this is the industry standard for wind data. Then, depending on the data available and the analysis conducted, the data is resampled to fit the objective of the analysis. In this thesis, the python package pandas.DataFrame.resample is used.

4.3.2 Sampling Frequency

We use an up-sampling/down-sampling technique based on the Fast Fourier Transform to handle sensors with different sampling frequencies. Using up- or down-sampling enables different sampling frequencies in the same analysis. In this thesis, the scipy.signal.resample function, from the python scipy library [74], is used. The benefits and drawbacks of up-sampling and down-sampling have been discussed. Keeping all available data from a high-frequency measurement outweighs the drawbacks of down-sampling and removing data. In cases where anemometer data from different heights is retrieved with different sampling frequencies, this tool is used to up-sample the data to the highest sampling frequency.

4.3.3 Combine Data Sets

It is important that the different data sets match. Therefore when each data set has gone through a visual control, it can be combined for further analysis. The main steps is shown in figure 4.10.
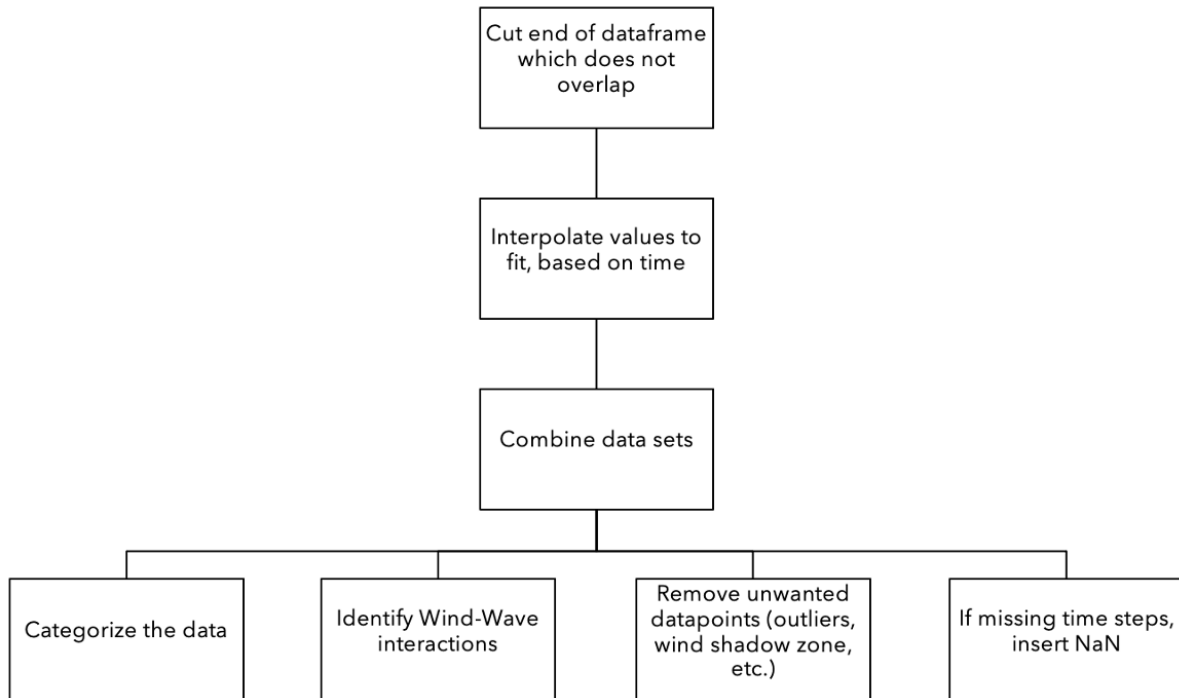
Figure 4.10: Combination of datasets flowchart, including the next steps.

4.4   Data Analysis

The data was analyzed based on what we aimed to investigate. All datasets were first analyzed to find the environmental conditions present in the respective period, as briefly shown in section 4.2. Further on, we identified wind-wave angles to look at how the different angles affected power generation and upward vertical transport of horizontal momentum. Due to higher frequency wind measurements, upward vertical transport of horizontal momentum is mainly examined in case study II. All formulas used can be found in chapter 2.

4.4.1   Normalization of Data

Confidential data is normalized to keep confidentiality, but the results are still presentable. In this thesis, the power data retrieved from AV4 is normalized to show values from 0 to 1. While at the same time, the power curves are calculated using bin averages. The data is normalized using the following equations:

$$x_{normalized} = \frac{x - x_{min}}{x_{max} - x_{min}}, \tag{4.1}$$

$$f_x = \frac{\sum y_{1(x)} + y_{2(x)} + \ldots + y_{n(x)}}{n}, \tag{4.2}$$

where x is the bin value and y is the corresponding values in that bin.

4.4.2 Momentum Transfer

Wave age has been used to indicate vertical transport of horizontal momentum upward. When events with upward transport of vertical momentum were identified, data with upward transport of vertical momentum were compared to events with downward transport of vertical momentum to see potential effect on the power generation. The comparison is made by comparing two power curves, one for each vertical momentum transfer direction.

4.4.3 Wind-Wave Angle

The effect of different wind-wave angles is investigated by simply categorising them into bins, as shown in Table 2.6; Aligned, Misaligned and Opposed. After categorising, we can compare these regimes to investigate how they affect the power generation at an offshore wind turbine.

4.4.4 Stability Conditions

For case study II, we will briefly look at the stability conditions present in the given dataset to investigate how they may affect wind power generation. The stability conditions are summarized in Section 2.5.1, which shows the formula and the boundary classes used in this study. The wind shear relies strongly on atmospheric stability [75], which again affects power generation.

4.4.5 Environmental Contour

Environmental contours are used to assess and define the extreme environmental conditions, which might be further used to evaluate the environmental loads on a structure [76], such as an offshore wind turbine. The environmental contour describes the extreme joint values of environmental variables, such as significant wave height, wave peak period and wind speed. Assessment of these extreme joint values is essential for ensuring safety during extreme environmental conditions [77]. As stated by Haselsteiner et al. [78], contour methods are acknowledged as approximate methods founded on the principles of structural reliability.

A joint distribution of the environmental variables of interest has to be created to derive an environmental contour. Based on this joint distribution, the environmental contour can be constructed. This thesis will use the Inverse First-Order Reliability, IFORM method. This method, first suggested by Winterstein et al. [79] in 1993, was introduced to reduce structural reliability problems. In this thesis, two environmental contours will be created: (1) for significant wave height (Hs) against wave peak period (Tp), and (2) for wind speed (u) against significant wave height (Hs).

The first step is to identify the distribution of the environmental parameter. Generally, the Weibull distribution is used for significant wave height and wind speed, while a log-normal distribution is used for wave peak period [78]. When the return period of

the environmental contour is longer than the measurement period, which it is for this thesis, values in the joint probability distribution must be extrapolated beyond the available data [77], causing statistically informed guessing of the fitted dependence between the environmental parameters [76]. In this thesis, Haselsteiner et al.'s Omae2020-8219 global hierarchical models, constructed for better interpreting how wind and waves behave in order to extrapolate values better [76], will be used together with the python-based software ViroCon [80].

The hierarchy of the joint density function is given as:

$$f_{X1,X2}(x_1, x_2) = f_{X1}(x_1) f_{X1|X2}(x_1|x_2), \tag{4.3}$$

where $X1$ and $X2$ represents random variables, such as wind speed (U) and significant wave height (Hs), and $f_{X1}(x_1)$ denotes the marginal distribution while $f_{X1|X2}(x_1|x_2)$ denotes the conditional distribution. In the Omae2020-8219 global hierarchical model, Hs and U follow an exponential Weibull distribution, which for the joint wind-wave distribution is conditional on the value of U,

$$F(U) = (1 - exp[-(\frac{u}{\alpha})^{\beta}])^{\gamma}, \tag{4.4}$$

$$F(Hs|U) = (1 - exp[-(\frac{Hs}{\alpha_{Hs}})^{\beta_{Hs}}])^{\gamma_{Hs}},$$

where β and γ denotes, respectively, the first and second shape parameter of the distribution, while α denotes the scale parameter.

The parameters used in either a sea-state model (Hs|Tp) or in a wind-wave model (U|Hs) is estimated by four steps. First the marginal distribution, f_{X1}, is fitted using a weighted least squares method [76]. Second, the period of $X2$ is sorted into $X1$ intervals (e.g. for $X1 = x_1$, $X2 = [x_{2(1,1)}, x_{2(1,2)}, x_{2(1,3)}, ..., x_{2(1,n)}]$). Third, the marginal distribution is fitted to the $X2$ period, in each interval, using maximum likelihood estimations. Fourth, the dependence function is fitted using nonlinear least squares.

Lastly, the contour lines are plotted based on a given exceedance probability value. The exceedance probability is given as,

$$P_e = \frac{Environmental\ state\ duration}{Return\ period\ of\ interest} = \frac{T_S}{T_R}. \tag{4.5}$$

Further in-depth explanations of how the environmental contours are calculated may be read in "ViroCon: A software to compute multivariate extremes using the environmental contour method" [80] and "Global Hierarchical Models for Wind and Wave Contours: Physical Interpretations of the Dependence Functions" [76].

4.4.6 Statistical Testing

Weibull Parameter

The Weibull distribution is used to show how the Weibull parameters relate to wind speed [81]. For wind energy assessments and analysis, the two-parameter Weibull distribution is commonly used as it has shown to capture the skewness of the wind speed distribution accurately [81, 82]. The scale- and shape parameter is commonly given as c and k, respectively.

The Weibull distribution is given by [81–84];

$$f_{(v)} = \left(\frac{k}{c}\right)\left(\frac{v}{c}\right)^{(k-1)} \exp\left[-\left(\frac{v}{c}\right)^{(k)}\right], \qquad (4.6)$$

where $f_{(v)}$ is the wind speed probability, and v is the wind speed.
There are several ways to estimate the parameters k and c, and for this thesis, the maximum likelihood estimator, MLE, was selected. The MLE assumes the probability distribution based on given observed data. The MLE approach provides good estimated results for different sample sizes, and values of c and k [83]. For the wind industry, the Weibull parameters is used to recreate time-series [85] or to extract properties such as the most frequent wind speed or maximum wind speed [83]. In this thesis, python package *scipy.stats.weibull_min* [74] has been used to estimate the Weibull parameters.

Wind Shear Exponent

The wind shear coefficient plays a vital role in wind analysis, where it is used to estimate wind speed at higher altitudes. Often for wind analysis, concerning wind turbines, we have wind speed at a different height than hub height. Therefore, to estimate the wind speed at another height we use the power law, presented in subsection 2.1.4.

$$\alpha = \frac{\ln \frac{u(z)}{u(z_{ref})}}{\ln \frac{z}{z_{ref}}}. \qquad (4.7)$$

Increasing wind turbine sizes lead to larger blades and a larger swept area. As these blades stretch in height, and as wind speed typically increases by height, the wind shear exponent is of great interest to wind turbine producers, wind park developers, and the operation of wind turbines. For wind turbine producers, wind shear is essential due to load calculations, while for wind operators, wind shear is also essential for power generation. Investigations of how wind shear affects power generation found that for medium and high shear coefficients, the generated power was lower than expected for the corresponding wind speed at hub height [19].

Wave Age

To calculate wave age, the wind speed at 10 m (U_{10}) must be known. For datasets where U_{10} is not given, the logarithmic wind profile shown in subsection 2.1.4, is used.

For case study I, the wave age is not calculated as using the logarithmic wind profile to estimate the wind speed at 10 m from 33 m is not deemed sensible.

Comparison of Power Curves

To verify the differences between the power curves, shown in Chapter 5, statistically, the deviation to the actual power curve is calculated in percent. The actual power curve is calculated using raw data without filtering based on wind-wave interaction conditions. The deviation percentage is then calculated by comparing the actual power curve to the filtered power curve (e.g. actual power curve against misaligned wind-wave power curve). Note that the power curves are only compared over the length of the filtered power curve. Hence, if the filtered power curve yield no values at wind speed equal to 25 m/s, that particular wind speed interval is excluded from the comparison. In addition, as the actual power curve is a function of all wind-wave interaction conditions, the percentage mainly describes positive or negative contributions for low deviations.

Chapter 5

Results

Wave data is assumed to be equal at FINO1 and Alpha Ventus 4, AV4, due to the ocean's inertia and the close distance between FINO1 and AV4. As mentioned by Kinder et al. [86], the wind park influences the turbulence and wind condition in cases where the wind speed is coming from easterly directions. In cases where FINO1 experiences wake conditions from Alpha Ventus, we can expect an increase in turbulence intensity and lower wind speed. In Case studies I, II and III, we primarily have wind speed from westerly directions, meaning that the Alpha Ventus wind park has a low influence on the results.

5.1 Case Study I

Case study I investigates wind-wave conditions surrounding FINO1 and AV4, covering one year of observation data from FINO1. The objective of Case study I is to look at environmental conditions, indications of upward transfer of horizontal momentum and wind-wave alignments during the period $05.01.2015 - 31.12.2015$.

5.1.1 Environmental Conditions

Figure 5.1 shows the time series of wave height, wave age, wind-wave alignment and wind speed at FINO1 and normalized active power at AV4 (3.2). In events of missing data segments, either removed by filters or not available, these are visible as blank segments/gaps in the figures. Note that wind speeds below 3.5 m/s are filtered away due to restrictions linked to cut-in wind speed at AV4. The time series provides a visual expression of the variability of the wind speed and how it affects power generation. The time series are categorized into aligned-, misaligned-and opposed wind-wave cases, which is used as a tool to understand the importance of different wind-wave alignments for the offshore wind industry.

Figure 5.2 shows the highest density of wind speed occurrences at 33 m and 90 m, where the highest density occurs between cut-in and rated wind speed. Approximately 60% of the wind speed occurs within this wind speed interval in this dataset.
Figure 5.3 shows how the wind shear exponent is distributed throughout the period $01.05.2015 - 01.01.2016$. Further on, figure 5.5 shows how wind direction changes
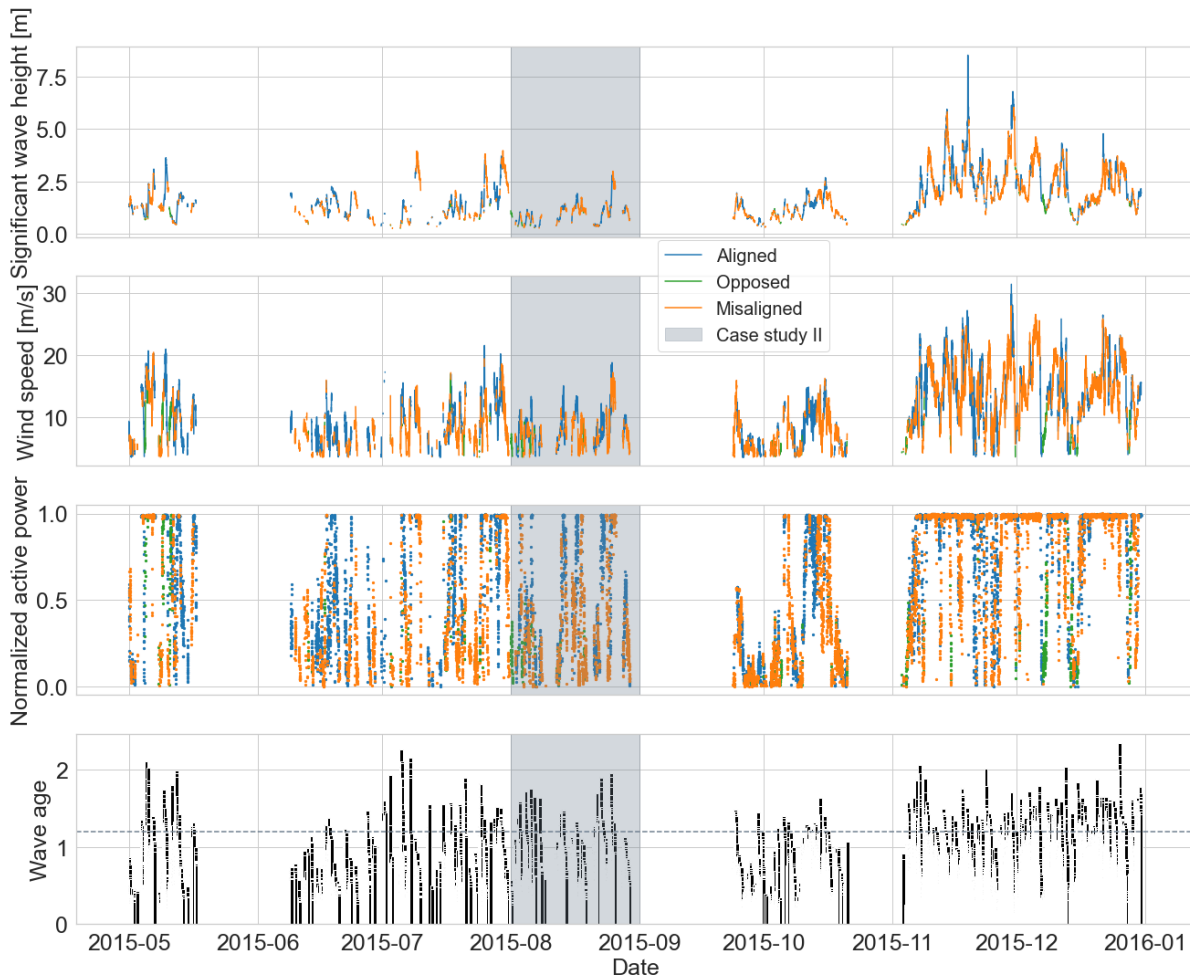
Figure 5.1: Time series of wind speed (90 m ASL) and significant wave height at FINO1, normalized power at AV4, and wave age. The time series shows how the different wind-wave alignments are distributed throughout the period and compares them to the wave age. The grey area indicates the period of case study II. The measurement is taken during the period 05.01.2015 − 31.12.2015. Wave age is calculated using the logarithmic wind scale to transform wind speed from 33 m to 10 m, assuming neutral conditions, no stratification and that the surface roughness length is equal to 0.0061.
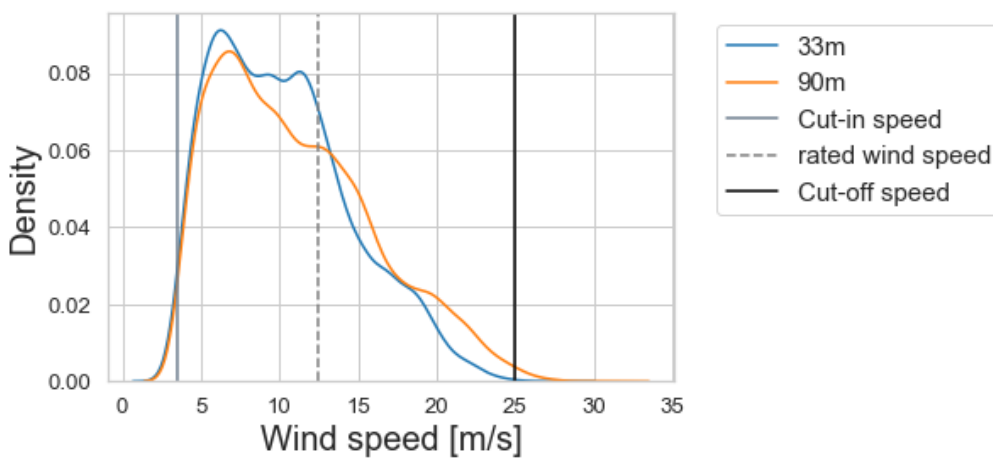
Figure 5.2: Probability density distribution for wind speed at heights 33 and 90 m.
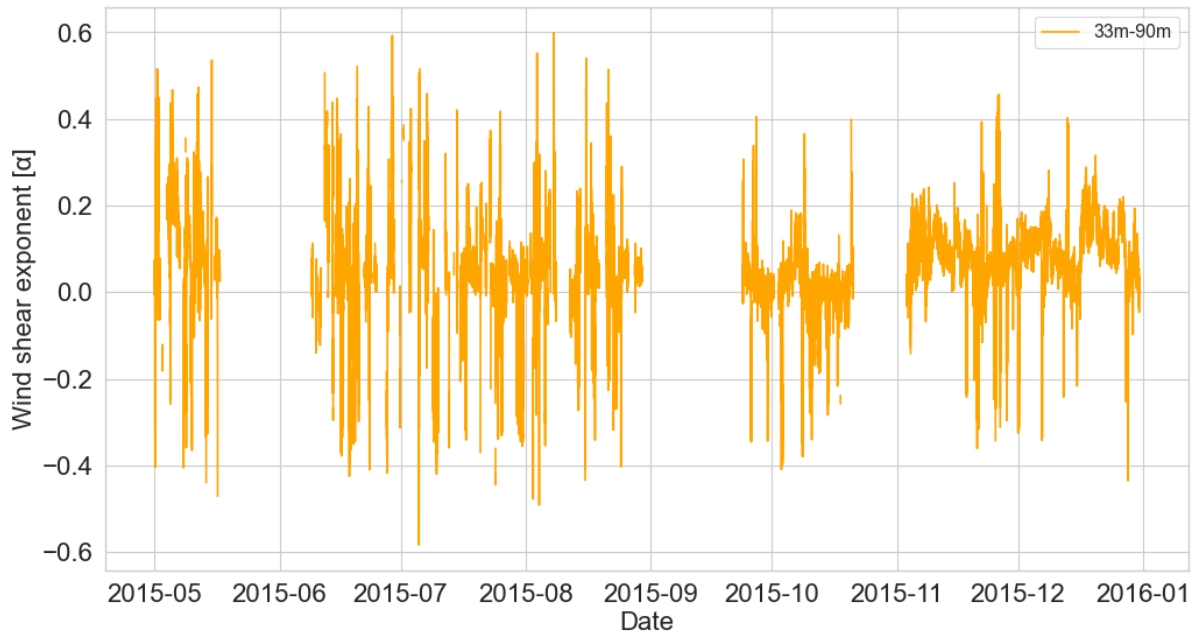
Figure 5.3: Wind shear exponent.

depending on height during the period $05.01.2015 - 31.12.2015$. The wind rose indicates that, for misaligned cases, most of the wind is coming from a more southerly direction than in aligned cases. This behaviour is present in both the wind rose at 90 m and 33 m. Figure 5.4 shows how the wind shear exponents affects the power curve, where lower wind shear values seem to fit the actual power curve best.
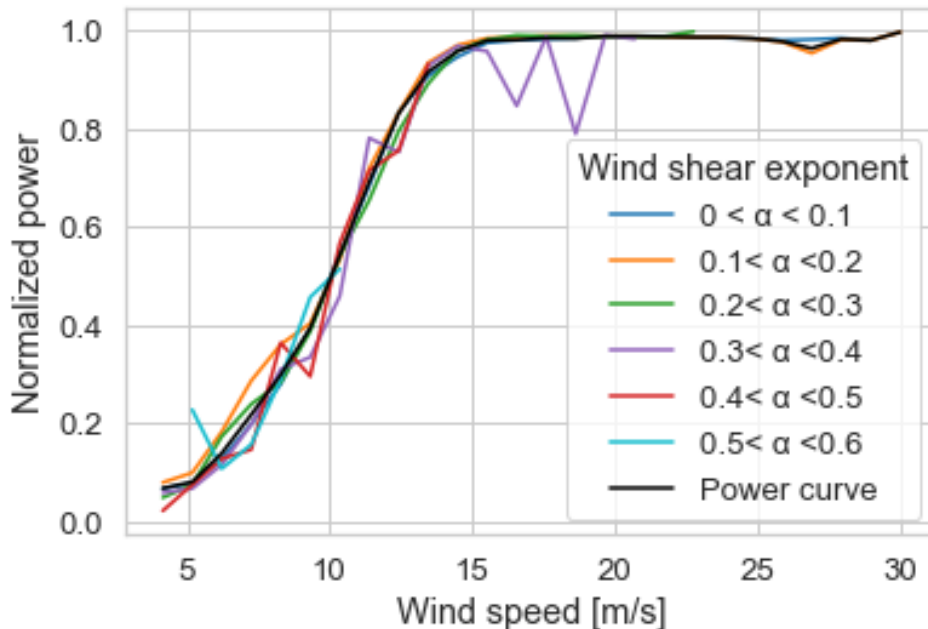
Figure 5.4: Power curve showing based on wind shear values.

In figure 5.6 the Weibull shape (k) and scale (c) parameters are shown, with indications of how the variables changes depending on wind speed. Figure 5.6 (a) show the
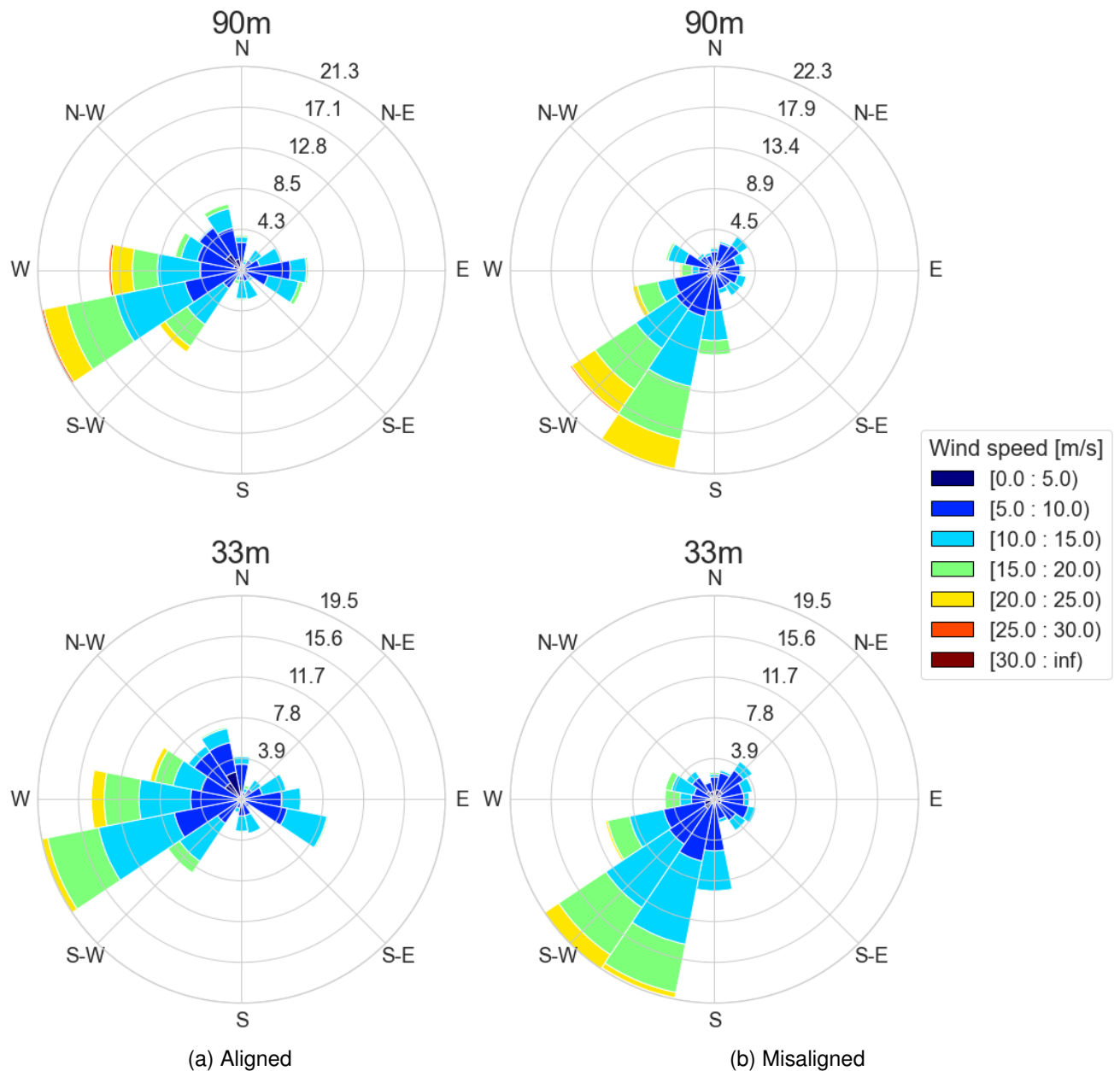
Figure 5.5: Wind rose showing wind veer at FINO1 for aligned and misaligned wind waves, at heights 33 m (ASL) and 90 m (ASL). The Wind rose shows wind speed as [m/s] during the period 05.01.2015 − 31.12.2015.

aligned shape parameter, (b) the aligned scale parameter, (c) the misaligned shape parameter and (d) the misaligned scale parameter. The results show, both for aligned- and misaligned wind-waves, that the shape parameters for both heights follows each other well. Indicating a similar distribution on both heights throughout the sample period.
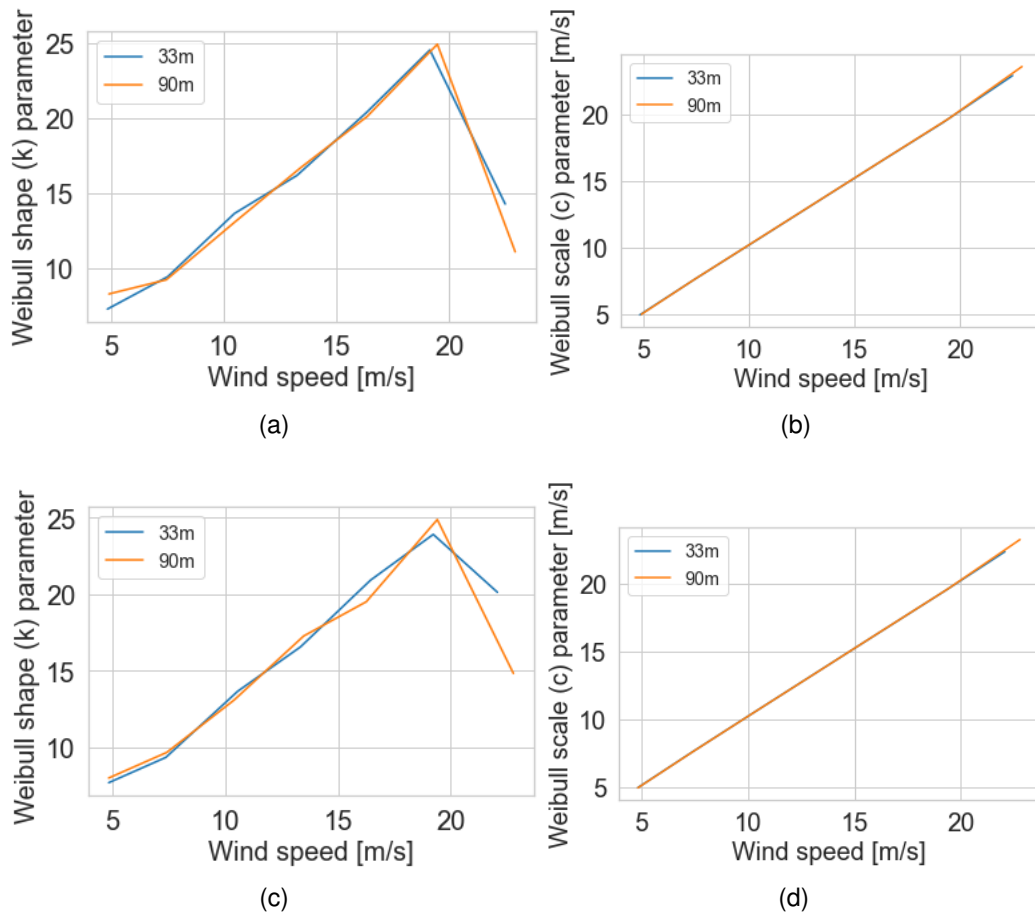
Figure 5.6: ***Weibull parameter plotted against wind speed.*** *The figures show how the Weibull parameters change from aligned to misaligned wind waves: (a) the aligned shape parameter; (b) the aligned scale parameter; (c) the misaligned shape parameter, and (d) the misaligned scale parameter. The data is calculated using 5 m/s bins, [0, CoW) (CoW = cut-off wind speed).*

5.1.2   Upward Transfer of Horizontal Momentum
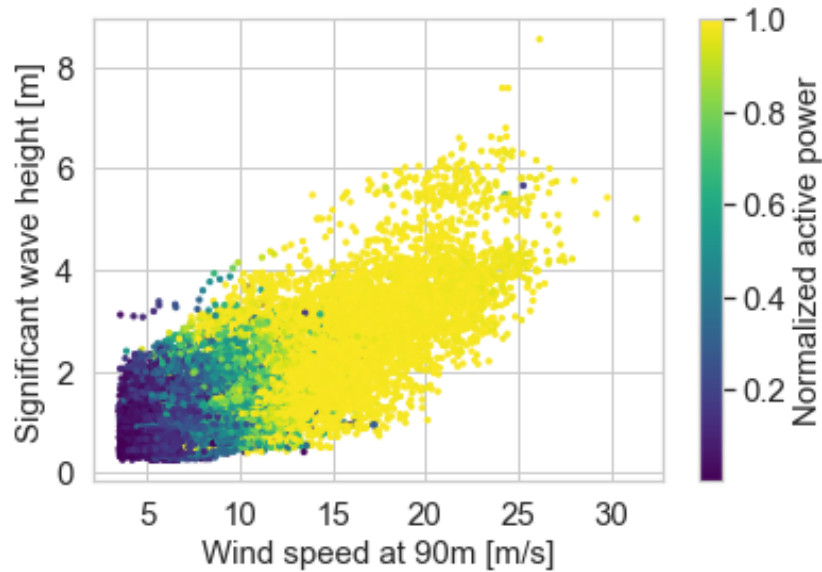
Figure 5.7: Significant wave height plotted against wind speed (90 m ASL), with a color bar showing normalized power generation.

Wind speed and significant wave height are strongly correlated, where the correlation coefficient is 0.75. Figure 5.7 shows that stronger winds lead to higher waves. In the area of around 10 m/s the generated power varies depending on the wind speed and the significant wave height, imploring that wind speed and wave height affect power generation. The graph shows predicted tendencies for strong- (higher waves, higher power generation) and weak winds (lower waves, lower power generation).
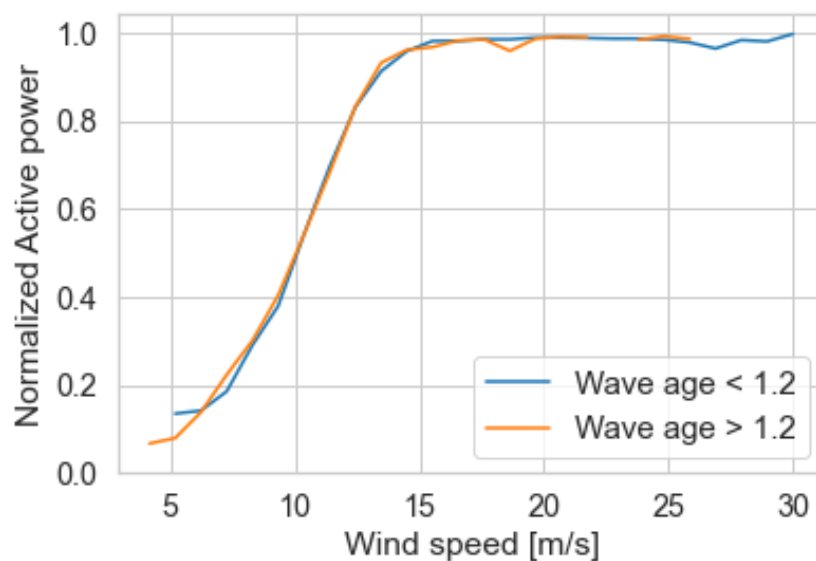
Figure 5.8: Power curves plotted for wave age ratio above and below 1.2. The wind speed used to calculate wave age (U_{10} is calculated using the logarithmic wind profile with $Z_0 = 0.0061$).

Figure 5.8 shows how the power curve deviates depending on the wave age ratio. The wave age is calculated using the logarithmic wind profile with a surface roughness value, Z_0, of 0.0061, where the initial wind speed was observed at 33 m. The power curves show only small differences between the different wave age ratio values.

5.1.3   Wind-Wave Alignment

During Case study I, the wind-wave alignments spread out as shown in Table 5.1. Misalignment between waves and wind accounts for almost 49% of all analyzed events, indicating that misalignment is commonly occurring—only 6.36% of the analyzed cases experienced opposed wind waves.

Wind-Wave Alignments	Occurrence [%]
Aligned	44.93
Misaligned	48.71
Opposed	6.36

Table 5.1: Wind-wave alignment distributed in percent over the time period 05.01.2015 − 31.12.2015.
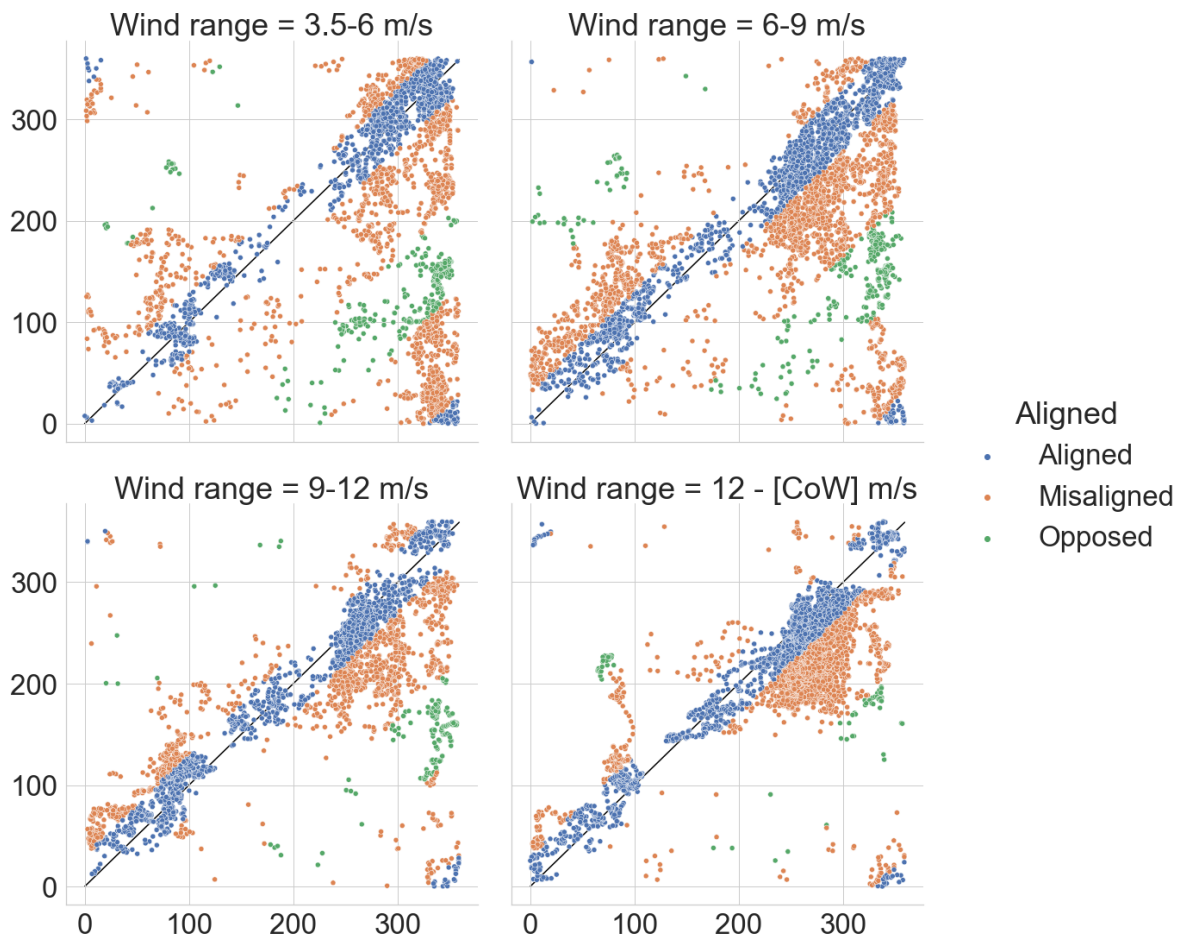
Figure 5.9: The figure shows the visualization of wind-wave alignments and their dependence on wind speed. The X-axis shows wave direction, and Y-axis shows wind direction, while the different plots are separated into different wind ranges. CoW = Cut-off wind speed.

Figure 5.9 shows how dependent the wind-wave alignment is on wind speed. Higher wind speed leads to more aligned wind-wave, while low wind speed indicates more spread wind-wave alignments. In case study II, we do a more in-depth analysis to identify different wave conditions and classify the presence of swell waves and different wind-wave regimes.

In figure 5.10 the different wind-wave angles are plotted as kernel density estimates, further showing how wind speed affects the angle between wind and waves. The figure clearly shows that higher degrees of misalignment between wind and waves occurs more frequently during lower wind speeds.
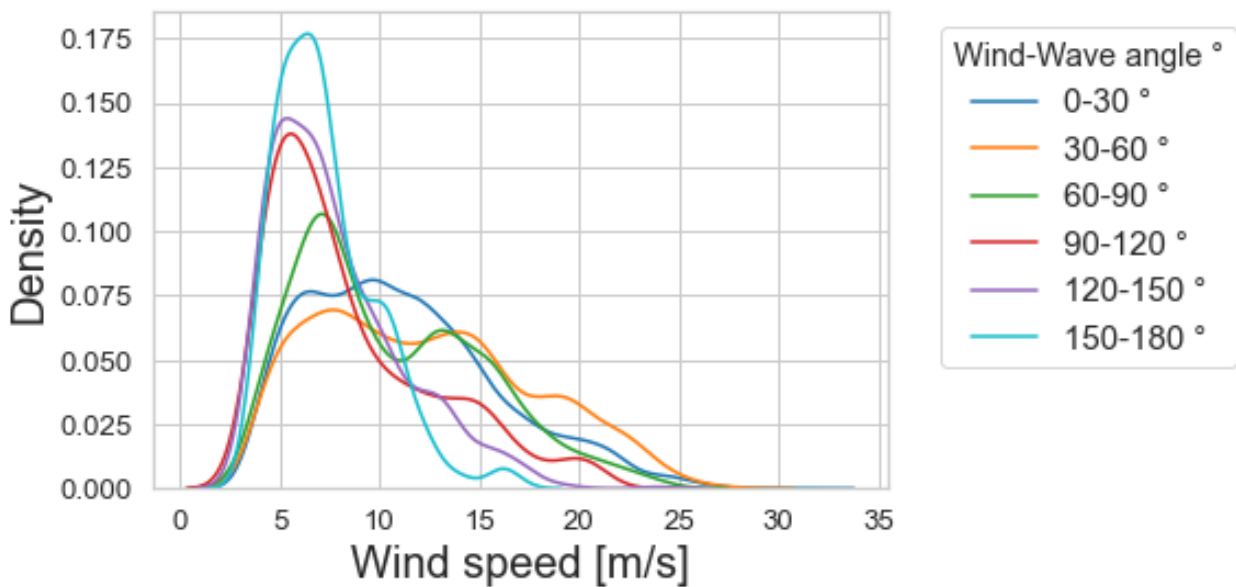
Figure 5.10: Kernel density estimates (KDE) of wind speed (90 m ASL) for different wind-wave angles, where the wind-wave angles are defined as the angle between wind direction and wave direction.

Figure 5.11 shows power curves calculated using bin averages over the wind speed, where each bin equals 1 m/s. Power data are retrieved from the AV4 wind turbine, showing how different wind-wave alignments affect the generated power. Figure 5.11 shows that the difference between the wind-wave alignment curves for low wind speeds clearly shows how the angle between the waves and the wind affects power generation. In cases where we have opposed wind waves, we can expect lower power generation than aligned wind waves. The differences between aligned-, misaligned- and opposed wind waves seem to lessen for higher wind speeds.

By comparing the different power curves in figure 5.11 to the actual power curve, we visually see that the normalized misaligned power curve fits best with the actual power curve. The normalized aligned power curve was found to over-perform by 1.16%, while the misaligned and opposed under-perform by 0.86% and 3.19%, respectively. Note that the opposed wind wave curve has a more significant under-performance due to no events of power generation occurred hat higher wind speeds during opposed wind wave conditions. Indicating, as expected, that aligned wind and waves influence power generation positively as more energy can potentially be generated at lower wind speeds

than opposed- and misaligned wind waves. Conversely, misaligned- and opposed wind waves negatively influence power generation. In addition, by comparison of the aligned power curve and the misaligned power curve we see a deviation of 2.05%, and for the aligned power curve against the opposed the deviation is 5.7%.

Further on, figure 5.11 shows the probability density distribution for wind speed overlaid by the normalized power curve. In the wind speed interval between 5 m/s and 10 m/s, the figure shows that the area where the wind-wave alignment power curves deviate overlaps with the area with a high probability of wind speeds—indicating that the power curve deviations may have a significant impact on the total power generation.
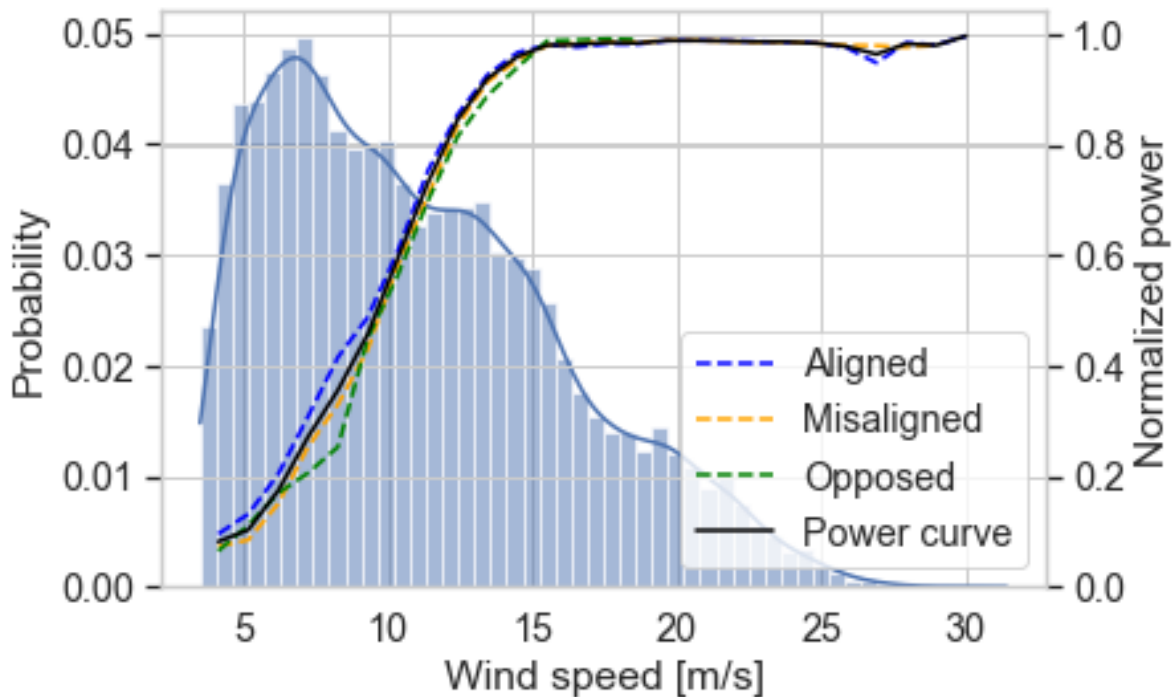
Figure 5.11: Power curve calculated using bin averages, where each bin equals 1 m/s. The wind speed is retrieved from FINO1 at 90 m, and the power data is retrieved from AV4. A power curve is plotted for each wind-wave alignment condition, showing how wind-wave alignment affects power generation during the period 05.01.2015 − 31.12.2015. The wind speed probability is overlayed on the power curves.

Wind-Wave Alignments	May	June	July	August	September	October	November	December
Aligned	54.0	58.67	51.56	47.4	48.36	39.67	50.08	36.62
Misaligned	38.3	38.74	43.08	47.25	50.72	55.44	47.49	56.65
Opposed	7.7	2.59	5.36	5.34	0.92	4.88	2.43	6.73

Table 5.2: wind-wave alignment distributed in percent per month during the time period 05.01.2015 − 31.12.2015.

In Table 5.2, the results indicate an even distribution of aligned- and misaligned wind waves. The most considerable differences between aligned- and misaligned wind

waves occur in May, June and July (where aligned wind waves occur most frequently) and October and December (where misaligned wind waves occur most frequently).
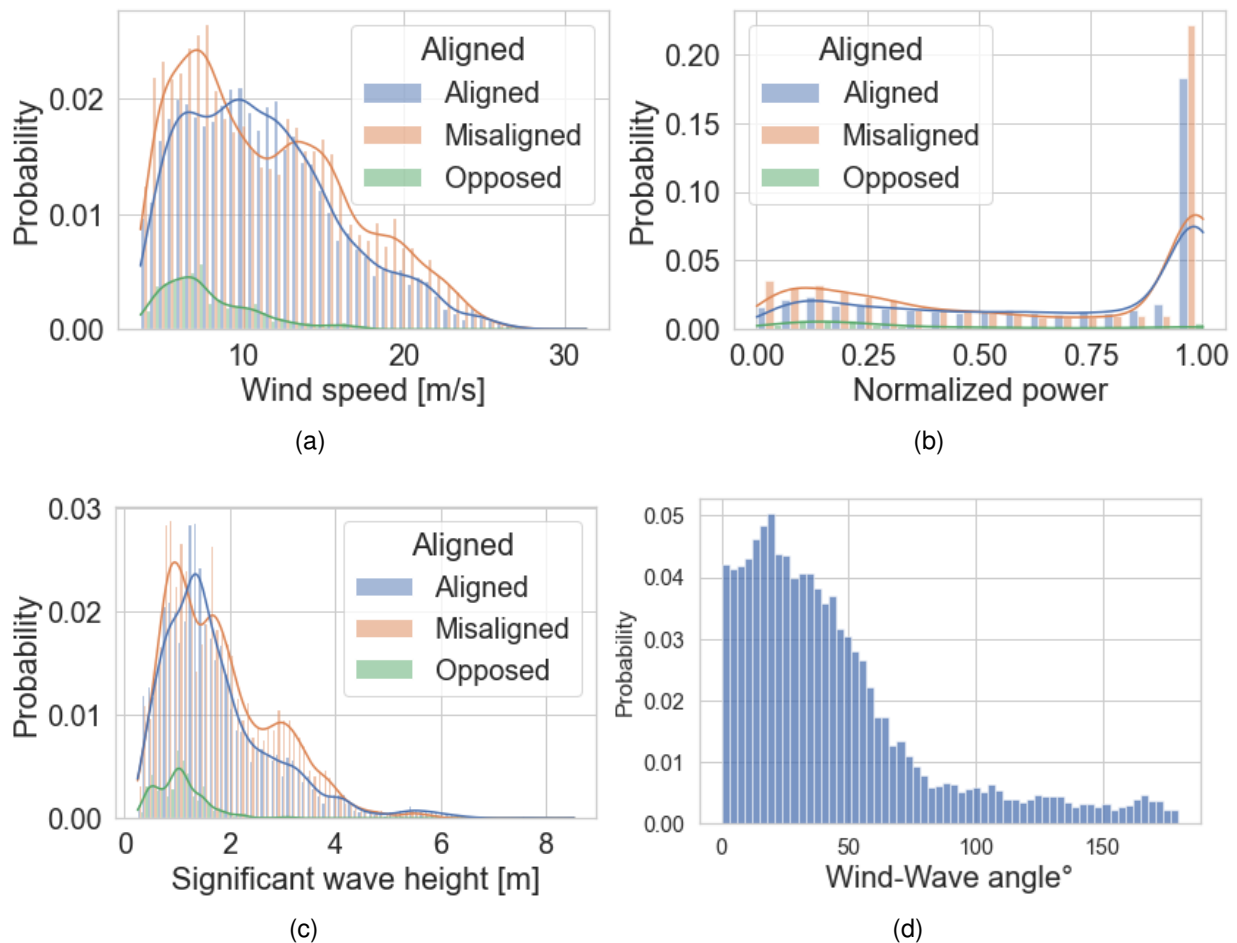
Figure 5.12: **Probability density distributions (PDF) at FINO1.** *The figures show the probability density distributions with overlaying Kernel density estimate of (a) wind speed at 90 m, (b) normalized power generation, (c) significant wave height and (d) the angle between the wind and wave directions at 90 m.*

Figure 5.12 (b) shows the distribution of normalized generated power, where power generation at rated power is most common. Further on, the shows that opposed conditions occur more frequently during lower power generation and wind speeds. However, by comparing how often the wind turbine generates power below rated power to when it generates at rated power, we would see that the power generation is mostly below rated power. Which in this case corresponds to 32% of the energy generated. Together with Table 5.1 indications are that wind and waves will be more aligned during higher wind speeds. Interestingly it also shows a near-equilibrium between misaligned conditions and aligned conditions, throughout the distribution.

Figures 5.12 (a) and 5.12 (c) show how wind-wave alignments distribute wind speed and significant wave height, where aligned- and misaligned wind-wave events are evenly distributed. Figure 5.12 (d) shows the highest probability for lower wind-wave angles, which fits in line with the distributions of figures 5.12 (a), 5.12 (b) and

5.12 (c).
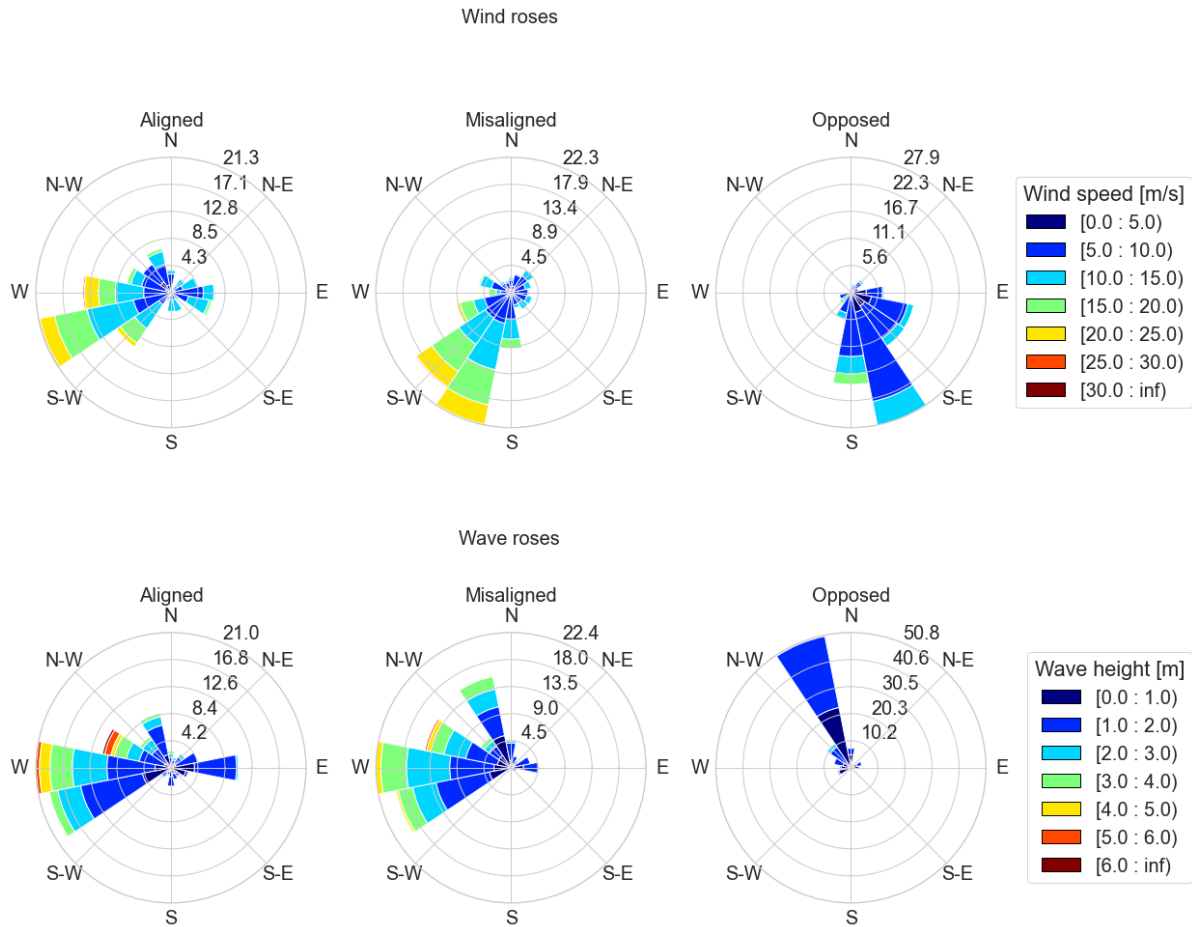
Figure 5.13: Wind- and wave roses showing the direction of wind and waves during different wind-wave alignment conditions, for the period 05.01.2015 − 31.12.2015. The wind rose shows wind speed as [m/s] at 90 m, while the wave rose shows significant wave height as [m]. Wind shadow zones are excluded. The numbers present in the plot show normalized data as a percentage.

The wind- and wave roses in 5.13 show how wind direction and wave directions distribute throughout the period 05.01.2015 − 31.12.2015. The wind rose separates wind speed using bins of 5 m/s, while the wave rose separates the significant wave height using bins of 1 m/s. The wind direction and wave direction are shown as the direction it is coming from. For aligned wind waves, the predominant direction is westerly/slightly south-westerly, with occasional easterly winds. For misaligned wind waves, the predominant direction is south-westerly for wind and westerly for waves, where we encounter occasional waves from a north-westerly direction. As a result, we encounter the most substantial wind speeds and significant wave heights during aligned- and misaligned wind waves.

Furthermore, for opposed wind waves, the predominant direction is south/south-easterly for wind and north/north-westerly for waves, causing the wind to blow from land through the Alpha Ventus wind park. The length and colour of each direction segment represent wind/wave strength, while the grey circles show normalized data as

percentages. The results presented in figure 5.13 are in line with the results shown by Porchetta et al. [16]. The wind rose indicates that aligned- and misaligned wind waves occur more often during higher wind speeds than opposed wind waves.

5.2 Case Study II

An analysis of the conditions surrounding FINO1 and Alpha Ventus wind park is done over the period $01.08.2015 - 31.08.2015$. This case study aims to look at the environmental conditions and do a more in-depth analysis of indications of upward transfer of horizontal momentum and wind-wave alignments.

5.2.1 Environmental Conditions

*Figure 5.14: **Wind-wave alignment and stability:** For the upper three plots, wind-wave alignments are shown. The top plot shows significant wave height, followed by wind speed at 15 m and 80 m. The last two plot shows atmospheric stability at the height of 80 m and wave age.*

Figure 5.14 shows, from top to bottom, the time series of significant wave height, wind speed at 15 m, wind speed at 80 m, normalized power generation at AV4 and the wave age ratio. The top three plots show wind-wave alignments, while the normalized

power plot shows stability conditions. As mentioned in Section 2.5, different atmospheric stability conditions affect the atmosphere, the stratification in the atmosphere and the wind field in different ways. As can be seen from figure 5.14 the amount of data available is ultimately much lower than for Case studies I and III. Due to low raw data availability (54%) and removal of data where the wind speed is below cut-in speed, i.e., the power generated is equal to zero, as well as the removal of wind shadow zones, the data availability is lower than desired. Missing data segments, either removed by filters or unavailable, are visible as blank segments/gaps. The time series shows the variations in wave height, wind speed and power generation, where typical patterns are visible. E.g., power generation seems to be higher during stable and neutral stability than unstable, and an increase in wind speed leads to an increase in wave height.
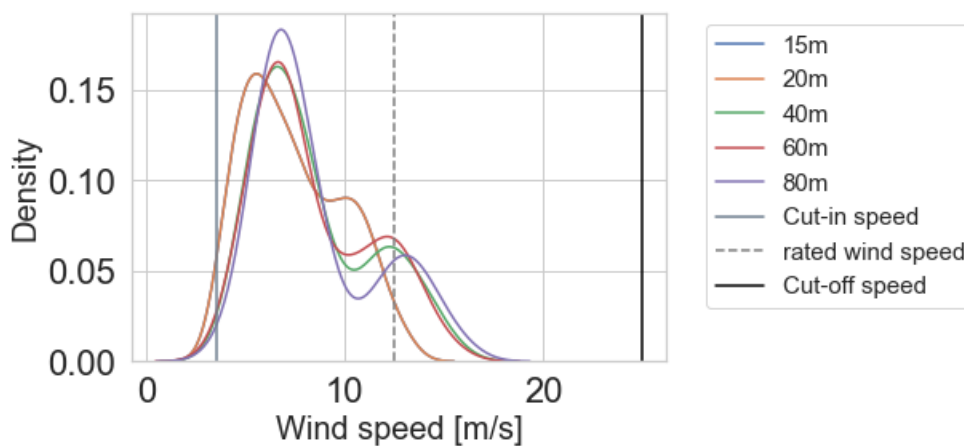
Figure 5.15: Probability density distribution for wind speed at all heights.

Wind speed varies by height, where we expect to find the highest wind speeds at higher elevations. Figure 5.15 shows that the highest elevations have their peaks at a higher wind speed compared to lower elevations. The probability density plot shows that most wind speeds in this dataset are between cut-in and rated wind speed. Between 85.7% - 96.8% of the wind speeds in this dataset is between this wind speed interval.

Figure 5.16 show shear exponents calculated between heights $15 - 20$ m, $15 - 40$ m, $15 - 60$ m and $15 - 80$ m. The shear exponents show large variation throughout the sample period, indicating that the shear exponent is affected by interactions within the MABL.

Figure 5.17 and 5.18 shows how the Weibull parameters shape (k) and scale (c) varies as the wind speed or significant wave height increases. Figure 5.18 also show how the parameters depends on wind-wave alignment. In figure 5.17 the Weibull parameters are shown based on each measurement heights, where (a) shows the aligned shape parameter, (b) the aligned scale parameter, (c) the misaligned shape parameter and (d) shows the misaligned scale parameter. The shape parameter (k) describes the wind (wave) behavior, where a small shape parameter value corresponds to a weak wind speed(significant wave height). Henceforth, a high shape parameter value indicated the presence of both high and low wind speed values (significant wave height). On the other hand, the scale parameter (c) scales the wind speed (significant wave height).
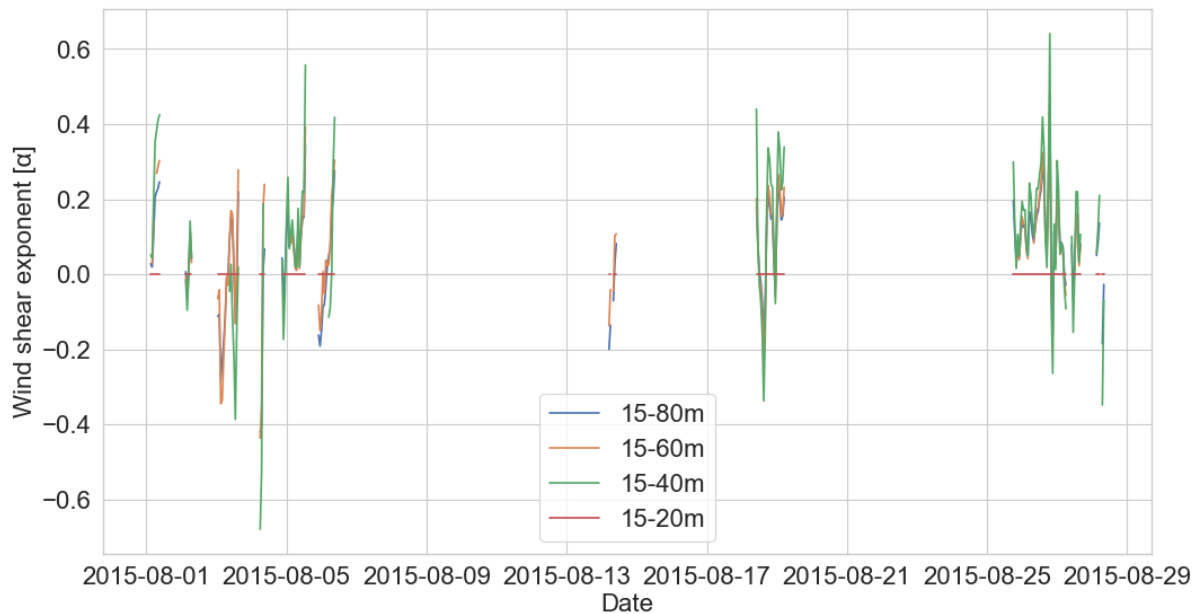
Figure 5.16: Wind shear exponents for heights 20, 40, 60 and 80 m.

The wind roses in figure 5.19 shows the distribution of wind speed direction for aligned- and misaligned wind waves at heights 15 m, 40 m, 60 m and 80 m. The wind rose separates wind speed using bins of 5 m/s, and the wind direction shown is the direction the wind is blowing from, e.g. the predominant wind direction, at the height of 40 m, in the aligned wind roses shows that wind is blowing from the west. As the figures show, the predominant wind direction changes by height. For aligned wind waves, the dominant wind direction at heights 40 m and 80 m is westerly, while for 15 m and 60 m is easterly. For misaligned wind waves, the predominant direction is northwesterly with occasional easterly winds, at 40 m and 80 m. While the predominant wind direction at heights 15 m and 60 m is southeasterly and northeasterly, respectively. Elevation, wind direction and wind-wave alignment affect the magnitude of wind speed. The wind coming from an easterly direction tends to have a lower wind speed than the wind from a westerly. The wind roses also indicate more stable and more substantial wind speeds for higher altitudes. The wind rose shows that the predominant wind direction for substantial wind speeds (above 10 m/s) is coming from the west for aligned wind waves. For misaligned wind waves, the predominant wind direction during substantial wind speeds (above 10 m/s) is northwesterly.
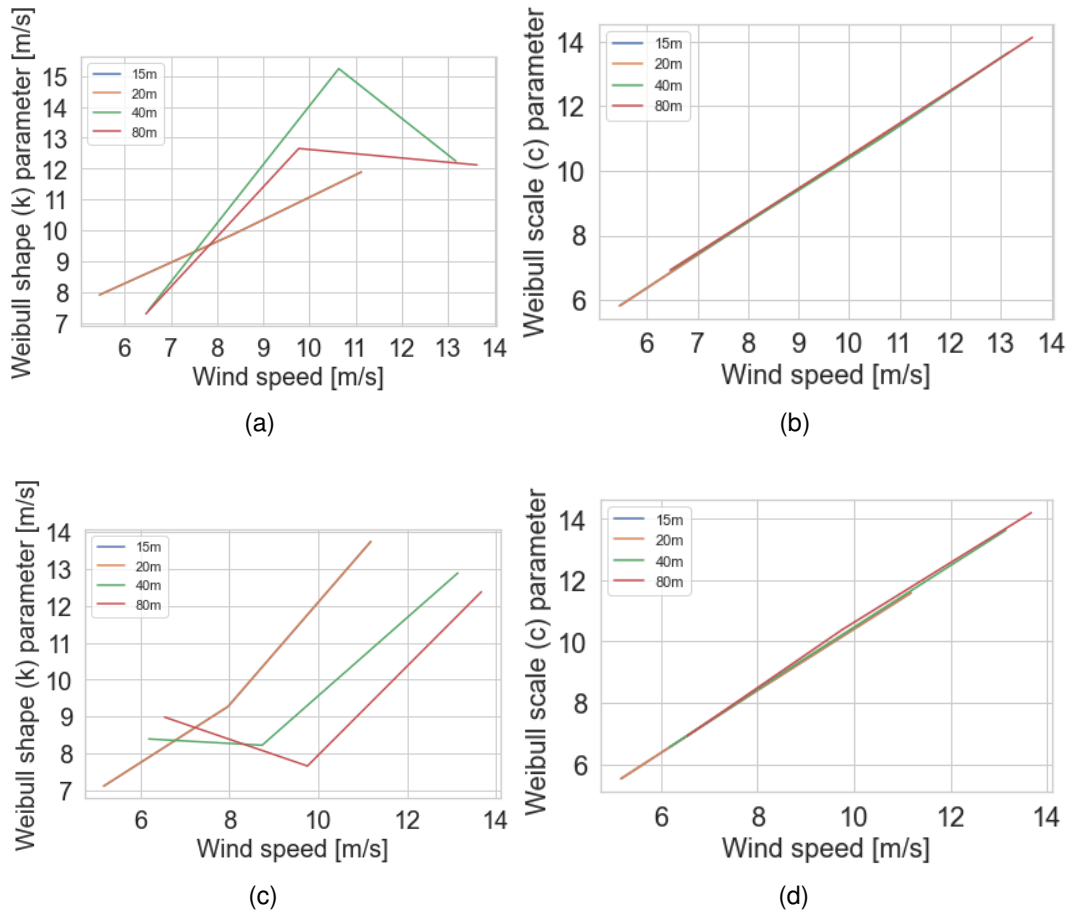
Figure 5.17: **Weibull parameter plotted against wind speed.** *The figures show how the Weibull parameters change from aligned to misaligned wind waves: (a) the aligned shape parameter; (b) the aligned scale parameter; (c) the misaligned shape parameter and (d) shows the misaligned scale parameter. The data is calculated using 5 m/s bins, [0, CoW) (CoW = cut-off wind speed).*
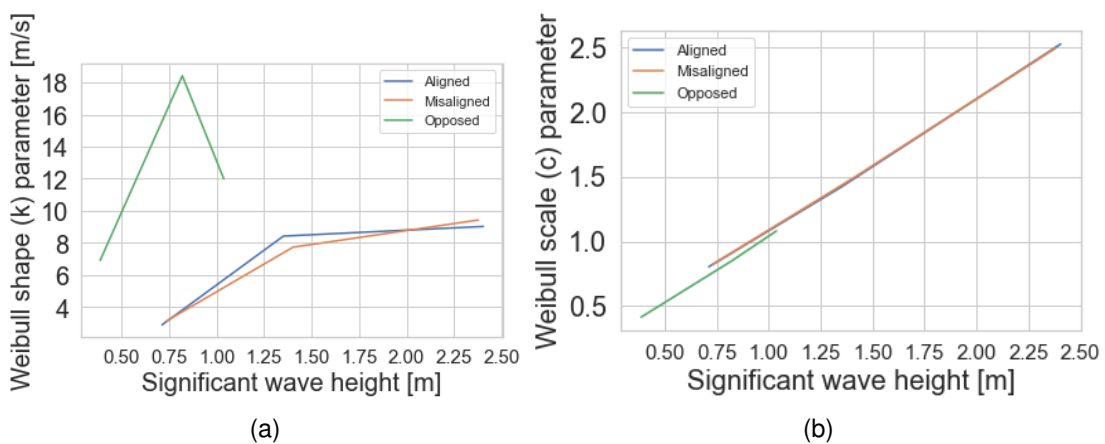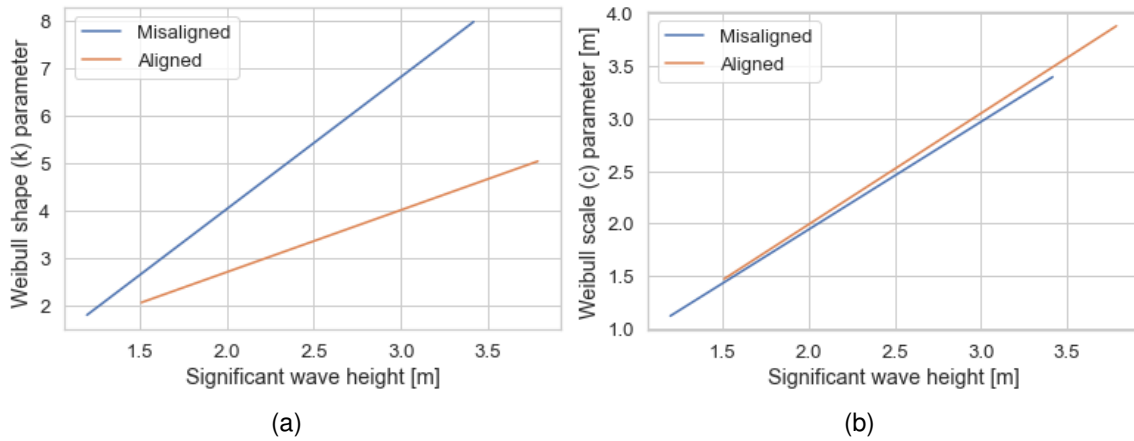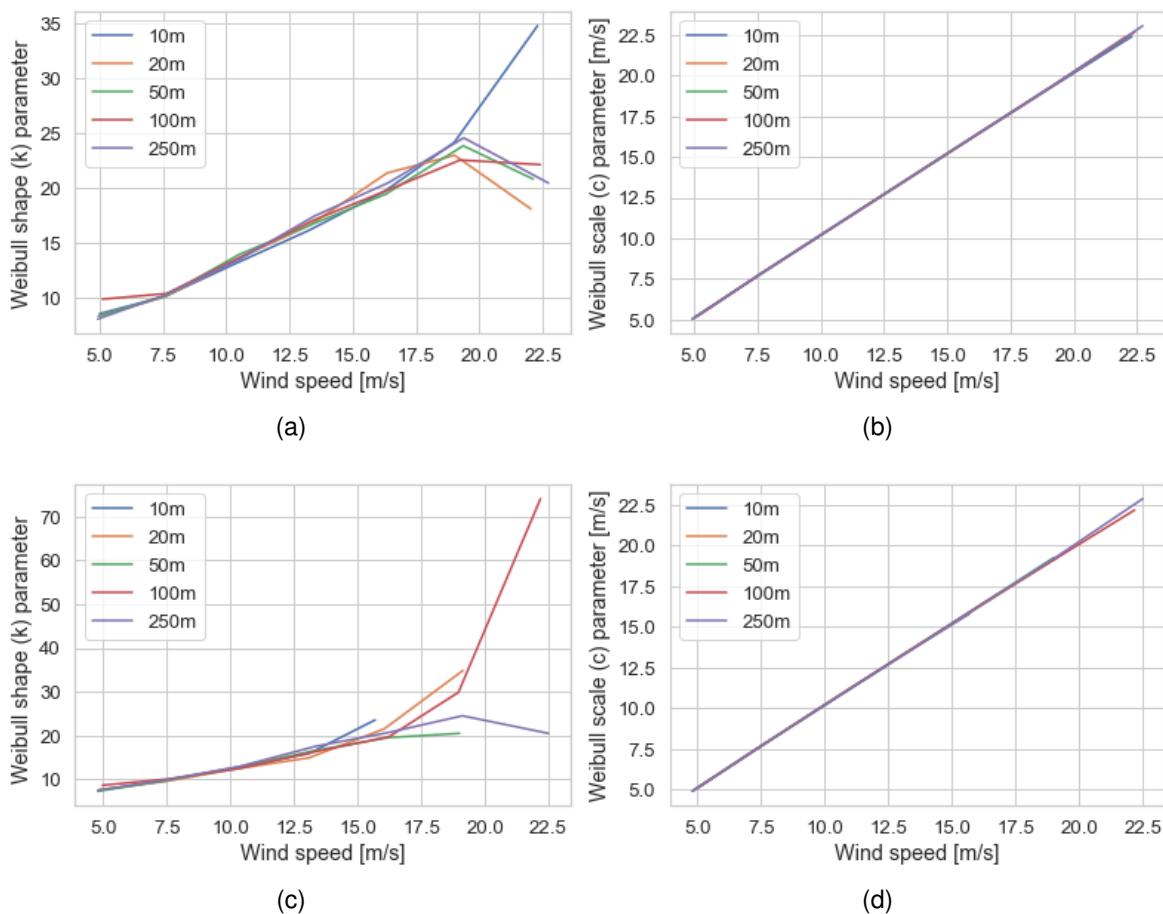

Figure 5.18: **Weibull parameter plotted against Significant wave height** *The figures show how the Weibull parameters change from aligned to misaligned wind waves: (a) the aligned shape parameter; (b) the aligned scale parameter; (c) the misaligned shape parameter and (d) shows the misaligned scale parameter. The data is calculated using 5 m/s bins, [0, CoW) (CoW = cut-off wind speed).*
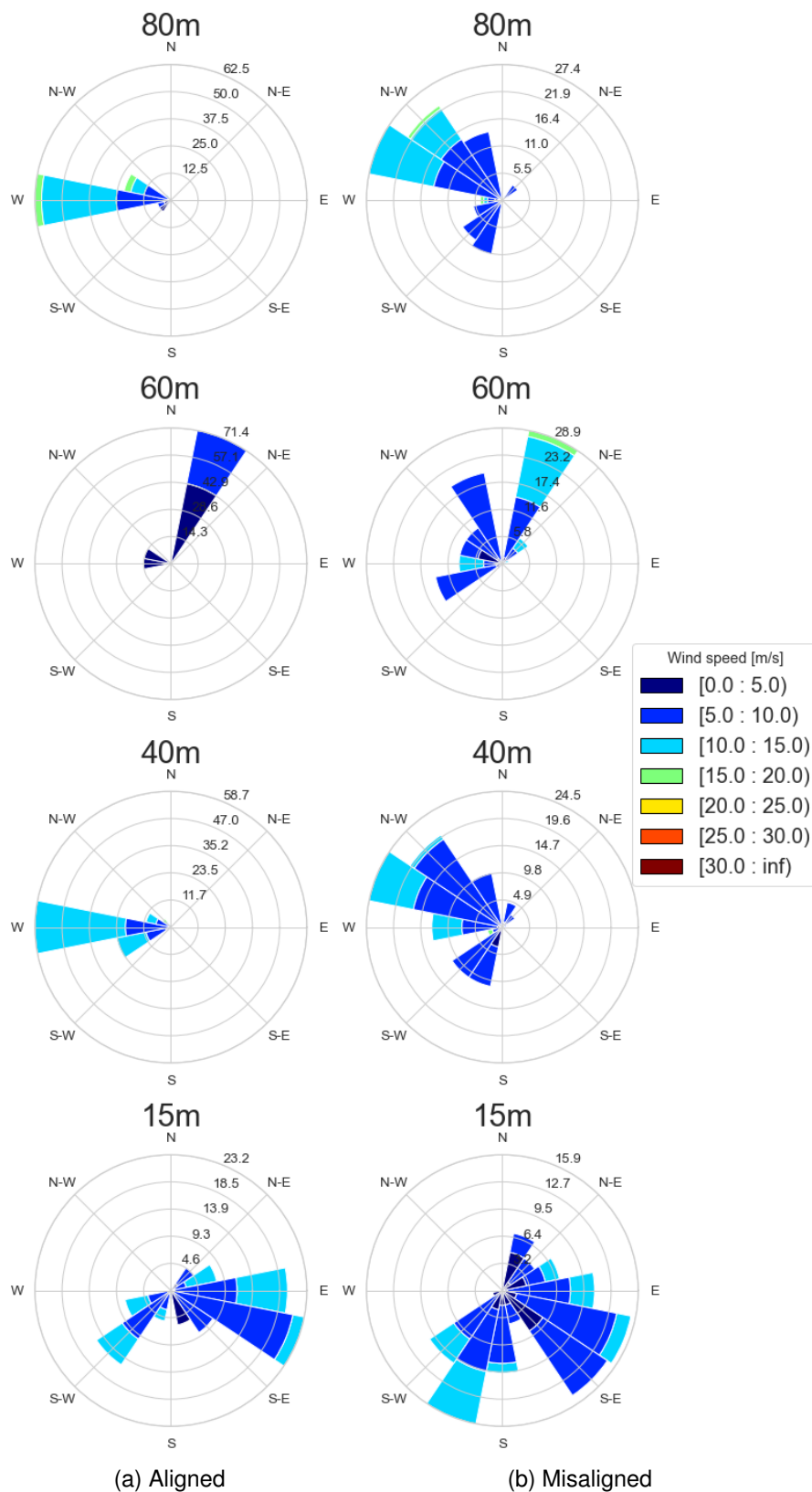
Figure 5.19: Wind roses showing wind veer at FINO1 for aligned- and misaligned wind waves at heights 10 m, 50 m, 100 m and 250 m (ASL). Figure (a) shows aligned wind-wave events, while figure (b) shows misaligned wind-wave events. The wind rose shows wind speed as [m/s] during the period 01.08.2015 − 31.08.2015.

5.2.2 Upward Transfer of Horizontal Momentum
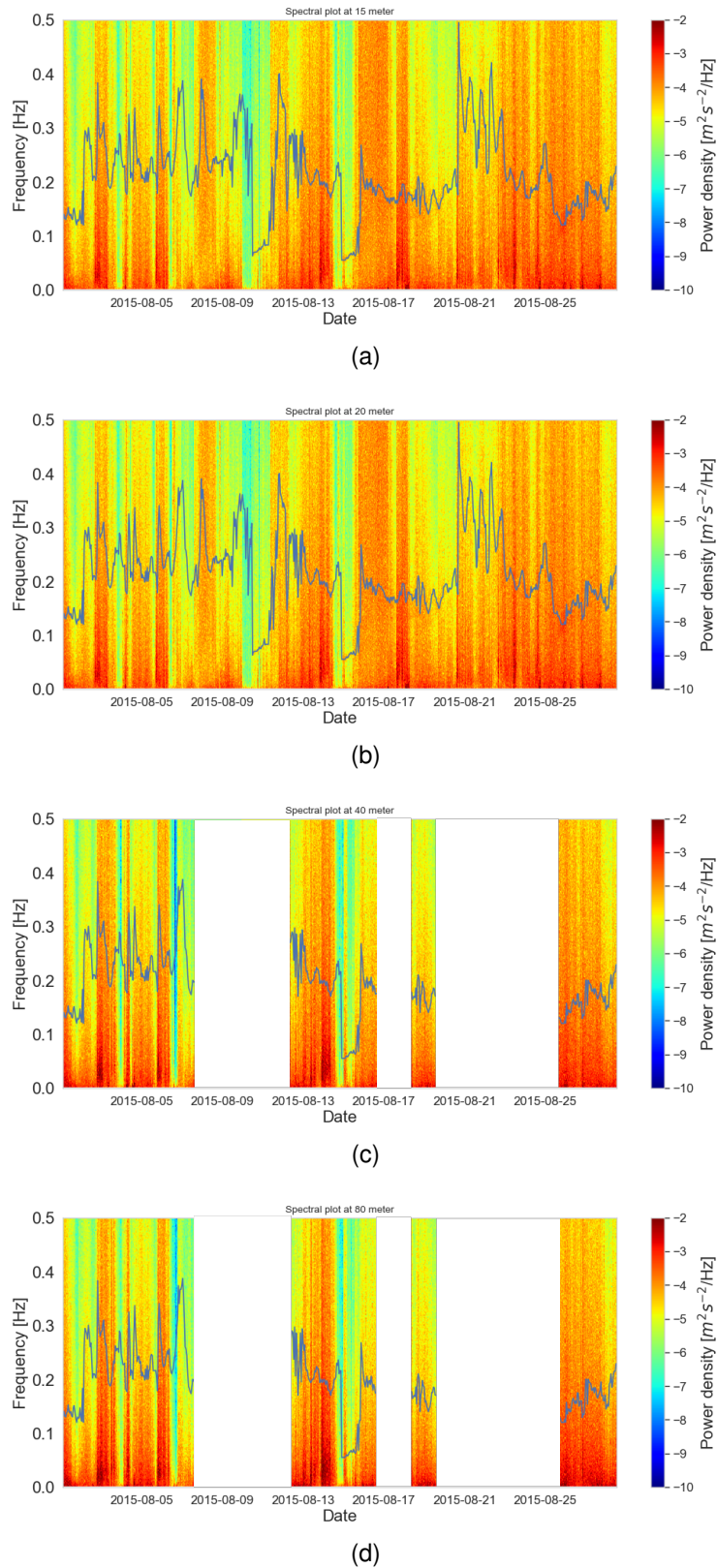
Figure 5.20: *Power spectrum* The figures show the power spectrum for the vertical, w, wind speed overlaid by the wave frequency, where (a) is at 15 m (b) at 20 m (c) at 40 m (d) at 80 m.

Figure 5.20 shows the power density plot for vertical wind speed, w, overlaid by the wave frequency, during August 2015. The measurement data is retrieved from the OBLEX-F1 (15 m and 20 m) measurements campaign and from routinely measurements (40 m, 60 m, 80 m) at FINO1. This figure retrieves information from two independent sensors; (1) wave frequency from a buoy (showed as the black line) and (2) sonic measured spectra at 15, 20, 40 and 80 m. The figure shows footprints of waves in the wind field at the given heights, highlighting how waves interact with the lower part of MABL, where the wave peak frequency follows the inertial subrange of the sonic spectra; the figure indicates that waves affect the wind field.

5.2.3   Wind-Wave Alignment
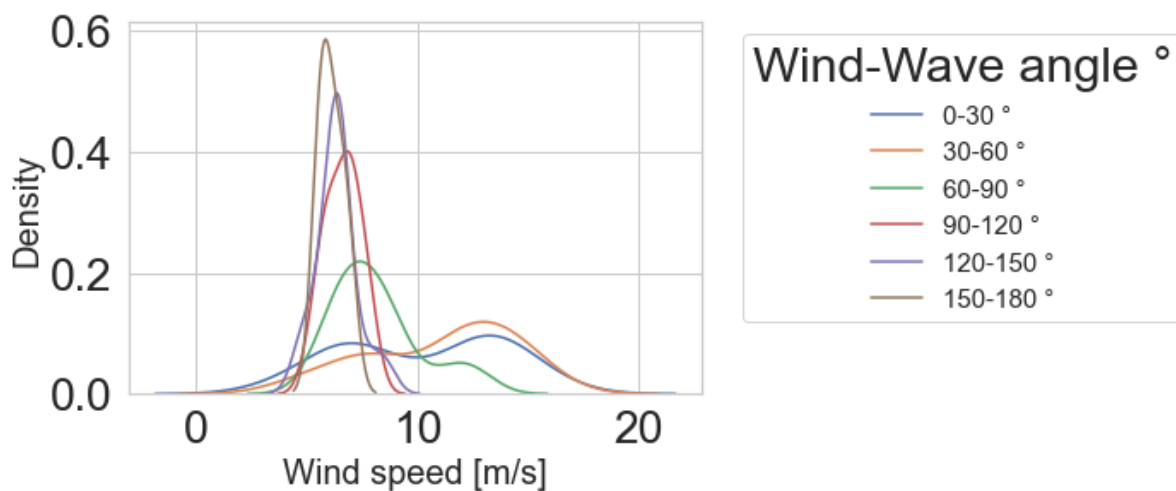
Figure 5.21: Distribution of wind-wave angles at 80 m.

Figure 5.21 shows how the different wind-wave angles are distributed based on wind speed. Higher degrees of wind-wave angles occur for lower wind speeds (below 10 m/s). Lower wind-wave angels, which correspond to aligned- and misaligned wind waves, occur during the full wind speed spectra. Further on, figure 5.22 show the same tendencies as figure 5.21. where the angle between wind and waves decreases with increased wind speed. Figure 5.22 shows how wind direction and wave direction are distributed, where the black line denotes x=y and indicates that wind-wave alignments tend to become more aligned as wind speed increases.

Wind-Wave Alignment	Capacity Factor
Aligned	55%
Misaligned	47%
opposed	33%

Table 5.3: Capacity factor for each wind-wave alignment event.

In Table 5.3 the mean power generated during each wind-wave alignment is shown, where the results show that during aligned wind waves, power is generated at a larger
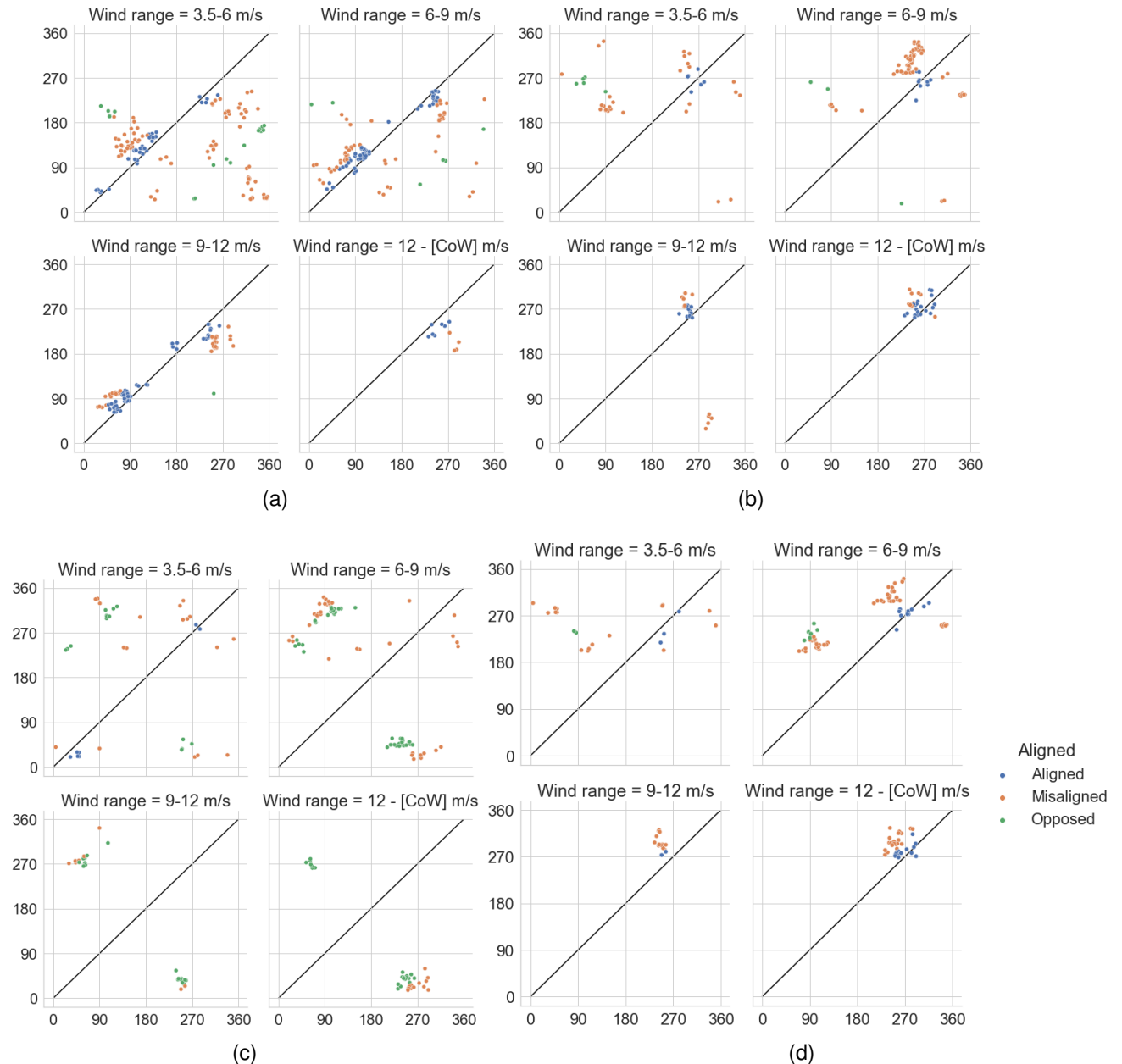
Figure 5.22: **Wind-wave alignment at FINO1** *The figures show how wind speed affects the angle between the wind and the wave, where: (a) shows wind at 15 m; (b) shows wind at 40 m; (c) shows wind at 60 m and (d) shows wind at 80 m. Note that CoW is denoted as Cut-off wind speed at AV4. The x- and y-axis show wave direction and wind direction in degrees, respectively.*

scale, followed by misaligned- and opposed wind-wave events.

Table 5.4 show how wind-wave alignments are distributed, at different heights, during the case study. The wind speed at 60 m indicates that 53% of the wind-wave alignments are opposed, which does not correspond to results at heights 15 m, 20 m, 40 m and 80 m-indicating that the data retrieved at height 60 m is either wrong or affected by the ekman spiral. However, results at all heights, excluding 60 m, indicate that aligned- and misaligned wind waves are the significant contributors where the portion of misaligned wind waves increases by height. Combining the results shown in Table 5.4 with

Height	Wind-Wave Alignments	Occurrence [%]
15 m	Aligned	42.9
	Misaligned	50
	Opposed	7.1
20 m	Aligned	42.9
	Misaligned	50
	Opposed	7.1
40 m	Aligned	28
	Misaligned	67.1
	Opposed	4.9
60 m	Aligned	4
	Misaligned	42.9
	Opposed	53
80 m	Aligned	17.6
	Misaligned	74.2
	Opposed	8.2

Table 5.4: Wind-wave alignment distributed in percent during case study III.

the results in figure 5.23, for wind speed at 80 m, shows that, for all wind-wave alignments, the predominant wind direction is westerly. For both aligned- and misaligned wind waves, the wave direction comes primarily from west/slightly southwest, while for opposed, the predominant wave direction is east.

Figure 5.24 shows probability density plots for wind speed at 80 m (a), normalized power (b), significant wave height (c) and wind-wave angles (d). A probability density plot may be used to identify occurring events. Figure 5.24 (a) builds on the result shown in figure 5.15, where the highest probability of wind speed occurs at the lower intervals. This figure shows that during the period $01.08.2015 - 31.08.2015$, misaligned wind waves occurred more often than aligned- and opposed wind waves. Figure 5.24 (b) shows how the probability of power generation is distributed. The figure shows a considerable variation in wind-wave alignment contributions and power generation. This is a small dataset, stretching over the period $01.08.2015 - 31.08.2015$, with large chunks of data being removed due to filters or limitations, causing it to be highly affected by significant variations. However, 51.65% of the energy generated during case study II occurs below rated power. Further on, the significant wave height (c) is evenly distributed for values between 0 m and 1.5 m. The wind-wave alignments are based on the wind at 15 m. Lastly, figure 5.24 (d) shows the distributions of wind-wave angles at 80 m.
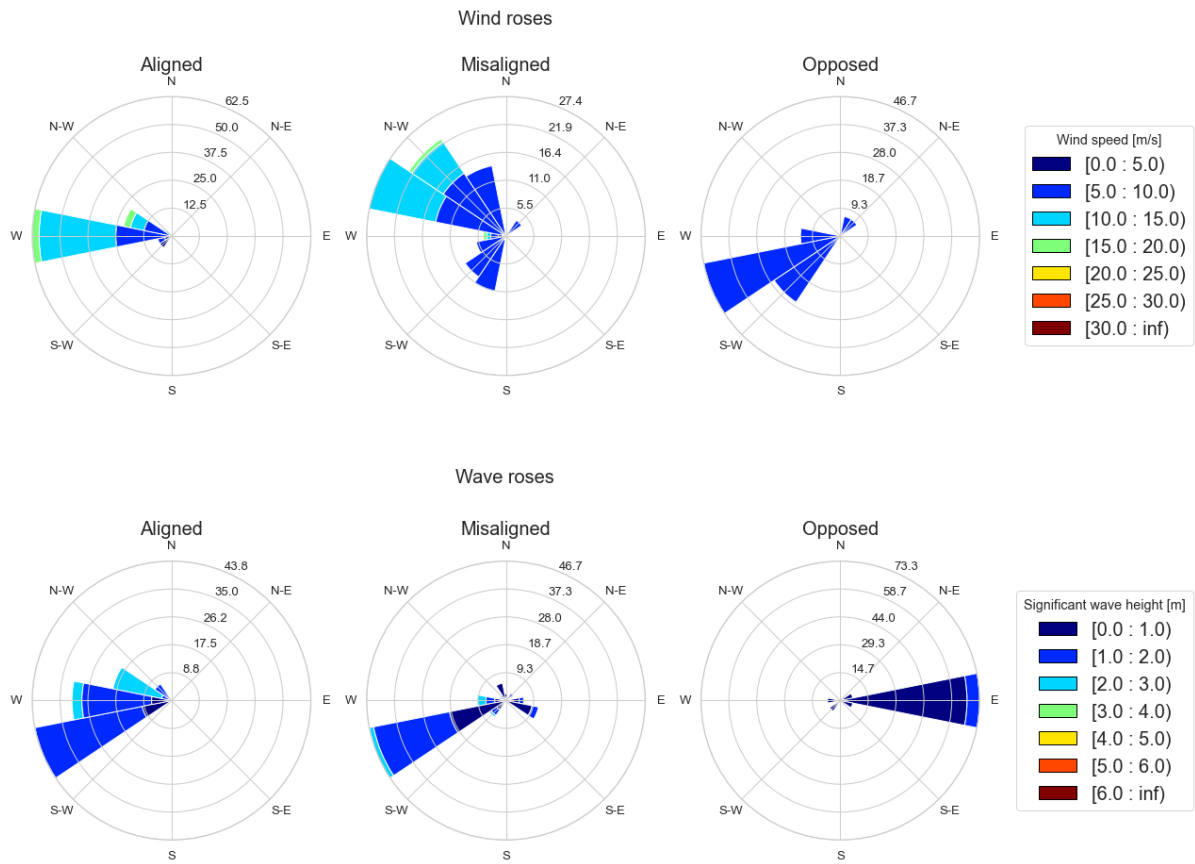
Figure 5.23: Wind and Wave rose.
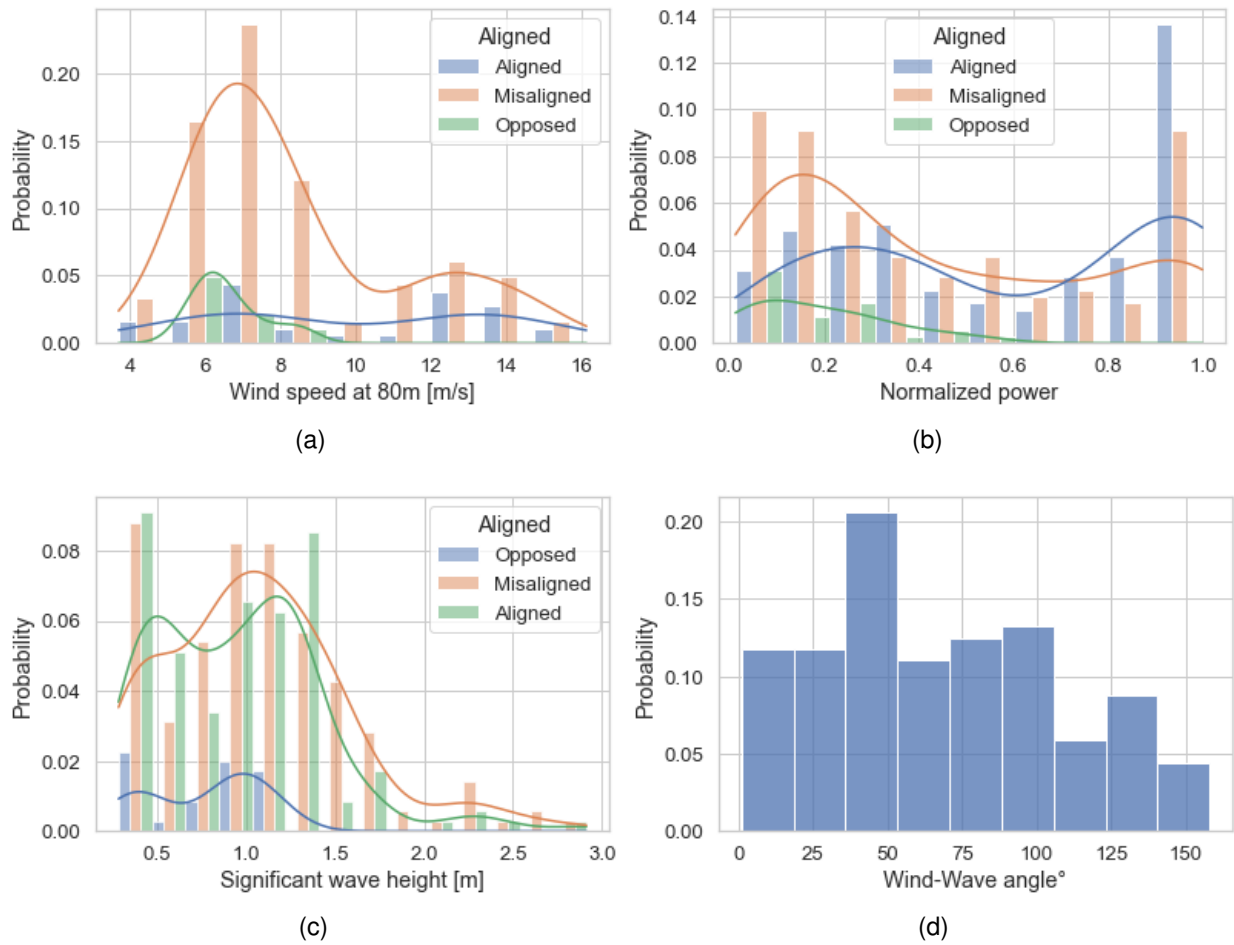
Figure 5.24: **Probability density distributions at FINO1.** *The figures show the probability density distributions of (a) wind speed at 80 m, (b) Active power production, (c) significant wave height and (d) the angle between wind and wave.*

5.3   Case Study III

Case study III is the last case study looking at wind-wave interactions around FINO1 and Alpha Ventus. This case study covers two years of reanalysis data from NORA3. The objective of this case study is to investigate the environmental conditions, indications of upward transfer of horizontal momentum and wind-wave alignments found in the period $01.01.2015 - 01.01.2017$.

5.3.1   Environmental Conditions
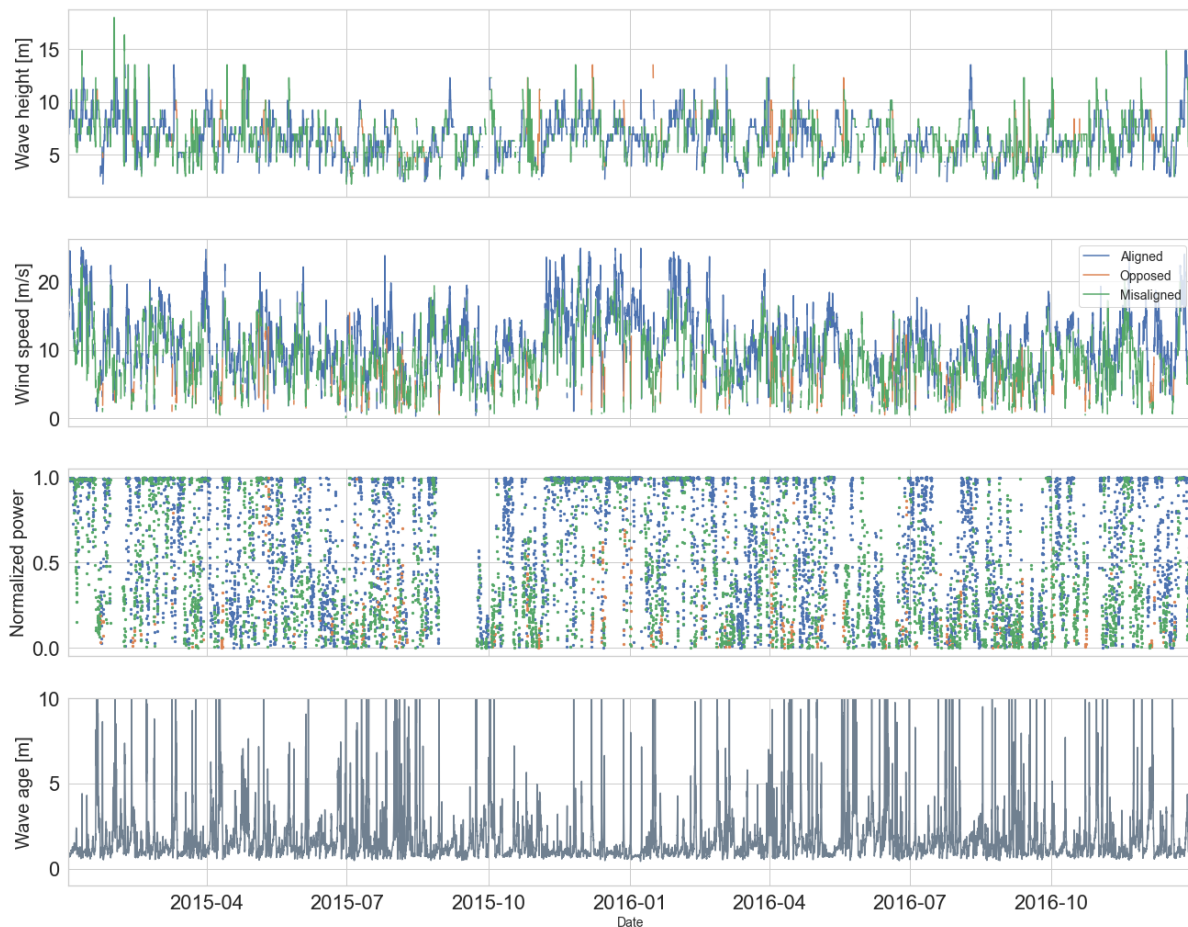
Figure 5.25: Time series of wind speed (100 m ASL) and significant wave height at FINO1, normalized power at AV4, and wave age. The time series shows how the distribution of different wind-wave alignments throughout the period and how they compare to the wave age. The measurement is from the period $01.01.2015 - 01.01.2017$.

Figure 5.25 shows the time series of significant wave height, wave age, wind-wave alignment and wind speed at FINO1 and normalized active power at AV4. In events of missing data segments, either removed by filters or not available, these are visible as blank segments/gaps in the figure 5.25 . The time series provides a visual expression of the variability of the wind speed and how it affects power generation. The time series are categorized into aligned, misaligned, and opposed. These three categories can help us understand the importance of wind-wave conditions for the offshore wind industry.

As this time series is dependent on NORA3, different results are expected compared to observed data from FINO1 (case study I and II).

The variations in wind speed, significant wave height and normalized power are observable during the period shown in figure 5.25. Additionally, the time series show a slight increase in wind speed and significant wave height during winter.
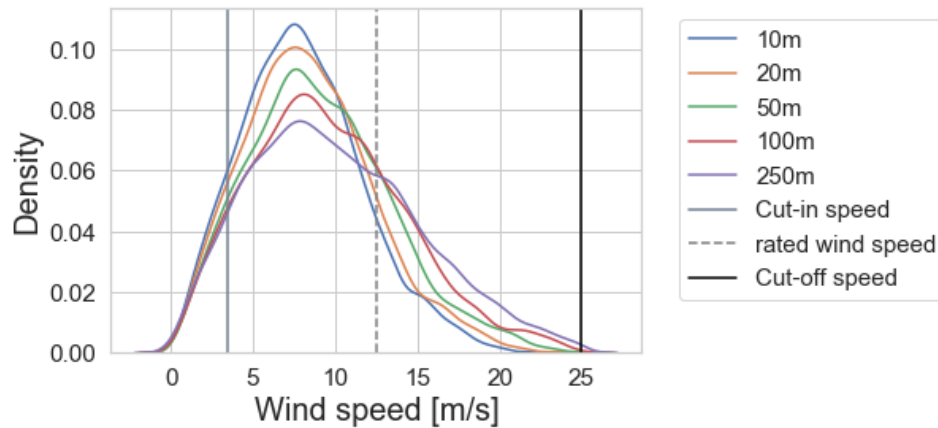
Figure 5.26: Density distribution for different wind speeds. Cut-in speed is at 3.5 m/s, rated wind speed is at 12.5 m/s and cut-off wind speed is at 25 m/s.

Figure 5.26 shows the density distribution of wind speed across several heights constructed using consecutive 2-year reanalysed time series. The figure clearly shows that wind speed between cut-in and rated wind speeds has the highest probability of occurrence. Thus, this wind speed interval is significant for offshore wind power generation as this dataset suggests that 63-85% (depending on height) of all wind speeds above cut-in speed occurs here. The figure shows that higher elevations encounter a higher density of substantial wind speeds. Table 5.5 show how the wind-wave alignments are distributed over height.

Height	Wind-Wave Alignments	Occurrence [%]
10 m	Aligned	53.1
	Misaligned	34.8
	Opposed	5.2
20 m	Aligned	53.1
	Misaligned	34.8
	Opposed	5.2
50 m	Aligned	53.2
	Misaligned	34.9
	Opposed	5.6
100 m	Aligned	53.4
	Misaligned	34.8
	Opposed	5.6
250 m	Aligned	54.2
	Misaligned	34.5
	Opposed	5.2

Table 5.5: Wind-wave alignment distributed in percent during case study III.

(a)   (b)

Figure 5.27: **Weibull parameter plotted against significant wave height** *The figures show how the Weibull parameters change from aligned to misaligned wind waves: (a) the shape parameter; (b) the scale parameter. The data is calculated using 5 bins from [0, Max].*

(a)   (b)

(c)   (d)

Figure 5.28: **Weibull parameter plotted against wind speed** *The figures show how the Weibull parameters change from aligned to misaligned wind waves: (a) the aligned shape parameter; (b) the aligned scale parameter; (c) the misaligned shape parameter, and (d) shows the misaligned scale parameter. The data is calculated using 5 m/s bins, [0, CoW) (CoW = cut-off wind speed).*

The results in figure 5.28 is summarized in Table 5.6, where differences between

Height [m]	Aligned Mean Wind Speed [m/s]	k	c	Misaligned Mean Wind Speed [m/s]	k	c
10	5	8.55	5.1	4.83	7.56	4.94
	7.61	10.16	7.79	7.44	9.64	7.62
	10.38	13.13	10.57	10.24	12.61	10.44
	13.25	16.11	13.45	13.08	15.86	13.28
	16.24	19.67	16.45	15.68	23.55	15.7
	19.01	24.15	19.19	-	-	-
	22.29	34.74	22.41	-	-	-
20	4.98	8.35	5.08	4.86	7.55	4.97
	7.61	10.11	7.79	7.46	9.52	7.64
	10.44	13.52	10.62	10.27	12.42	10.48
	13.28	16.58	13.49	13.09	14.9	13.30
	16.35	21.35	16.54	16.05	21.54	16.21
	19.02	22.96	19.21	19.13	34.84	19.24
	22.03	18.1	22.38	-	-	-
50	4.95	8.34	5.05	4.80	7.25	4.91
	7.61	10.17	7.78	7.48	9.73	7.65
	10.52	13.95	10.70	10.3	12.80	10.49
	13.37	16.68	13.57	13.22	16.45	13.41
	16.3	19.43	16.53	16.22	19.53	16.44
	19.36	23.83	19.58	19.00	20.48	19.24
	22.12	20.80	22.40	-	-	-
100	5.12	9.88	5.18	4.98	8.63	5.07
	7.65	10.39	7.82	7.57	10.06	7.75
	10.54	13.68	10.74	10.38	12.48	10.59
	13.46	17.07	13.67	16.23	16.31	13.56
	16.28	19.71	16.49		19.70	16.44
	19.24	22.53	19.46	18.96	29.87	19.07
	22.41	22.12	22.7	22.18	74.09	2.17
250	4.93	8.07	5.03	4.79	7.43	4.9
	7.62	10.29	7.8	7.52	9.91	7.69
	10.53	13.51	10.73	10.34	12.88	10.53
	13.48	17.43	13.68	13.32	17.49	13.50
	16.40	20.47	16.62	16.26	20.74	16.46
	19.38	24.55	19.59	19.12	24.51	19.3
	22.72	20.44	23.08	22.5	20.48	22.86

Table 5.6: Weibull parameters. Data is stored in bins of a size of 3 m/s. If the amount of data points within each bin is below 1% of the total length of the dataset, it is not used.

wind-wave alignments is shown. Figure 5.28 shows the Weibull parameters shape (k) and scale (c) and how it varies as the wind speed increases, where (a) shows the aligned shape parameter, (b) the aligned scale parameter, (c) the misaligned shape parameter and (d) shows the misaligned scale parameter. The figure shows larger differences in the shape parameter for higher wind speeds, whereas there are a significant difference between (a) and (c). In figure 5.28 (c) we see large differences between the shape parameters for wind speed above 17.5 m/s, whereas the same split occurs later in (a).
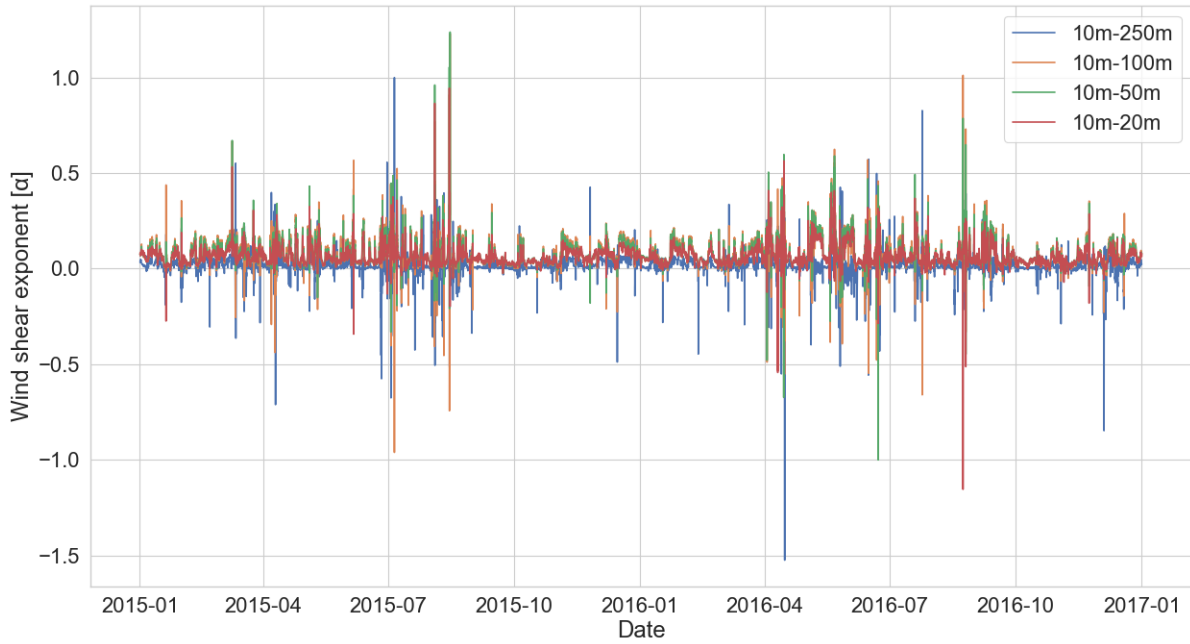
Figure 5.29: Wind shear exponents for heights 10, 20, 50, 100 and 250 m.

In figure 5.29, the shear exponents for different heights is calculated using equation 2.6 for power law. A larger distance between the coupled heights yields larger variations in the shear exponent. The shear exponent for 10 m-100 m (orange) and 10 m-250 m (blue) shows larger negative values and larger positive values. However, the results are more significant looking at the lower values of shear exponents. Figure 5.30 show some deviation between lower shear exponent values and the actual power curve. However, they fit better to the actual power curve than to larger shear exponent values.
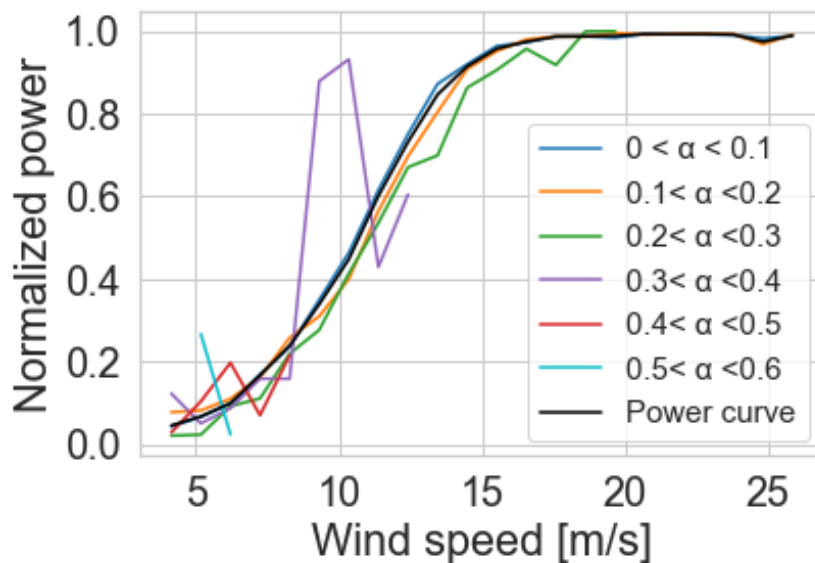
Figure 5.30: Power curve depending on shear exponent values, where the shear exponent values is calculated using wind speed at height 10 m and 100 m.

The wind rose in figure 5.31 shows the distribution of wind speed direction at heights 10 m, 50 m, 100 m and 250 m. The wind rose separates wind speed using bins of 5 m/s. The wind direction shown is the direction the wind is blowing from, e.g. the predominant wind direction in the aligned wind roses shows that wind is blowing from a westerly direction. The predominant wind direction for aligned wind waves is westerly, with occasional northwesterly and south-westerly winds. For misaligned, the predominant direction is south-westerly with occasional easterly winds. Elevation and wind-wave alignment affect the magnitude of wind speed, where wind speed increases with increased elevation and is higher for aligned wind waves than misaligned wind waves. The wind rose shows that the predominant wind direction for substantial wind speeds (above 20 m/s) is coming from west/south-west for aligned wind waves. For misaligned wind waves, the predominant wind direction during substantial wind speeds (above 15 m/s) is south-westerly. Furthermore, the figure 5.31 shows little difference in wind direction by height for both aligned- and misaligned wind waves.
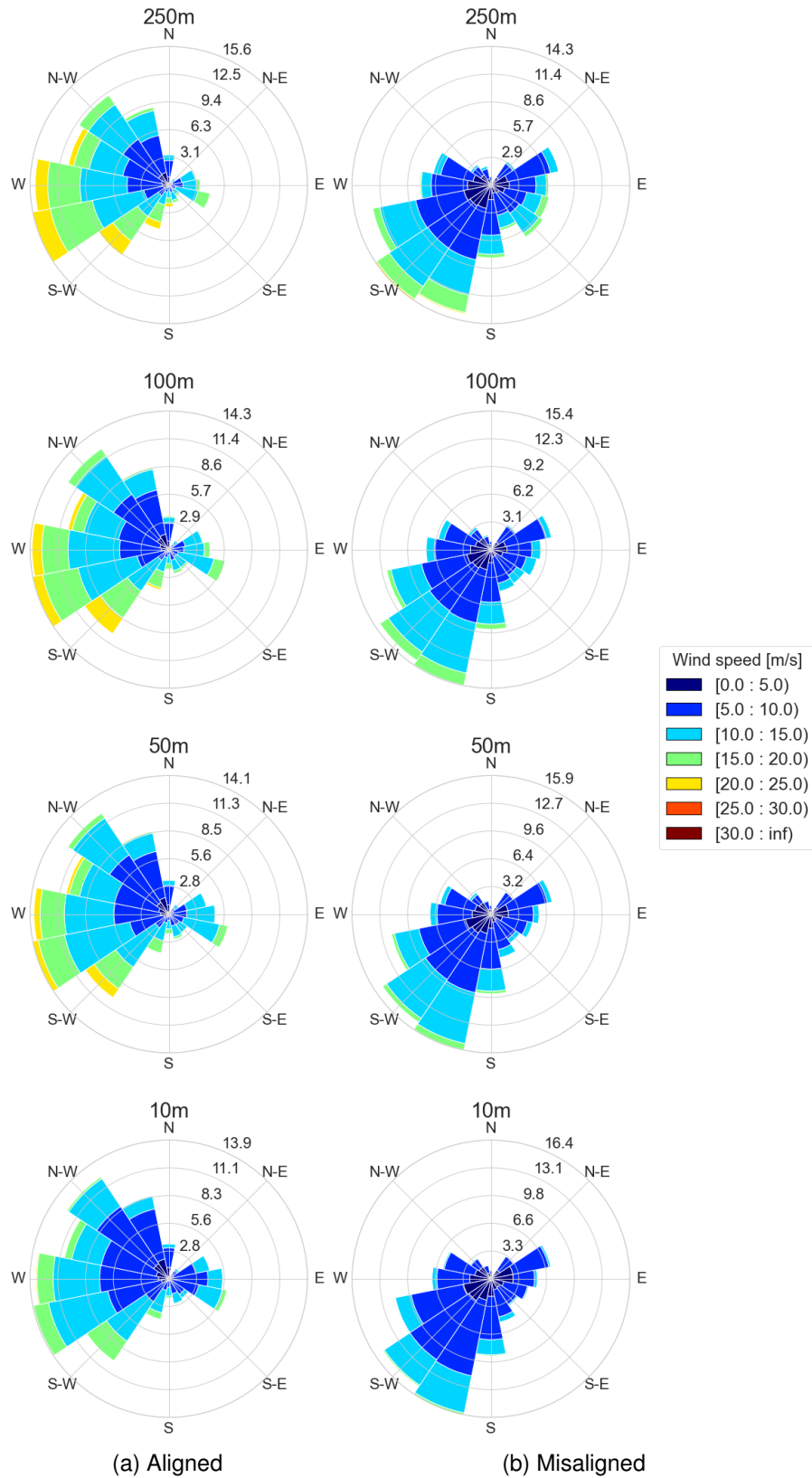
Figure 5.31: Wind roses showing wind veer at FINO1 for aligned- and misaligned wind waves at heights 10 m, 50 m, 100 m and 250 m (ASL). Figure (a) shows aligned wind-wave events, while figure (b) shows misaligned wind-wave events. The wind rose shows wind speed as [m/s] during the time period 01.01.2015 − 31.01.2017.

5.3.2   Upward Transfer of Horizontal Momentum
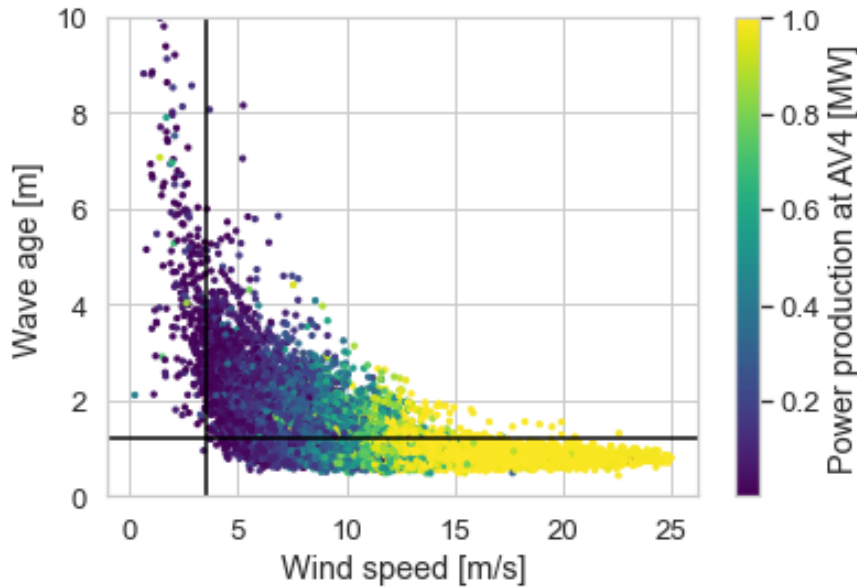
Figure 5.32: Wave age is plotted against wind speed at 100 m (ASL), with a color bar indicating power generation. The vertical black line indicates the turbine cut-in speed, while the horizontal black line corresponds to a wave age value of 1.2.

Figure 5.32 shows the wave age plotted against wind speed with a colour bar indicating power generation. For higher wind speeds, the result suggests that the effect of the swell waves is suppressed, as the wave age is moving below wave age ratio 1.2. However, for wind speeds above 15 m/s, there are still events with a wave age ratio above 1.2, even though they do not seem to affect the power generation significantly. More considerable variation in the energy generated is present in the wind speed interval between 5 m/s - 15 m/s. For events where energy generation is below rated power, the figure indicates that wave age > 1.2 is more common than wave age < 1.2.
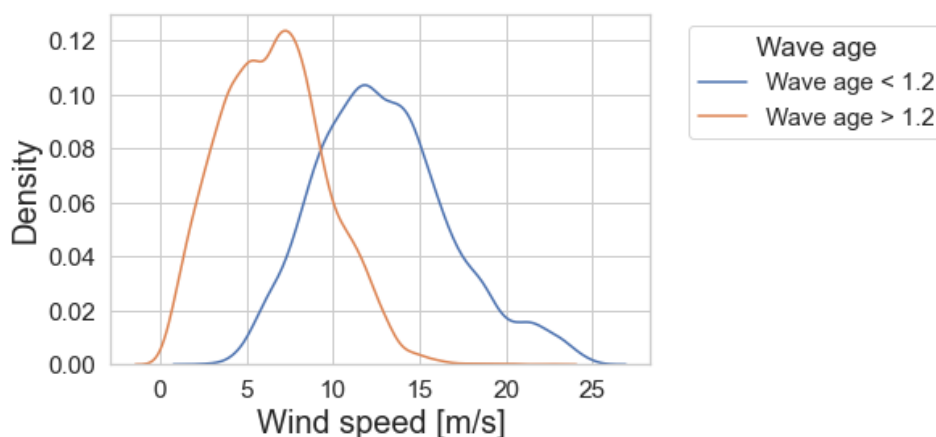
Figure 5.33: Density distribution showing wind speed at 100 m connected with wave age.

As mentioned in section 2.3.1, the wave age is the ratio between wave phase speed and wind speed at 10 m. Figure 5.33 shows how wave age above and below 1.2 distributes. Wave age < 1.2 occurs more frequently at lower wind speeds (0-10 m/s) than
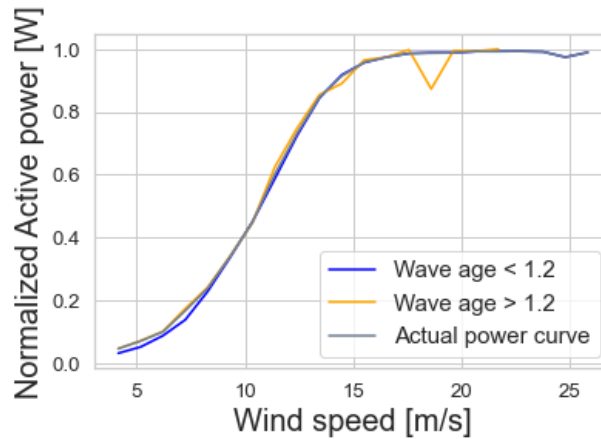
Figure 5.34: Power curve visualising the difference in power generation during wave age ratios above and below 1.2, where wave age > 1.2 is the first indication of probable upward transfer of horizontal momentum.

wave age > 1.2. Furthermore, the wind speed interval with a wave age ratio above 1.2 coincides with the same area as for high wind-wave angles in figure 5.36. Most wind-wave angles peak in the interval 0 -10 m/s—indicating that wind-wave angles and wave age are present during lower wind speeds at the height of 100 m ASL.

Figure 5.34 shows a power curve plotted based on wave age values. Figure 5.34 shows how the power curve performs when the wave age is above and below 1.2, giving only a small indications of performance effects between the two wave ages. During low wind speeds, 3. 5 m/s to 8 m/s, a small deviations is visible, where the power curve with wave age > 1.2 performs better than the power curve with wave age < 1.2.

5.3.3 Wind-Wave Alignment

Figure 5.35 shows how the wind profile changes depending on the present wind-wave alignment, where the wind profile for aligned wind-wave yields the highest wind speeds. The figure also shows that for aligned wind-waves the wind speed increases more by height, compared to misaligned- and opposed wind-waves. Further on, the result may indicate that during opposed- and misaligned wind-waves the waves slows down the wind speed even at higher altitudes.

Figure 5.36 shows the density distribution for the different wind-wave angles, where the distributions of alignments at 100 m are summarised in Table 5.7. The figure suggests that higher degrees of wind-wave misalignment are more common for low wind speeds, while for higher wind speeds, the wind-wave angle decreases.
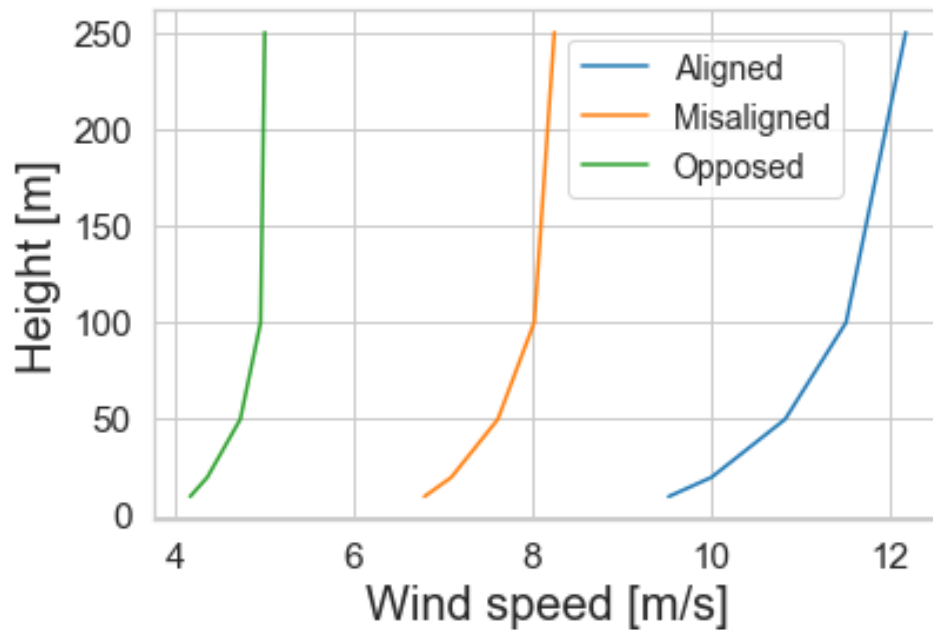
Figure 5.35: Wind profiles for each wind-wave alignment were calculated using data from heights 10 m, 20 m, 50 m, 100 m and 250 m. The wind profile is calculated by taking the mean wind speed at each height.
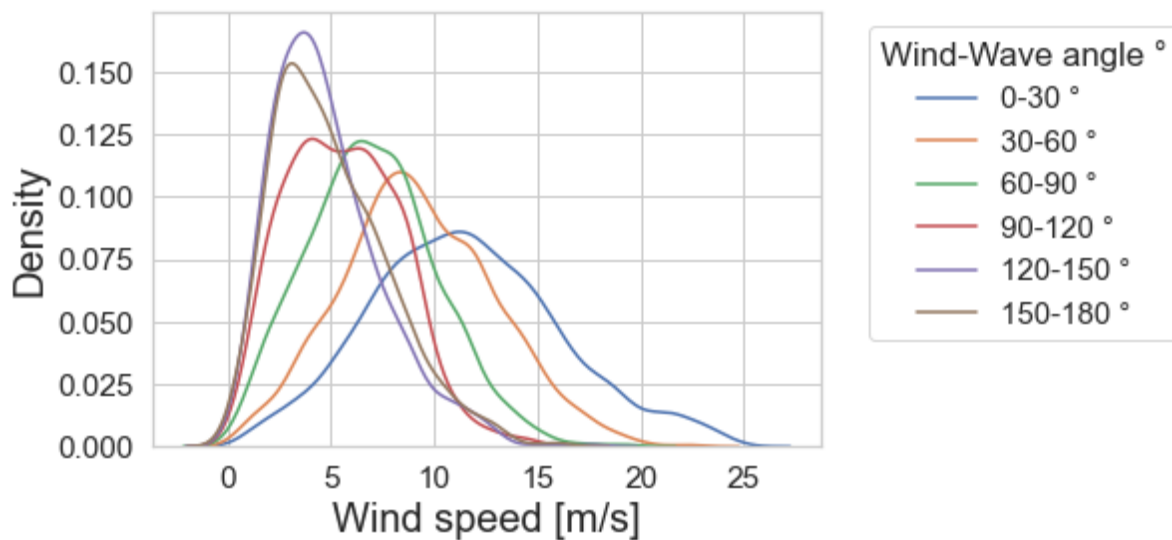
Figure 5.36: Density distribution for different wind-wave angles at 100 m.

Wind-Wave Alignment	Occurrence [%]
Aligned	53.4
Misaligned	34.8
opposed	5.6

Table 5.7: Wind-wave alignment distributed in percent over the time period 01.01.2015 − 31.01.2017. Wind speed is captured at height 100 m ASL.
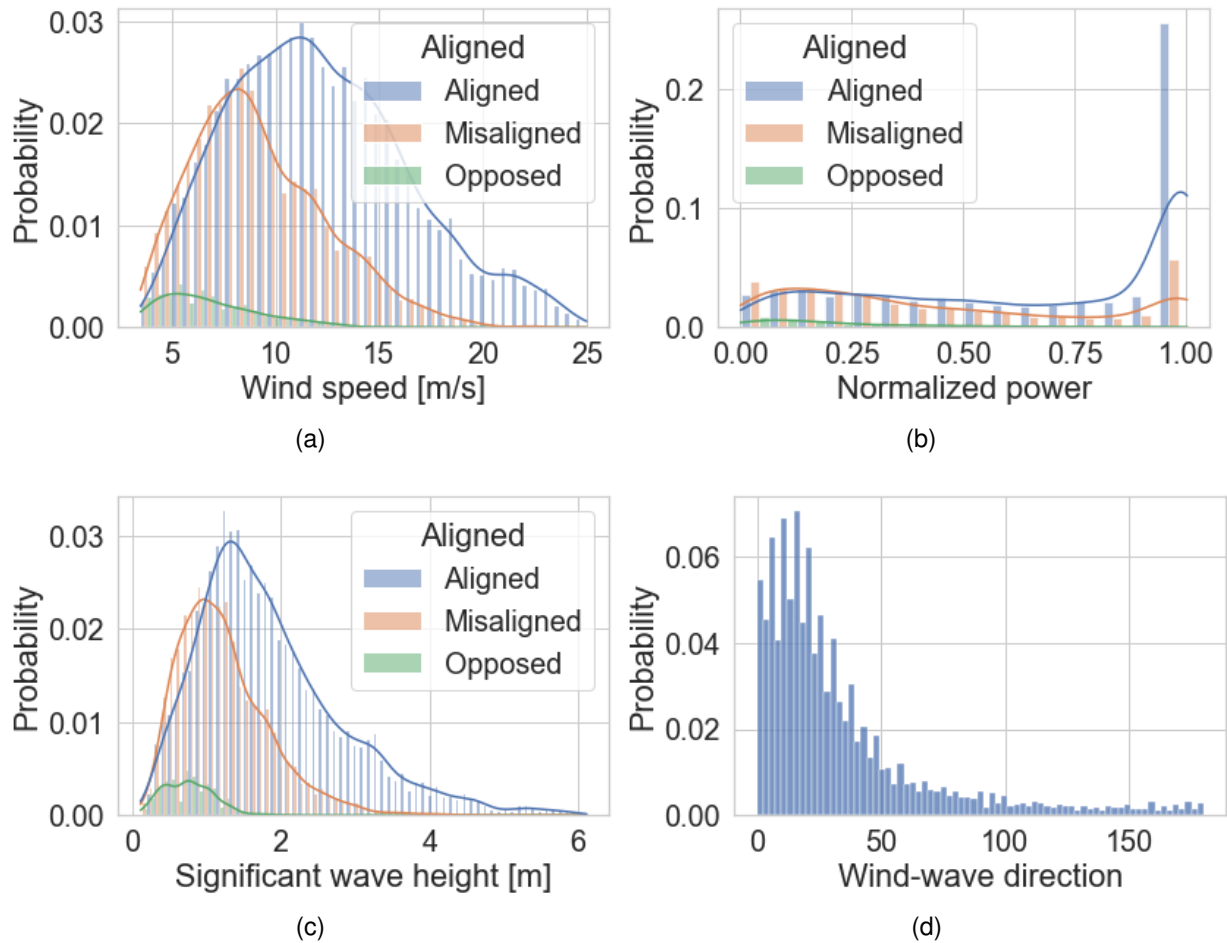
*Figure 5.37: **Probability density distributions (PDF) based on NORA3 data.** The figures show the probability density distributions with overlaying Kernel density estimate of (a) wind speed at 100 m, (b) normalized power generation, (c) significant wave height and (d) the angle between the wind and wave directions at 100 m.*

Figure 5.37 shows probability density plots for wind speed at 100 m (a), normalized power (b), significant wave height (c) and wind-wave angles (d). For the FINO1 area, figure 5.37 (a) shows the distribution of wind-wave alignment at a height of 100 m (ASL). Aligned- and misaligned wind-wave cases dominate the distribution. However, only aligned wind waves are present for higher wind speeds (above 20 m/s). In accordance with figure 5.26, the wind speed interval between 5 m/s and 15 m/s has the highest occurrence of wind speed, where misaligned- and aligned wind waves occur at a similar rate. Opposed wind waves occur only for lower wind speed intervals and are not present in the dataset above 13 m/s. Figure 5.37 (b) shows the distribution of

normalized generated power, where power generation at rated power is most common. In accordance with figure 5.37 (a), we see that aligned wind-waves are most common for rated power. In this case, 42.7 % of the energy generated during the time period $01.01.2015 - 31.01.2017$ is below rated power. Further on, the significant wave height (c) follows the same shape as for wind speed at 100 m (a), where high values of significant wave height corresponds to aligned wind waves. Lastly, figure 5.37 (d) shows the distributions of wind-wave angles at 100 m, indicating that the angle between wind and wave mainly is between 0-50°.
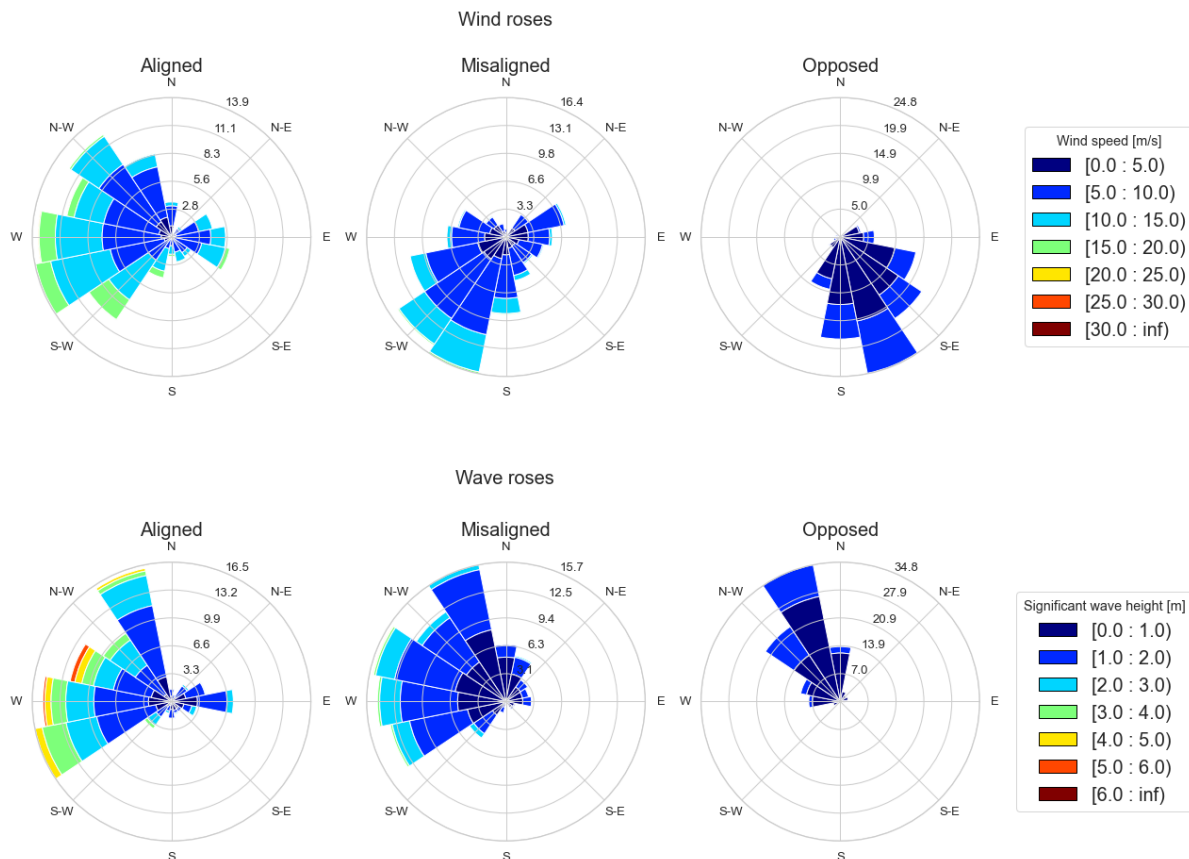
Figure 5.38: Wind- and wave roses showing the direction of wind and waves during different wind-wave alignment conditions, during the period $01.01.2015 - 31.01.2017$. The wind rose shows wind speed as [m/s], while the wave rose shows significant wave height as [m].

The wind- and wave rose in figure 5.38 shows the distribution of wind/wave directions during aligned-, misaligned- and opposed wind waves. The wind rose separates wind speed using bins of 5 m/s, while the wave rose separates the significant wave height using bins of 1 m/s. The wind direction and wave direction are shown as the direction it is coming from. The results provided in figure 5.38 are comparable to the results in figure 5.13, where the predominant direction for aligned wind waves is westerly for both wind and waves. For misaligned wind waves, the predominant direction is south-westerly for wind and westerly for waves, where we encounter occasional waves from a north-westerly direction. Furthermore, for opposed wind waves, the predominant direction is south/south- easterly for wind and north/north-westerly for waves, causing the wind to blow from land through the Alpha Ventus wind park. The figure shows that wind speed and significant wave height are highest during aligned wind

waves, followed by misaligned wind waves. The length and colour of each direction segment represent wind/wave strength, while the grey circles show normalized data as percentages. The results presented in figure 5.38 and 5.13 are in line with the results shown by Porchetta et al. [16]. The wind rose indicates that aligned- and misaligned wind waves occur more often during stronger wind speeds than opposed wind waves.
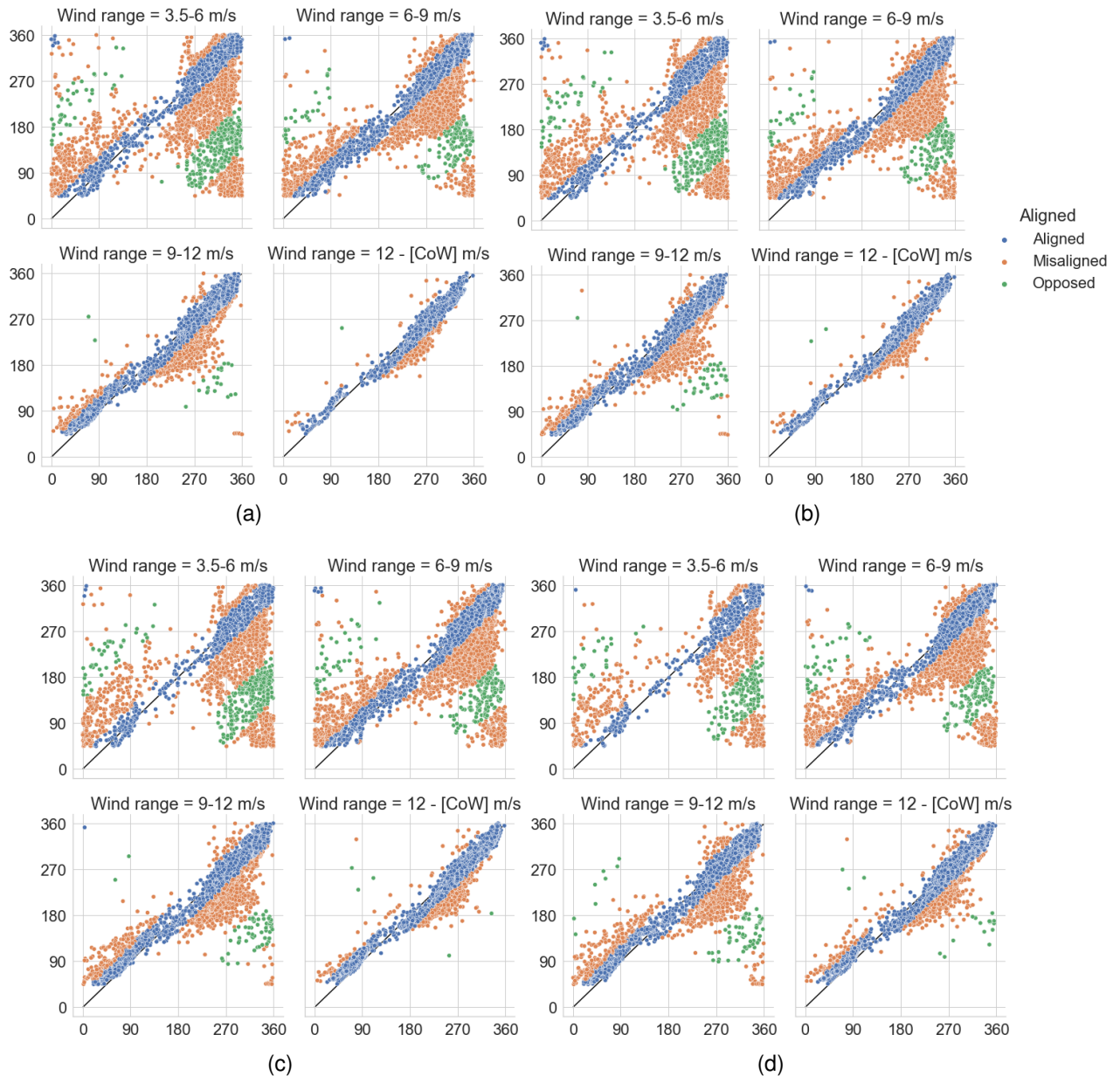
Figure 5.39: **Wind-wave alignment at FINO1 using NORA3 data.** *The figures show how wind speed affects the angle between the wind and the wave, where: (a) shows wind at 10 m; (b) shows wind at 20 m; (c) shows wind at 50 m and (d) shows wind at 100 m. Note that CoW is denoted as Cut-off wind speed at AV4. The x- and y-axis show wave direction and wind direction in degrees, respectively.*

The angle between wind and wave is highly dependent on wind speed. Higher wind speeds have a higher occurrence of aligned wind and waves. Figure 5.39 shows how wind direction and wave direction are distributed, where the black line in the middle
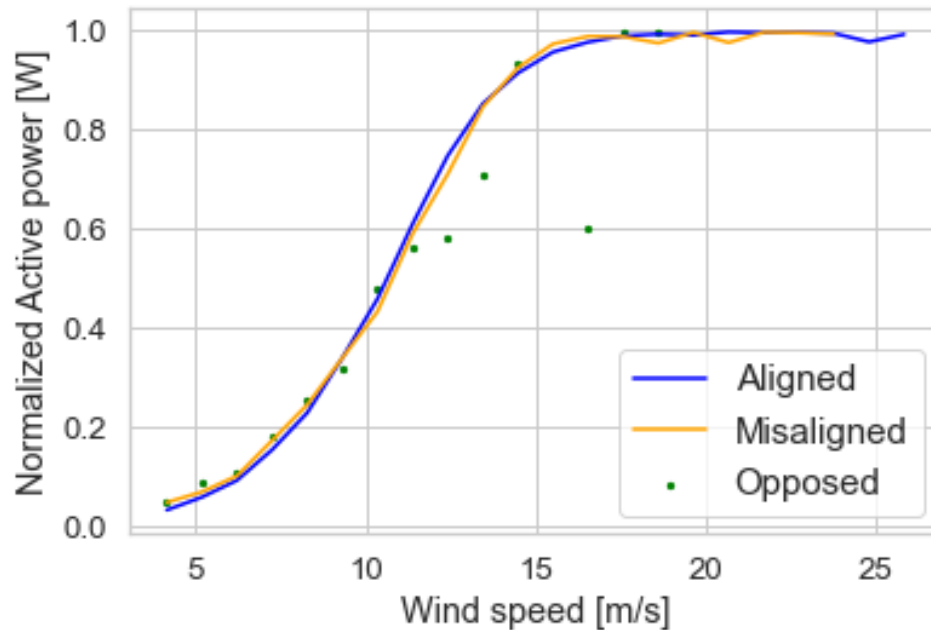
Figure 5.40: **Normalized power curve at AV4 using NORA3 data.** *The figures show how the power generation is affected by wind-wave alignment, where opposed wind waves are shown as dots, while aligned- and misaligned wind waves are shown as curves.*

denotes x=y. The results provided in the figure indicate, for all heights, that the wind-wave alignments tend to become more aligned as wind speed increases.

In figure 5.40, the power curves are separated by wind-wave alignments, where the opposed wind-waves power curve is plotted as dots due to the low sample size. Figure 5.40 show only little tendencies of performance differences between the wind-wave alignments. By comparing the aligned-, misaligned and opposed wind-waves power curves to the actual power curve, which is not separated by alignments, the aligned wind-wave power curve overperforms by 0.1% while the misaligned wind-wave power curve underperforms by 0.22% and the opposed by 8.22%. However, the opposed wind-wave power curve is disregarded due to insufficient amount of measurements.

The wind shear exponents profiles for each wind-wave alignment is shown in figure 5.41, where we see a clear distinction between the different alignments. A large exponent will indicate a larger vertical wind shear increase in the wind speed, and as seen from the figure aligned wind waves returns a higher wind shear exponent compared to misaligned- and opposed wind waves.
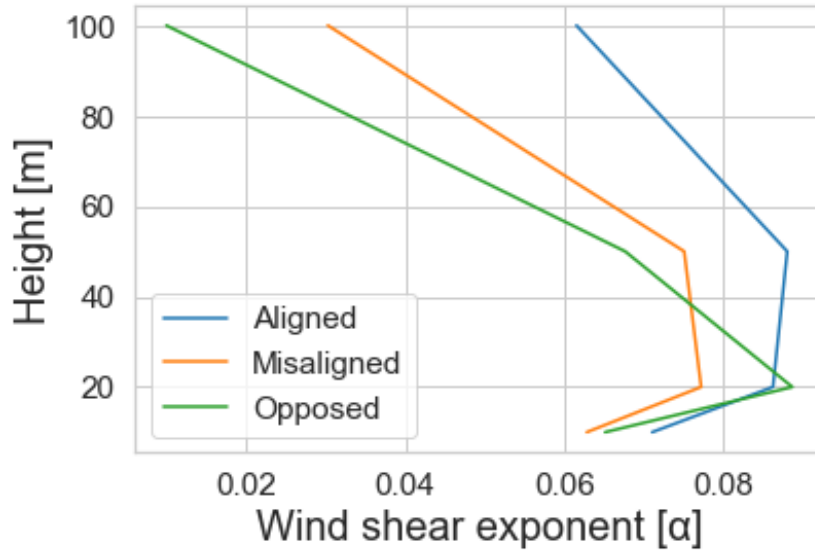
Figure 5.41: Shear was calculated at four different steps: 10-20 m, 20-50 m, 50-100 m and 100-250 m. All lines show how the wind shear exponent changed depending on height (from 10 m to 250 m).

5.3.4   Environmental Contour
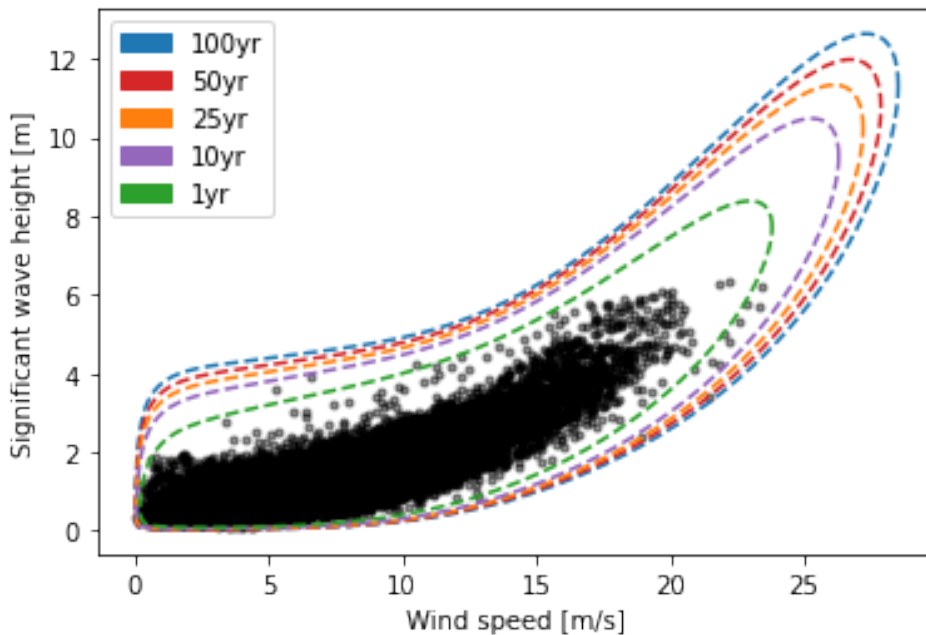
Figure 5.42: Environmental Contour of wind speed and significant wave height. Show contour lines for 100, 50, 25, 10 and 1 year. Computed using the python tool ViroCon [80].

Figure 5.42 show the environmental contour for 100, 50, 25, 10 and 1 year, based on 2 years of NORA3 wind and wave data. The environmental contour lines show the multivariate extreme of environmental conditions. The figure indicates how significant wave height increases with wind speed. The figure gives an indication of expected wind and wave forces during each period, where any given value in e.g. the 100 year contour, have a probability of $(1/100 years) \times 100 = 1\%$ to occur every year. Based on the 100

year contour line, the figure indicates maximum extreme values of wind speed at above 25 m/s (above cut-off speed) and significant wave height at 12 m.
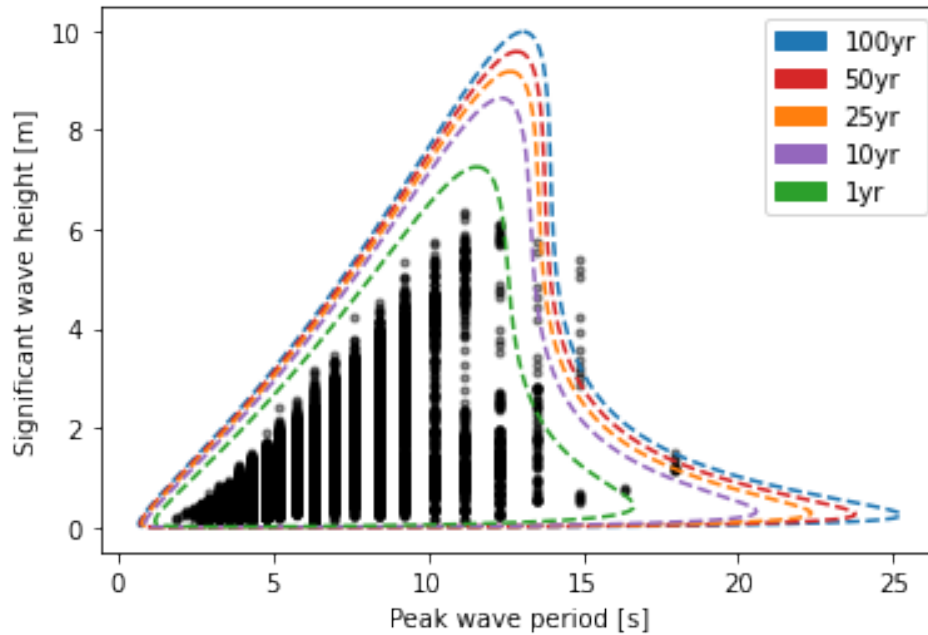
Figure 5.43: Environmental Contour of peak wave period and significant wave height. Show contour lines for 100, 50, 25, 10 and 1 year. Computed using the python tool ViroCon [80].

Figure 5.43 shows an environmental contour for peak wave period against significant wave height, with contour line at 100, 50, 25, 10 and 1 year. The figure indicates how the peak wave period changes based on significant wave height, where the significant wave height reaches a maximum extreme value between a peak wave period of 10-15 seconds. The contour plot also show indication of presence of swell waves in the dataset, as swell waves are typically described with a long wave length (corresponding to a long peak wave period). The two maximum extreme values occurring during the 100 year contour line is (1) significant wave height of 10 m and a peak wave period of 13 seconds, and (2) significant wave height of 0.3 m and a peak wave period of 25 seconds.

Chapter 6

Discussion

In the following chapter, a discussion clarifying the results shown in chapter 5 is presented. Here, how wind-wave interaction affects power generation, focusing mainly on the alignment between wind and waves and the vertical transfer of horizontal momentum, will be discussed. In addition, other plots and analyses, shown in the result, will be included. The foundation of this analysis is the data collected at FINO1(during the OBLEX-F1 measurement campaign and routinely performed measurements at FINO), the NORA3 dataset and SCADA data at Alpha Ventus 4, AV4. Three case studies, dependent on different data/sensors, have given us comparable results which can be used to identify environmental patterns.

This thesis aims to contribute to combining research about wind and waves with respect to the wind industry by; (1)investigating the effects of misalignment on energy generation, (2) i conducting a process study using energy spectra, atmospheric stability, some (higher-order) statistics, two-point statistics, wind shear and veer and (3) providing an environmental contour based on NORA3 data.

6.1   Key Findings

How do different wind-wave interactions interfere with the surrounding wind field, affecting turbine performance? Moreover, how big of a contribution do these interactions yield? The research question stated in the motivation section (1.2) specifies that this thesis aims to enhance and cohere the research on wind-wave interactions with the wind industry by using wind-wave measurements and connecting them with power data from a nearby wind turbine.

The main results gained from this analysis suggest that wind-wave alignments affect the wind field and power curve at wind speeds between cut-in and rated. Further, analysis of the vertical transfer of horizontal momentum indicates contributions from waves, where vertical transfer of horizontal momentum directly influences the air above the ocean waves. However, no clear indications of upward momentum affecting power generation are found. Two environmental contour plots also provide an insightful view into the environmental conditions at the measurement site. Lastly, essential processes and variables such as Weibull parameters and wind shear coefficients have been identi-

fied.

6.2   Wind-Wave Interactions Effect on Power Generation

In line with Porchetta's study [16] each of the case studies in this thesis seems to share some influential characteristics. Wind and wave tend to be more applicable for a higher degree of misalignment during lower wind speeds, and the wave age ratio, C_p/U_{10}, tends to exceed 1.2 more often during the same wind speeds. The different case studies' wind directions are mainly westerly, avoiding wake effects and wind field disturbance from the nearby Alpha Ventus wind park, located east/south-east of FINO1. The use of power curves dependent on a given condition, such as misalignment, is used to investigate the effects on power generation. In some cases, especially for opposed wind waves conditions, the data points gathered are insufficient, as opposed wind waves rarely occur (between 0.79% to 7.7%, depending on the month and dataset). Nevertheless, we see an agreement of wind-wave alignments during all case studies, where aligned- and misaligned wind-wave occur most frequently.

6.2.1   Wind-Wave Alignment

Several studies [8, 56, 60] have investigated the occurrence and outcome of wind-wave alignments. In this study, the wind-wave alignment is connected to wind power generation at AV4, where power curves plotted for each alignment are used to identify any significant differences. The results in Case study III indicate only a slight difference in power generation based on alignment. However, based on the results in Case studies I and II and a study by Porchetta [8], a more reasonable indication is that alignments have a more significant effect the power generation. Case studies I and II indicate that the different alignments (aligned, misaligned, and opposed) affect the potential power generation for low-medium wind speeds (below rated wind speed).

In Case study I, figure 5.11, we see a clear contribution on the power curve. Data retrieved from cup anemometers throughout 2015 suggests that for wind speeds between cut-in and rated, the power curves for the different alignments deviate from each other, thereby affecting the power output. In figure 5.11 we can see that in cases where we experience opposed wind waves the power curve underperforms compared to cases where the angle between wind and waves are aligned or misaligned. In the same figure, 5.11, a comparison of the actual power curve with the power curves based on alignments has been conducted. The results show that the aligned wind-wave power curve over-performs by 1.16%, while the misaligned- and opposed wind-wave power curve under-performs by 0.86% and 3.19%, respectively, compared to the actual power curve. Comparing the aligned power curve against the misaligned power curve does however show a more significant difference of 2.05%, where the opposed show a 5.7% deviation.. In addition, figure 5.11 shows the probability density plot for wind speeds, indicating that the highest probability of wind speed occurrence is in the same area as where the curves deviate. A wind turbine produces more energy when at or above-rated wind speed and below cut-off wind speed, but as stated in the results and figure 5.12 (b), 32% of the energy generated occur below-rated power. Indicating that aligned-,

misaligned-, and opposed wind waves will have a minor contribution to generation at rated power but might significantly impact the generation below rated power. This finding extends our knowledge of wind-wave interactions, where misalignment effects on power generation have had little focus. However, the findings do agree with existing studies shown by Porchetta et al. [8] where differences in alignments affect the wake and power generation and by Hildebrandt et al. [18] where the occurrence of misalignment was investigated.

In Case study II we see the same tendencies as Case study I, where aligned conditions generate more energy than misaligned and opposed. In Table 5.3, we see the mean normalized power generated during each event, where aligned cases triumph over misaligned and opposed cases. In the dataset for August 2015, the length of the data is insufficient to compute a power curve for aligned-, misaligned and opposed wind waves. However, Table 5.3 shows that during aligned wind waves, the wind turbine has a capacity factor of 55%, while during opposed wind waves, the capacity factor is at 33%. The result in case study II thereby agrees with the result in Case study I. Stating expected higher energy generation during aligned wind waves than during misaligned- and opposed wind waves.

Lastly, in Case study III, power curves for each alignment are compared in figure 5.40. Results show that even though there is a less significant deviation between the different power curves, we might expect more power to be generated during aligned wind waves than during misaligned wind waves. The results show that the aligned wind-wave power curve over-performs by 2.49%, while the misaligned wind-wave power curve under-performs by 0.5% compared to the actual power curve. By looking at Table 5.7 we see that during the period $01.01.2015 - 31.01.2017$, aligned wind-waves are predominant with an occurrence of 53.4%, with misaligned- and opposed wind-waves occurring respectively 34.8% and 5.6%. Table 5.7, together with figure 5.35, showing the vertical wind profiles for aligned-, misaligned- and opposed wind-wave cases, indicates that the results in figure 5.40 are reasonable. The results show that higher wind speeds occur during aligned wind-wave events and that aligned wind waves occur more frequently than misaligned- and opposed wind waves.

6.2.2   Vertical Transfer of Horizontal Momentum

Transfer of momentum between ocean and atmosphere, especially from the ocean to the atmosphere, is one of the wind-wave interactions investigated. Several studies have investigated this interaction, including a study by Hanley et al. [35] investigating wave-driven wind jets in the MABL and a study by Grachev et al. [41] where results suggest that upward momentum (from ocean to atmosphere) may occur up to 10% of the time. This thesis further investigates if this upward momentum is visible at hub height and if it affects power generation.

High-frequency wind and wave data are used to verify an upward transfer of horizontal momentum. In Case studies I and III, wave age is used as an indication of

upward momentum, as this is stated to be a good first indication of vertical transfer of horizontal momentum [16, 33, 35]. While for case study II a power spectrum plot for all heights has been plotted to show how the footprints of the waves are visible in the wind field.

Figure 5.7, in case study I, shows significant wave height and wind speed at 90 m against generated power. As thought, waves and wind are highly correlated with a correlation coefficient of 0.75. In the figure, we see that the power deviates more when around a wind speed interval of 10 m/s. Further, in figure 5.8 the power curves for wave age ratio above and below 1.2 are plotted against each other. The power curves show no significant deviations, indicating that the potential upward transfer of horizontal momentum, indicated by wave age, is not affecting power generation.

Further on in case study III, the same indications as in case study I are repeated. As seen in figure 5.32, the power generation deviates most around the wind speed interval of 10 m/s, while it is consistently above and below this interval. In Figure 5.33 the wind speed distribution for wave age above and below 1.2 is plotted, indicating that events where upward transfer of momentum potentially may occur mainly occur during a wind speed interval between 0 m/s and 10 m/s. Lastly, in figure 5.34 no significant effect of wave age ratio is shown on the power curve.

In case study II a, power spectra are plotted for heights 15, 20, 40 and 80 m. Figure 5.20 show how wave frequency interacts with the measured wind spectra, where the footprint of the waves is visible and showing how waves interact with the lower part of the MABL. The dip in wave frequency shown between the dates 13.06.2015-17.06.2015 shows how the wave peak frequency follows the inertial subrange of the sonic spectra, indicating that waves affect the wind field. This particular event is visible at all heights. By calculating the momentum fluxes and identifying events with an upward transfer of horizontal momentum, one could compare those events with events of downward transfer of horizontal momentum under similar wind speed conditions to see if there are any apparent differences in the power generated. However, this was not done in this thesis but would be recommended for further research. Therefore, based on the results presented in this thesis, there are no clear indications of upward momentum affecting power generation.

6.2.3   Environmental Contour

Environmental contours are used to assess and define the extreme environmental conditions, which may be further used to evaluate the environmental loads on a structure, which in this thesis is relevant for an offshore wind turbine. The environmental contour describes the extreme joint values of environmental variables, such as significant wave height, wave peak period and wind speed.

In figure 5.42 the contour lines locate the boundaries of the distribution of wind speed and significant wave height, indicating that during a 100 year period, we are likely to observe wind speed above 25 m/s and a significant wave height of 12m. The data provided by the environmental contour is essential for the wind industry in or-

der to design structures to handle extreme structural loads and responses present at the measurement site. The contour also gives an overview of wind speed strength and significant wave height at a lower scale, which is essential to maximize the capacity factor. Suppose the environmental contour had shown a large cluster of values for low wind speeds. It could indicate that the wind energy resources at that particular site were not ideal for wind energy harvesting.

As discussed earlier, swell waves are often the cause of upward transfer of horizontal momentum and significantly contribute to how the wind and wave are aligned. In 5.43 the environmental contour indicates extreme events with extensive peak wave periods. These periods indicate swell waves, as swell waves are typically described with a long wavelength. Hence, the environmental contour indicates that swell waves will be present at the measurement site.

By comparing the environmental contours presented in section 5.3.4 the maximum extreme value of significant wave height in figure 5.42 does not equal the value in figure 5.43. Indicating that how the contour is calculated highly affects the result. Hence supports the statement by Haselsteiner et al. [78] that the contours should be viewed as approximate methods based on the principles of structural reliability and that this is mainly a tool used for assessing and defining extreme environmental conditions based on statistically informed guesses [76].

6.2.4 Stability and Other Analysis

Stability parameters, Weibull parameters and the wind shear exponent have been a small part of this thesis. The main objective of these analyses was to identify interesting events that might be worth investigating further. As the main objective of the thesis has mainly focused on wind-wave alignments and vertical transfer of horizontal momentum, this part of the analysis has gained little attention. However, results have been provided.

For stability, a study by Wharton et al. [13] has shown that the average power output might deviate up to 15% depending on the stability. As stated in section 2.5.1 we expect the best conditions for wind power generation to occur during neutral stability regimes. This agrees with the result shown in figure 5.14, where higher energy generation levels are seen during neutral stability events. However, to fully state, based on the data used in this thesis, that neutral stability provides better wind power generation conditions, more data is needed. This thesis uses only one month of sonic anemometer data from FINO1, which include only a few similar events, to fully determine if stability events are heavily influencing the power output.

Within the environmental condition section for each case study (I 5.1.1, II 5.2.1, III 5.3.1), we find the Weibull parameters plotted against wind speed, the wind shear and an arrangement of wind roses showing the distribution of wind directions, indicating wind veer affects.

The Weibull distribution is the most widely used probability density function for wind speed and is described by the k and c parameters. The shape parameter (k) describes the wind (wave) behaviour, where a small shape parameter value corresponds to a weak wind speed (or low significant wave height). Hence, a high shape parameter value indicated the presence of both high and low wind speed values (significant wave height). In figures 5.6, 5.17 and 5.28 the Weibull parameter plots shows how wind-wave alignment affects the Weibull parameter c and k. The c parameter is linearly related to wind speed and is used as an reference value [83], while the k parameter describes the shape of the distribution. In figure 5.6, 5.17 and 5.28 there are visible differences between aligned- and misaligned wind waves, where misaligned wind waves yields a larger k parameter value.

The wind shear exponent is also identified for each case study. For example, in a study by Honrubia et al. [19] they found that when medium or high shear exponents were found in front of the swept rotor area of a wind turbine, the power generated was lower than expected for the wind speed measured at the hub height. In section 5.3.3 the mean wind shear exponents for heights 10 m to 250 m are shown for each wind-wave alignment. The figure clearly shows that aligned wind waves at hub height give a higher wind shear exponent, thereby indicating that we experience higher wind speeds under aligned wind waves than for misaligned- and opposed wind waves.

6.3   Limitations

In this thesis, the main focus has been on wind and wave interaction and how they affect the power generation of an offshore wind turbine. As the ocean waves move slowly compared to the wind, the wind and wave data is set/investigated at an hourly rate. Data given in 10-min bins have been upsampled to hourly data.

This thesis uses three different datasets: reanalysis dataset, cup anemometer data, and sonic anemometer data. The sonic anemometer data is retrieved from August 2015, where the data availability was at only 54% before filtering. Low data availability causes the available data sample to be minor, meaning that broader generalization of the results is impossible.

Wind data is retrieved from the FINO1 platform, wave data from a nearby buoy and power data from AV4. As all data is not retrieved at the exact location, this may limit the results and the usability of the results. As mentioned in Chapter 4, the data is assumed to be perfectly usable due to the slowness of the waves and since all locations are located in the vicinity of each other. However, this limitation must be addressed, including the fact that wind park correction is not used.

NORA3 is based on reanalysis data and may not correctly represent the actual conditions found at the site. Even though NORA3 have been proved to be a good fit for actual wind data, there still may be questions about how well NORA3 compares and handles wind-wave interactions and whether it is usable for such analysis. Further analysis could uncover how well it fits with actual wind-wave interactions.

The most extended dataset used contains measurements spread over two years, which may not be sufficient to generalize this thesis's results. Using more extended datasets could provide more significant power curve deviations, which further would better indicate the effect of wind-wave interactions.

The presented results are affected by how the angles between waves and winds are categorized into bins. As shown in Table 2.7 the alignment bins vary in size, where the size of the misalignment bin is 105 °. Therefore, changing the size of the alignments bins will affect the degree of occurrences located in each bin. In this thesis, the bins have been chosen by the author and the supervisor to capture enough measurements to compile a study on the alignment differences, where the opposed alignment bin is larger than the aligned for this reason.

The available data from the different Case studies have different pros and cons, where the analysis provided depends on the variables available. E.g. momentum and stress can only be calculated with sonic anemometers, as the contributions of u, v and z are necessary. These variables are not available for the cup anemometer or the NORA3 dataset. Therefore, certain analysis is dropped for these measurements.

Chapter 7

Conclusions and Future Work

This dissertation has analyzed wave and wind measurements at FINO1 and compared the power generation data from the nearby Alpha Ventus 4 wind park. Cup anemometer data, sonic anemometer data, SCADA data, and NORA3 reanalyzed data have been utilized to provide a process study to uncover how different wind-wave interactions interfere with offshore wind turbine performance.

Different wind-wave interactions occurring at FINO1 and how they affect the power generation at AV4 is included in this thesis. The main focus has been on wind-wave alignments, such as aligned, misaligned and opposed (see section 2.4.4). However, indications of upward transfer of horizontal momentum have also been in focus. In addition, stability parameters, Weibull parameters and the wind shear coefficient have been included. The result from these different analyses show wind-wave interactions affecting the wind field. Power generation during neutral stabilities seems to be higher than in stable and unstable conditions. However, these results do not have any significant analytical weight and should therefore only be interpreted as interesting findings that should be further analyzed.

The complexity of the wind-wave systems and the many parameters that seem to have an impact on the power generation have been investigated in this thesis, where the major findings were:

1. Wind-wave alignments have a visible effect on the power output, where alignments cause the power curve to deviate up to 3.19% compared to the actual power curve.

2. The power curve for aligned wind waves performs best in all scenarios, showing a deviation up to 5.7% compared to the opposed wind-wave power curve.

3. Wind-wave alignments affect the power curve during lower to medium wind speeds (between cut-in and rated wind speed).

4. Power generation at wind speeds around 10 m/s is most affected by wind-wave alignments.

5. Wind-wave misalignment frequently occurs, especially during low-to-medium wind speeds (below rated wind speed).

6. Stronger wind forces are expected during aligned wind waves compared to misaligned- and opposed wind waves.

7. The angle between wind and waves is typically higher during lower wind speeds and tends to become more aligned during higher wind speeds.

8. Misaligned wind waves occur in the region of $35 - 50\%$ of the time.

9. No significant contributions of upward transfer of horizontal momentum on wind power generation, but this interaction should be further investigated.

10. There are visible differences in the dataset from NORA3 compared to the dataset from FINO1 (OBLEX-F1 & routinely measurements), indicating wind-wave interactions are not properly depicted in NORA3.

    This thesis has mainly focused on wind-wave alignments, thereby neglecting or downscaling the focus on other important parameters within wind-wave interaction. The upward transfer of horizontal momentum should be further investigated, as well as conducting a more extended analysis of wind-wave alignment effects on power generation over several years. Furthermore, further research should be conducted on how wind and wave affect the structural loads on an offshore floating structure, especially focusing on what effect an upward transfer of horizontal momentum and wave-induced low-level jet have. Lastly, a more in-depth investigation of wind-wave alignment during a more extended period would further describe the magnitude of wind-wave misalignment's effect on power generation.

List of Figures

List of Tables

List of Equations

Bibliography

[1] IEA. Wind power. (visited on 07/03/2022). [Online]. Available: https://www.iea.org/reports/wind-power

[2] WindEurope asbl/vzw. Wind energy in europe 2020 statistics and the outlook for 2021-2025. (visited on 14/02/2022). [Online]. Available: https://windeurope.org/intelligence-platform/product/wind-energy-in-europe-2020-statistics-and-the-outlook-for-2021-2025/

[3] WindEurope. Wind energy in europe 2021 statistics and the outlook for 2022-2026. (visited on 16/05/2022). [Online]. Available: https://windeurope.org/intelligence-platform/product/wind-energy-in-europe-2021-statistics-and-the-outlook-for-2022-2026/

[4] WindEurope asbl/vzw. History of europe's wind industry. (visited on 07/12/2021). [Online]. Available: https://windeurope.org/about-wind/history/

[5] C. Walsh, "Offshore wind in Europe: Key trends and statistics 2019," Wind Europe, Tech. Rep. 2, 2019. [Online]. Available: https://windeurope.org/wp-content/uploads/files/about-wind/statistics/WindEurope-Annual-Offshore-Statistics-2019.pdf

[6] Directorate for ICT and joint service in higher education and research. How to use oria. (visited on 14/02/2022). [Online]. Available: https://www.unit.no/en/node/620

[7] S. Pal Arya, "Marine Atmospheric Boundary Layer," in *International Geophysics*, S. P. Arya, Ed. Academic Press, 1988, vol. 42, no. C, ch. 13, pp. 197–222.

[8] P. Sara, M.-E. Domingo, M. Wim, v. B. Jeroen, and v. L. Nicole, "Impact of ocean waves on offshore wind farm power production," *Renewable Energy*, vol. 180, 2021.

[9] S. M. Kalvig, "On Wave-Wind Interactions and Implications for Offshore Wind Turbines," PhD, Univeristy of Stavanger, 2015.

[10] M. B. Paskyabi, S. Zieger, A. D. Jenkins, A. V. Babanin, and D. Chalikov, "Sea surface gravity wave-wind interaction in the marine atmospheric boundary layer," *Energy Procedia*, vol. 53, no. C, pp. 184–192, 2014. [Online]. Available: http://dx.doi.org/10.1016/j.egypro.2014.07.227

[11] M. Flügge, M. Bakhoday-Paskyabi, J. Reuder, and O. El Guernaoui, "Wind stress in the coastal zone: Observations from a buoy in southwestern Norway," *Atmosphere*, vol. 10, no. 9, pp. 1–32, 2019.

[12] A. Smedman, U. Högström, H. Bergström, A. Rutgersson, K. K. Kahma, and H. Pettersson, "A case study of air-sea interaction during swell conditions," *Journal of Geophysical Research: Oceans*, vol. 104, no. C11, pp. 25 833–25 851, 1999.

[13] S. Wharton and J. K. Lundquist, "Atmospheric stability affects wind turbine power collection," *Environmental Research Letters*, vol. 7, no. 1, p. 9, 2012.

[14] S. Emeis, "Current issues in wind energy meteorology," *Meteorological Applications*, vol. 21, no. 4, pp. 803–819, 2014.

[15] R. B. Stull, *An Introduction to Boundary Layer Meteorology*, ser. Atmospheric Sciences Library. Springer, Dordrecht, 1988, vol. 13.

[16] S. Porchetta, O. Temel, D. Muñoz-Esparza, J. Reuder, J. Monbaliu, J. Van Beeck, and N. Van Lipzig, "A new roughness length parameterization accounting for wind-wave (mis)alignment," *Atmospheric Chemistry and Physics*, vol. 19, no. 10, pp. 6681–6700, 2019.

[17] G. P. Van Vledder, "On wind-wave misalignment, directional spreading and wave loads," in *Proceedings of the International Conference on Offshore Mechanics and Arctic Engineering - OMAE*, G. P. Van Vledder, Ed., vol. 5, no. June 2013, Nantes, France, 2013.

[18] A. Hildebrandt, B. Schmidt, and S. Marx, "Wind-wave misalignment and a combination method for direction-dependent extreme incidents," *Ocean Engineering*, vol. 180, no. March 2018, pp. 10–22, 2019.

[19] A. Honrubia, A. Vigueras-Rodríguez, E. Ǵomez Ĺazaro, and D. Rodŕiguez-Śanchez, "The influence of wind shear in wind turbine power estimation," *European Wind Energy Conference and Exhibition 2010, EWEC 2010*, vol. 6, pp. 4130–4139, 2010.

[20] S. Emeis, *Wind Energy Meteorology*. Springer International Publishing AG, part of Springer Nature 2018, 2013. [Online]. Available: http://www.benthamdirect.org/pages/content.php?9781608052851

[21] NASA. Global wind patterns. (visited on 27/03/2022). [Online]. Available: https://commons.wikimedia.org/wiki/File:NASA_depiction_of_earth_global_atmospheric_circulation.jpg

[22] T. Hara and S. E. Belcher, "Wind profile and drag coefficient over mature ocean surface wave spectra," *Journal of Physical Oceanography*, vol. 34, no. 11, pp. 2345–2358, 2004.

[23] J. Du, R. Bolaños, and X. Guo Larsén, "The use of a wave boundary layer model in SWAN," *Journal of Geophysical Research: Oceans*, vol. 122, no. 1, pp. 42–62, 2017.

[24] M. C. Holtslag, W. A. Bierbooms, and G. J. Van Bussel, "Estimating atmospheric stability from observations and correcting wind shear models accordingly," *Journal of Physics: Conference Series*, vol. 555, no. 1, 2014.

[25] S. Emeis and M. Turk, "Comparison of Logarithmic Wind Profiles and Power Law Wind Profiles and their Applicability for Offshore Wind Profiles," *Wind Energy*, no. December, pp. 61–64, 2007.

[26] B. Robertson, G. Dunkle, J. Gadasi, G. Garcia-Medina, and Z. Yang, "Holistic marine energy resource assessments: A wave and offshore wind perspective of metocean conditions," *Renewable Energy*, vol. 170, pp. 286–301, 2021. [Online]. Available: https://doi.org/10.1016/j.renene.2021.01.136

[27] H. Charnock, "Wind stress on water: An hypothesis," *Quarterly Journal of the Royal Meteorological Society*, vol. 81, no. 350, pp. 639–639, 1955.

[28] A. Peña and S. E. Gryning, "Charnock's roughness length model and non-dimensional wind profiles over the sea," *Boundary-Layer Meteorology*, vol. 128, no. 2, pp. 191–203, 2008.

[29] American Meteorological Society. Buoyancy. (visited on 15/02/2022). [Online]. Available: https://glossary.ametsoc.org/wiki/Buoyancy

[30] J. J. Voermans, H. Rapizo, H. Ma, F. Qiao, and A. V. Babanin, "Air–sea momentum fluxes during tropical cyclone olwyn," *Journal of Physical Oceanography*, vol. 49, no. 6, pp. 1369–1379, 2019.

[31] S. E. Belcher and J. C. Hunt, "Turbulent flow over hills and waves," *Annual Review of Fluid Mechanics*, vol. 30, pp. 507–538, 1998.

[32] L. S. Thauvin, "Response of Monopile Wind Turbines to Higher Order Wave Loads," phD, NTNU, 2019.

[33] K. E. Hanley, S. E. Belcher, and P. P. Sullivan, "A Global climatology of wind-wave interaction," *Journal of Physical Oceanography*, vol. 40, no. 6, pp. 1263–1282, 2010.

[34] A. Semedo, Ø. Saetra, A. Rutgersson, K. K. Kahma, and H. Pettersson, "Wave-induced wind in the marine boundary layer," *Journal of the Atmospheric Sciences*, vol. 66, no. 8, pp. 2256–2271, 2009.

[35] K. E. Hanley and S. E. Belcher, "Wave-driven wind jets in the marine atmospheric boundary layer," *Journal of the Atmospheric Sciences*, vol. 65, no. 8, pp. 2646–2660, 2008.

[36] J. W. Miles, "On the generation of surface waves by shear flows," *Journal of Fluid Mechanics*, vol. 3, no. 2, pp. 185–204, 1957.

[37] J. E. Cohen and S. E. Belcher, "Turbulent shear flow over fast-moving waves," *Journal of Fluid Mechanics*, vol. 251, pp. 109–148, 1993.

[38] K. Hanley, "A global perspective of wind-wave interaction and the distribution of wave momentum," PhD, The Univeristy of Reading, 2008. [Online]. Available: http://ethos.bl.uk/OrderDetails.do?uin=uk.bl.ethos.501332

[39] S. D. Smith, "Wind stress and heat flux over the ocean in the Gale force winds." *Journal of Physical Oceanography*, vol. 10, no. 5, pp. 709–726, 1980.

[40] A. M. Sempreviva, N. G. Mortensen, S. E. Larsen, and I. Troen, "Response of neutral boundary layers to changes of roughnessss," *Boundary-Layer Meteorology*, vol. 50, no. 1-4, pp. 205–225, 1990.

[41] A. A. Grachev and C. W. Fairall, "Upward momentum transfer in the marine boundary layer," *Journal of Physical Oceanography*, vol. 31, no. 7, pp. 1698–1711, 2001.

[42] K. Hasselmann, T. P. Barnett, E. Bouws, H. Carlson, D. E. Cartwright, K. Eake, J. A. Euring, A. Gicnapp, D. E. Hasselmann, P. Kruseman, A. Meerburg, P. Mullen, D. J. Olbers, K. Richren, W. Sell, and H. Walden, "Measurements of wind-wave growth and swell decay during the joint North Sea wave project (JONSWAP)." *Deut.Hydrogr. Z.*, vol. 8, pp. 1–95, 1973.

[43] K. Ye and J. Ji, "Current, wave, wind and interaction induced dynamic response of a 5MW spar-type offshore direct-drive wind turbine," *Engineering Structures*, vol. 178, pp. 395–409, 2019.

[44] C. Koukoura, C. Brown, A. Natarajan, and A. Vesth, "Cross-wind fatigue analysis of a full scale offshore wind turbine in the case of wind-wave misalignment," *Engineering Structures*, vol. 120, pp. 147–157, 2016. [Online]. Available: http://dx.doi.org/10.1016/j.engstruct.2016.04.027

[45] X. Hao and L. Shen, "Wind-wave coupling study using les of wind and phase-resolved simulation of nonlinear waves," *Journal of Fluid Mechanics*, vol. 874, pp. 391–425, 2019.

[46] I. J. Moon, T. Hara, I. Ginis, S. E. Belcher, and H. L. Tolman, "Effect of surface waves on air-sea momentum exchange: Part I: Effect of mature and growing seas," *Journal of the Atmospheric Sciences*, vol. 61, no. 19, pp. 2321–2333, 2004.

[47] J. Battjes, E. Bouws, L. Burroughs, D. Carter, L. Draper, L. Eide, J. Ewing, W. Gemmill, L. Holthuijsen, M. Khandekar, A. Laing, A. Magnusson, M. Reistad, and V. Swail., *Guide to Wave Analysis and Forecasting*, 3rd ed., J. Battjes, E. Bouws, L. Burroughs, D. Carter, L. Draper, L. Eide, J. Ewing, W. Gemmill, L. Holthuijsen, M. Khandekar, A. Laing, A. Magnusson, M. Reistad, and V. Swail., Eds.   World Meteorological Organization, 2018, no. 702.

[48] T. Hara and P. P. Sullivan, "Wave boundary layer turbulence over surface waves in a strongly forced condition," *Journal of Physical Oceanography*, vol. 45, no. 3, pp. 868–883, 2015.

[49] A. Semedo, "Atmosphere-Ocean Interactions in Swell Dominated Wave Fields," PhD, Uppsala Univeristy, 2010.

[50] P. P. Sullivan, J. B. Edson, T. Hristov, and J. C. McWilliams, "Large-eddy simulations and observations of atmospheric marine boundary layers above nonequilibrium surface waves," *Journal of the Atmospheric Sciences*, vol. 65, no. 4, pp. 1225–1245, 2008.

[51] P. C. Kalverla, J. B. Duncan, G. J. Steeneveld, and A. A. Holtslag, "Low-level jets over the north sea based on ERA5 and observations: Together they do better," *Wind Energy Science*, vol. 4, no. 2, pp. 193–209, 2019.

[52] G. P. Van Vledder and L. H. Holthuijsen, "The Directional Response of Ocean Waves to Turning Winds," *Journal of Physical Oceanography*, vol. 23, no. 9, pp. 177–192, 1993. [Online]. Available: https://doi.org/10.1175/1520-0485(1993)023{%}3C0177:TDROOW{%}3E2.0.CO;2

[53] K. Yousefi, F. Veron, and M. P. Buckley, "Momentum flux measurements in the airflow over wind-generated surface waves," *Journal of Fluid Mechanics*, vol. 895, 2020.

[54] T. Cao and L. Shen, "A numerical and theoretical study of wind over fast-propagating water waves," *Journal of Fluid Mechanics*, vol. 919, pp. 1–35, 2021.

[55] D. Wang, T. Kukulka, B. G. Reichl, T. Hara, and I. Ginis, "Wind-wave misalignment effects on Langmuir turbulence in tropical cyclones conditions," *Journal of Physical Oceanography*, vol. 49, no. 10, pp. 3109–3126, 2019.

[56] A. S. Verma, Z. Jiang, Z. Ren, Z. Gao, and N. P. Vedvik, "Effects of Wind-Wave Misalignment on a Wind Turbine Blade Mating Process: Impact Velocities, Blade Root Damages and Structural SafetyAssessment," *Journal of Marine Science and Application*, vol. 19, no. 2, pp. 218–233, 2020.

[57] Z. S. Haghayeghi, H. Imani, and M. Karimirad, "Directional dependence of extreme metocean conditions for analysis and design of marine structures," *Applied Ocean Research*, vol. 100, no. April, p. 102181, 2020. [Online]. Available: https://doi.org/10.1016/j.apor.2020.102181

[58] Q. Li, E. Bou-Zeid, N. Vercauteren, and M. Parlange, "Signatures of Air–Wave Interactions Over a Large Lake," *Boundary-Layer Meteorology*, vol. 167, no. 3, pp. 445–468, 2018.

[59] E. G. Patton, "Final Report for Project: Impacts of stratification and non-equilibrium winds and waves on hub-height winds," University Corporation for Atmospheric Research National Center for Atmospheric Research, Tech. Rep., 2005. [Online]. Available: https://www.osti.gov/biblio/1322012

[60] S. Kalvig, L. Eliassen, and E. Manger, "On Offshore wind turbine fatigue caused by wave influenced wind," in *E3S Web of Conferences*, vol. 5. Les Ulis: EDP Sciences, 2015, p. p.2001.

[61] N. Sucevic and Z. Djurisic, "Influence of atmospheric stability variation on uncertainties of wind farm production estimation," in *European Wind Energy Conference and Exhibition 2012, EWEC 2012*, vol. 3, no. April, 2012, pp. 1891–1899.

[62] E. W. Tedford, S. MacIntyre, S. D. Miller, and M. J. Czikowsky, "Similarity scaling of turbulence in a temperate lake during fall cooling," *Journal of Geophysical Research C: Oceans*, vol. 119, no. 8, pp. 4689–4713, 2014. [Online]. Available: doi:10.1002/2014JC010135

[63] O. Krogsaeter and J. Reuder, "Validation of boundary layer parameterization schemes in the Weather Research and Forecasting (WRF) model under the aspect of offshore wind energy applications—part II: boundary layer height and atmospheric stability," *Wind Energy*, vol. 18, pp. 1291–1302, 2015.

[64] ABB. Pitch system. (visited on 08/03/2022). [Online]. Available: https://new.abb.com/low-voltage/industries/wind-power/utility-scale-turbine/pitch-system

[65] Federal Ministry of Economics and Energy. Fino1 - research platform in the north and baltic seas no. 1. (visited on 07/12/2021). [Online]. Available: https://www.FINO1.de/en/

[66] ——. Fino1 design. (visited on 07/12/2021). [Online]. Available: https://www.fino1.de/en/about/design.html

[67] M. E. Dr. Bernhard Lange. About Rave. (visited on 07/12/2021). [Online]. Available: https://rave-offshore.de/en/about-rave.html

[68] ——. Measurements in rave and data access. (visited on 07/12/2021). [Online]. Available: https://rave-offshore.de/en/data.html

[69] H. Haakenstad, Ø. Breivik, B. R. Furevik, M. Reistad, P. Bohlinger, and O. J. Aarnes, "Nora3: A nonhydrostatic high-resolution hindcast of the north sea, the Norwegian sea, and the barents sea," *Journal of Applied Meteorology and Climatology*, vol. 60, no. 10, pp. 1443–1464, 2021.

[70] I. M. Solbrekke, A. Sorteberg, and H. Haakenstad, "Norwegian hindcast archive (NORA3) – A validation of offshore wind resources in the North Sea and Norwegian Sea," *Wind Energy Science Discussions*, no. June 2020, pp. 1–31, 2021.

[71] "Python language reference, version 3.8." Python Software Foundation, (visited on 27/03/2022). [Online]. Available: http://www.python.org

[72] F. P. Thomas Kluyver, Benjamin Ragan-Kelley, B. Granger, M. Bussonnier, J. Frederic, K. Kelley, J. Hamrick, J. Grout, S. Corlay, P. Ivanov, D. Avila, S. Abdalla, and C. Willing, "Jupyter notebooks – a publishing format for reproducible computational workflows," in *Positioning and Power in Academic Publishing: Players, Agents and Agendas*, F. Loizides and B. Schmidt, Eds. IOS Press, 2016, pp. 87 – 90.

[73] A. J. Kettle, "Unexpected vertical wind speed profiles in the boundary layer over the southern North Sea," *Journal of Wind Engineering and Industrial Aerodynamics*, vol. 134, pp. 149–162, 2014. [Online]. Available: http://dx.doi.org/10.1016/j.jweia.2014.07.012

[74] P. Virtanen, R. Gommers, T. E. Oliphant, M. Haberland, T. Reddy, D. Cournapeau, E. Burovski, P. Peterson, W. Weckesser, J. Bright, S. J. van der Walt, M. Brett, J. Wilson, K. J. Millman, N. Mayorov, A. R. J. Nelson, E. Jones, R. Kern, E. Larson, C. J. Carey, İ. Polat, Y. Feng, E. W. Moore, J. VanderPlas, D. Laxalde, J. Perktold, R. Cimrman, I. Henriksen, E. A. Quintero, C. R. Harris, A. M. Archibald, A. H. Ribeiro, F. Pedregosa, P. van Mulbregt, and SciPy 1.0 Contributors, "SciPy 1.0: Fundamental Algorithms for Scientific Computing in Python," *Nature Methods*, vol. 17, pp. 261–272, 2020.

[75] M. Optis, A. Monahan, and F. C. Bosveld, "Moving Beyond Monin–Obukhov Similarity Theory in Modelling Wind-Speed Profiles in the Lower Atmospheric Boundary Layer under Stable Stratification," *Boundary-Layer Meteorology*, vol. 153, no. 3, pp. 497–514, 2014.

[76] A. F. Haselsteiner, A. Sander, J. H. Ohlendorf, and K. D. Thoben, "GLOBAL HIERARCHICAL MODELS FOR WIND AND WAVE CONTOURS: PHYSICAL INTERPRETATIONS OF THE DEPENDENCE FUNCTIONS," in *Proceedings of the 39th International Conference on Ocean, Offshore and Arctic Engineering*, Fort Lauderdale, Florida, USA, 2020, p. 10.

[77] C. Qiao and A. T. Myers, "A new IFORM-Rosenblatt framework for calculation of environmental contours," *Ocean Engineering*, vol. 238, no. January, p. 109622, 2021. [Online]. Available: https://doi.org/10.1016/j.oceaneng.2021.109622

[78] A. F. Haselsteiner, R. G. Coe, L. Manuel, W. Chai, B. Leira, G. Clarindo, C. Guedes Soares, Á. Hannesdóttir, N. Dimitrov, A. Sander, J. H. Ohlendorf, K. D. Thoben, G. de Hauteclocque, E. Mackay, P. Jonathan, C. Qiao, A. Myers, A. Rode, A. Hildebrandt, B. Schmidt, E. Vanem, and A. B. Huseby, "A benchmarking exercise for environmental contours," *Ocean Engineering*, vol. 236, pp. 1–37, 2021.

[79] S. R. Winterstein, T. C. Ude, C. A. Cornell, P. Bjerager, and S. Haver, "ENVIRONMENTAL PARAMETERS FOR EXTREME RESPONSE: INVERSE FORM WITH OMISSION FACTORS," in *ICOSSAR-93*, vol. 2, Innsbruck, Austria, 1993, pp. 142–148.

[80] A. F. Haselsteiner, J. Lehmkuhl, T. Pape, K. L. Windmeier, and K. D. Thoben, "ViroCon: A software to compute multivariate extremes using the environmental contour method," *SoftwareX*, vol. 9, pp. 95–101, 2019.

[81] G. J. Bowden, P. R. Barker, V. O. Shestopal, and J. W. Twidell, "Weibull Distribution Function and Wind Power Statistics." *Wind Engineering*, vol. 7, no. 2, pp. 85–98, 1983.

[82] M. J. Stevens and P. T. Smulders, "Estimation of the Parameters of the Weibull Wind Speed Distribution for Wind Energy Utilization Purposes." *Wind Engineering*, vol. 3, no. 2, pp. 132–145, 1979.

[83] A. Genc, M. Erisoglu, A. Pekgor, G. Oturanc, A. Hepbasli, and K. Ulgen, "Estimation of wind power potential using weibull distribution," *Energy Sources*, vol. 27, no. 9, pp. 809–822, 2005.

[84] D. Babayani, M. Khaleghi, and M. Hashemi-Tilehnoee, "Assessment of wind energy potential in Golestan province of Iran," *International Journal of Renewable Energy Development*, vol. 5, no. 1, pp. 25–31, 2016.

[85] J. Keller, "Simulation of Wind With a Variable ' K ' Parameter," *Wind Engineering*, vol. 16, no. 6, pp. 307–312, 1992. [Online]. Available: https://www.jstor.org/stable/43749485

[86] F. Kinder, A. Westerhellweg, T. Neumann, and D. Wilhelmshaven, "Park Correction for FINO1- Wind Speed Measurements at alpha ventus," *DEWI Magazin*, no. 42, pp. 61–64, 2013.